Analysis of the Behaviour of Long-Runout Rock Avalanches Using Simple Energy Models

by

Cassandra Vanderwerff

A thesis
presented to the University of Waterloo
in fulfillment of the
thesis requirement for the degree of
Master of Science
in
Earth Sciences

Waterloo, Ontario, Canada, 2021

Author's Declaration

I hereby declare that I am the sole author of this thesis. This is a true copy of the thesis, including any required final revisions, as accepted by my examiners.

I understand that my thesis may be made electronically available to the public.

Abstract

Rock avalanches are a natural hazard of fragmented rock with extreme geomorphological impact and cause significant amounts of damage to the human population. This thesis develops and evaluates simple physics-based energy models to explain the high mobility of rock avalanches and to expand upon preceding research. A review of relevant literature is presented, and five major research topics are addressed.

First, it is shown that the numerous models that have been adopted for avalanche fragmentation are not in consistent agreement about the energy spent during this process. Second, there appears to be a lack of consensus regarding whether entrainment of path substrate materials induces a gain or loss in energy is gained or lost from this behaviour. Third, it has been typically assumed that the apparent coefficient of friction for a rock avalanche remains constant – which is likely false. Fourth, it is shown that the environment, geology, degree of lateral confinement and failure mechanism are key variables that control the horizontal travel distance travelled yet are rarely accounted for in various models. Lastly, this thesis shows, through a preliminary analysis of a Galileo Scaling relationship between volume and the horizontal travel distance, that rock avalanche databases are scant in data, limiting analyses.

Simple physics energy models were considered to examine rock avalanche behaviour as it pertains to the horizontal distance travelled. The simple physics energy models considered are sliding, entrainment, deposition, fragmentation, and impact. The simple sliding energy model examined the sliding motion exhibited by rock avalanches and the entrainment energy model considered the mass gained during an event. The deposition energy model examined mass loss and the fragmentation energy model observed the energy required to break a rock mass. Lastly, the impact energy model examined the energy lost when the failure mass impacts a lower slope. From

the simple physics energy models, it was concluded that the horizontal distance travelled by a rock avalanche is not mass-dependent. Rather, the horizontal distance travelled appears to be dependent on the percentage of mass gained or lost with respect to the initial mass. Further, it was determined from the entrainment and fragmentation energy models that Heim's Ratio is not a sufficient assumption for the apparent coefficient of friction value.

A preliminary statistical analysis provided further insight into Galileo Scaling and its relation to rock avalanches. It was determined that there was a square-cube scaling relationship between the volume and horizontal distance travelled by a rock avalanche. This relationship was further examined through smaller datasets. By constraining the data into datasets of analogous events, the scatter reduced. With further research, this could be developed into an empirical model to potentially predict rock avalanche travel distances.

Acknowledgments

I would like to first thank Dr. Stephen Evans whose knowledge and expertise in rock avalanches and landslides was invaluable for formulating this thesis. Your feedback has helped me sharpen my data analysis and research skills.

Secondly, I would like to thank Dr. Yuri Leonenko for his knowledge in physics, his assistance was critical to the creation of the simple energy models.

Next, I would like to thank Dr. Keith Delaney for his valuable guidance throughout the completion of this thesis. I would like to thank you for your support for the last few years.

I would also like to thank my friends Nahyan Rana and Graeme Milligan for their frequent help and support. They also provided much needed mental distractions from research when needed.

Lastly, I would like to thank my family for their love and support during this process.

Table of Contents

List of Figures

List of Tables

Chapter 1 : Introduction

1.1 Introduction

Rock avalanches are catastrophic natural hazards that often occur with no witnesses or recordings (Wang et al. 2018a; Francioni et al. 2019; Lato et al. 2019). These events typically occur in mountainous regions and are capable of burying areas under a thick debris field and causing vast amounts of destruction (Dufresne et al. 2016a; Reznichenko et al. 2017; Francioni et al. 2019; Strom et al. 2019). Among the first documented rock avalanches was the 1881 Elm event in Switzerland (Heim, 1882), while other examples include the 1903 Frank Slide (Alberta), 2009 Jiweishan rock avalanche (China), and 2017 Xinmo rock avalanche (China) (Benko and Stead, 1998; Fan et al. 2017; Huang et al. 2019; Zhang et al. 2019). Such events are particularly devastating due to exceptional flow volumes, very long and expansive runouts in diverse terrain, high mechanical energy and extremely rapid flow velocities (Heim, 1932; Crosta et al. 2004; Hermanns and Lonya, 2012; Hungr et al. 2014). The Mount Meager rock avalanche had a volume of 48.5 x 10^6 m^3 (Guthrie et al. 2012, 2012b; Roberti et al. 2017). Rock avalanches are also capable of blocking rivers thus forming landslide-dammed lakes, while also on occasion causing tsunamis (Dufresne et al. 2018; Jelinek and Zacek, 2018; Huang et al. 2019; Je et al. 2020). Figure 1.1 shows the destructive nature of the 1903 Frank Slide that buried a mining town and took more than 70 lives (Benko and Stead, 1998).

Figure 1.1 An aerial satellite image of the 1903 Frank Slide, Alberta, and the visible deposit which travelled northeast over the town of Frank. (Google Earth, 2021d).

From Figure 1.1, the scar of the 1903 rock avalanche is still visible in 2018, and it shows the extent of the area coved by the debris. It is important to determine what causes this behaviour in order to reduce the risk of life loss and assess the overall geomorphic impact.

1.2 Thesis Objectives

The processes which contribute to the high mobility of rock avalanches have been debated extensively in past literature (Legros, 2002), which warrants further research. This thesis is thereby limited to four objectives that are aimed to address knowledge gaps:

1. Complete a literature review of rock avalanche behaviour;

2. Apply simple physics to explore rock avalanche dynamics, particularly concerning the horizontal distance travelled and apparent reduction in the coefficient of friction;
3. Explore Galileo Scaling as it relates to rock avalanche geometry and complete a preliminary analysis to gain insight into rock avalanche field behaviour; and
4. Examine the implication of the work for a new understanding of rock avalanche behaviour including recommendations for future research.

1.3 Thesis Summary

The thesis has been divided into five chapters, of which this is the introduction.

Chapter 2 focuses on identifying current knowledge gaps through the completion of a review of rock avalanche and landslide literature. The literature review will focus on current and previous rock avalanche models and field investigations into rock avalanche behaviour.

Chapter 3 examines the application of simple physics to various rock avalanche mechanisms. These simple models are based on energy equations and energy lost to these processes. A parametric analysis will be completed to determine which parameters affect the horizontal distance travelled by rock avalanches.

Chapter 4 will focus on Galileo Scaling and its potential relationship to rock avalanche geometry. A preliminary statistical analysis will be completed to characterise this relationship and to better understand this empirical model.

Chapter 5 will summarise the findings of the thesis. This chapter will also suggest areas that require further research.

1.4 Identification of Current Knowledge Gaps in Rock Avalanche Literature

Rock avalanche literature spans over a century and many notable contributions have been made. However, there are still some areas of research that require further work, including:

1. The rate of energy consumption by rock avalanche fragmentation and the corresponding impact on the horizontal travel distance;
2. The role of path substrate material entrainment in inducing energy loss or gain;
3. The role of environment (i.e. glacial, volcanic, mountainous, soil dense, non-mountainous), geology, initial failure mechanism, and degree of lateral confinement in influencing the horizontal travel distance;
4. The lack of a consistency when calculating the coefficient of friction of a rock avalanche, particularly considering that coefficient of friction of a rock avalanche likely changes through the duration of the event, contradicting the assumption of a constant value;
5. The lack of data in rock avalanche databases is inhibiting the analysis of rock avalanches. An example can be shown through the Galileo Scaling relationship observed between the volume and the horizontal distance travelled.

1.5 Rock Avalanche Database

Several datasets have been collected and utilised to create a new rock avalanche database of 337 events that will be used to obtain baseline values for the parametric analysis completed in Chapter 3 as well as the statistical analysis to evaluate Galileo Scaling. Data sources include: Scheidegger (1973), Cruden (1976), Eisbacher (1977), (1979), Clague and Souther (1982), Cruden (1982), Whitehouse and Griffiths (1983), Cruden and Eaton (1987), Jackson and Isobe (1990),

Ryder et al. (1990), Evans and Clague (1988), Nicoletti and Sorriso-Valvo (1991), Siebe et al. (1992), Hermanns and Strecker (1999), Evans et al. (2001), Levson et al. (2003), Hungr and Evans (2004), Huscroft et al. (2004), Orwin et al. (2004), Geertsema et al. (2006), Locat et al. (2006), Masson et al. (2008), Sosio et al. (2008), Brideau et al. (2009), Lee et al. (2009), Tang et al. (2009a), Brideau et al. (2012), Guthrie et al. (2012a,b), Hermanns et al. (2012), Sakals et al. (2012), Sosio et al. (2012), Zhou et al. (2012), Barth (2014), Blais-Stevens et al. (2015), Dufresene et al. (2015), Crosta et al. (2017), Hooft et al. (2017), Schleier et al. (2017), Wang et al. (2017), Zhan et al. (2017) and Mitchell et al. (2019).

Chapter 2 : Literature Review of Rock Avalanche Models and Statistical Analyses

2.1 Introduction

The term landslide is used to classify a variety of mass wasting processes which range from soil to rock failures (ISRM, 1981). Landslides often exhibit exceptionally long horizontal travel distances that imply a reduction in the coefficient of friction for the material in which it occurs (Heim, 1932; Hsu, 1975; Hewitt et al. 2008; Evans et al. 2009). The coefficient of friction of a rock avalanche (implied in the geometry of its travel path) is typically much lower than the coefficient of friction of a similar dry material (Heim, 1882; Favreau et al. 2010; Iverson, 2015; Haug et al. 2016).

Rock avalanches initiate as intact rock masses on a slope face and typically occur in mountainous regions (Lucas et al. 2014; Francioni et al. 2019). Rock, an earth material is defined as having a minimum of 1 MPa intact unconfined compressive strength (ISRM, 1981; Brideau and Roberts, 2015). For a rock mass failure to be classified as a rock avalanche it must meet two criteria as outlined by Legros (2002); the volume of the rock mass must exceed 1 Mm^3 and the debris produced by the fragmentation of the rock mass must display an excessively long horizontal travel distance as shown in Figure 2.1 (Hsu, 1975; Legros, 2002; Ren et al. 2018). There are some exceptions to the volume criteria for rock mass failures that are slightly smaller than 1 Mm^3 and still display an unprecedently long travel distances (Hsu, 1975; Legros, 2002; Ren et al. 2018). Further, rock avalanches undergo a significant degree of fragmentation when they fall away from the source area and onto the slope below as displayed in Figure 2.2 (Hungr et al. 2001; Brideau and Roberts, 2015; Delannay et al. 2017; Preh, 2020).

Rock avalanches display excessive travel distances due to the apparent reduction in the coefficient of friction of the material. The coefficient of friction of a rock ranges from 20º to 40º (Wyllie and Norrish, 1996) and if these values where to be used to calculate the horizontal distance travelled by a rock avalanche the distance calculated would be significantly less than the distance travelled. Since rock avalanches travel further than expected they are said to have an excessive travel distance (Hsu, 1975; Legros, 2002; Ren et al. 2018). This excessive travel distance likely occurs due to a reduction in the coefficient of friction of the rock avalanche material (Legros, 2002; Aaron and McDougall, 2019; Davies et al. 2019), this idea will be discussed later in Chapter 2.

The discontinuities present in the initial rock mass at the slope face appear to dominate the mechanics of the mode of failure (Ramsay, 1967; Matheson and Thompson, 1973; Nichols 1980; Adam, 1982; Pollard and Ayden, 1988; Gudmundsson, 2011; Hencher et al. 2011). These discontinuities will become the failure plane of weakness which the rock mass will eventually fail along and break away from the slope (Hoek and Brown, 1997; Jaeger et al. 2007; Fan et al. 2019). The stability of the initial rock mass before failure is ultimately controlled by the condition and mechanics, such as the intact strength, of these discontinuities (Terzaghi, 1962; Hoek and Brown, 1997; Hoek, 1999; Brideau and Roberts, 2015). Rock avalanche failure triggers are typically caused by an external force such as seismic activity or weathering and erosion acting along the established discontinuities and weakening the rock face to the point of failure (Jibson and Keefer, 1994; Brideau et al. 2005; Dai et al. 2011; Penna et al. 2016; Sandøy et al. 2017; Crosta et al. 2017a).

Figure 2.1 Rockslide Pass in the Mackenzie Mountains is a large rock avalanche with a volume of 450 Mm^3 and travelled about 4.4 km, it is one of the largest rock avalanches to have occurred in the Canadian Cordillera area (Eisbacher, 1979; Google Earth, 2021c).

Various models and statistical relations have been proposed to explain rock avalanche behaviour particularly the apparent reduction in the coefficient of friction and the observed relationship between the horizontal distance travelled and volume. These models and statistical relationships are discussed in the following sections as well as the present knowledge gaps in research completed to date.

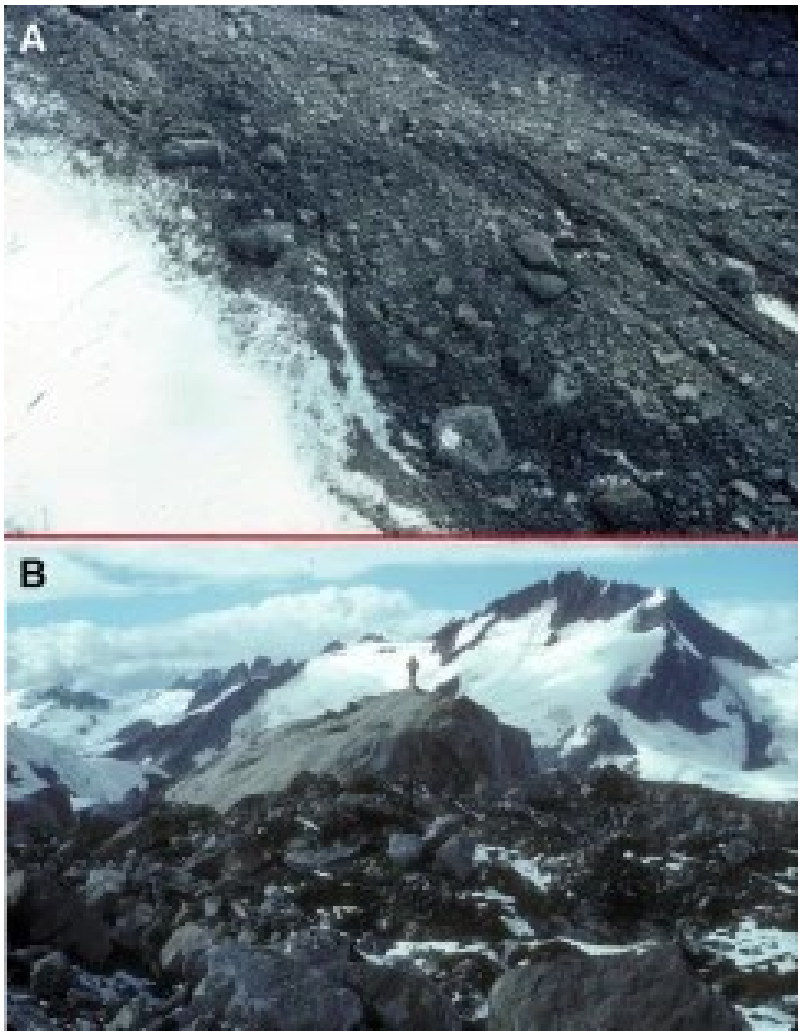

Figure 2.2 A photograph of the 1997 Mount Munday rock avalanche deposit displaying the large degree of fragmentation of the deposit, A displays the grain size range and B shows the size of the large blocks in the deposit relative to a person, image from Delaney and Evans (2014).

2.2 Summary of Current Research

To accurately identify knowledge gaps, it is important to build a complete picture of rock avalanche research reported in the literature.

Rock avalanches typically occur rapidly (often in remote areas) so there is usually no warning of their occurrence (Coe et al. 2016; Schiliro et al. 2019; Zhang et al. 2019). Due to their remote nature, very few rock avalanches are directly observed or recorded however, this is

changing with the introduction of remote sensing techniques such as the use of seismic records and satellite imagery. However, there is still much to learn about the exact behaviours and processes that occur during a rock avalanche (Reznichenko et al. 2017; Busetti-Kirton et al. 2018); the processes that occur in a rock avalanche thus have to be inferred from path geometry and debris characteristics. Various models have been developed to attempt to understand the processes which occur during a rock avalanche and to explain the observed relationships between parameters (Legros, 2002). Models have also been utilised to examine the excessive runout behaviour displayed by rock avalanches (Hungr, 2006; Mitchell et al. 2019; Walter et al. 2020). Mechanistic, numerical, and statistical models have been considered to explain rock avalanche behaviour and are summarised in this chapter.

2.2.1 The Coefficient of Friction

Rock avalanches are rarely recorded with scientific equipment due to their remote nature, as such many parameters are not known and must inferred from field observations (Imre et al. 2010; Li et al. 2012). The parameters such as coefficient of friction must be determined through either laboratory experiments or numerical back-analyses. This has led to competing ideas (Heim's Ratio, laboratory testing, Voellmy's rheology, and a calibrated coefficient of friction) about the best way to calculate the apparent coefficient of friction value for a rock avalanche. The following section will review the various methods utilised in rock avalanche literature to estimate the apparent coefficient of friction value.

As stated in the previous section, the implied coefficient of a rock avalanche is lower than the coefficient of friction of a rock or dry fragmented material of the same composition (Parez and Aharonov, 2015; Aaron and Hungr, 2015; Aaron and McDougall, 2019). Thus, the actual

coefficient of friction value of a rock avalanche is unknown and has not been measured in situ (Aaron and Hungr, 2015; Kang et al. 2017; Wang et al. 2019). The apparent coefficient of friction is considered to be between the rock avalanche body and slope face and between the moving mass and the path surface (Hungr and Morgenstern, 1984; Davies et al. 2019). The internal angle of friction is usually not considered when examining the coefficient of friction value (Davies and McSaveney, 2002; Kelfoun and Druitt, 2005).

From this point forward the coefficient of friction value of a rock avalanche will be called the apparent coefficient of friction value as it is an estimation or approximation of the actual value (Cruden, 1980. The following methods have been utilised to calculate and determine the apparent coefficient of friction value.

The first attempt to calculate the apparent coefficient of friction was the use of Heim's Ratio. Heim's Ratio was derived by Heim (1932) as:

$$\mu = \frac{H}{L} \tag{2.1}$$

where μ is the apparent coefficient of friction, H is the total height or maximum height of which the rock avalanche has travelled and L was the maximum horizontal distance the rock avalanche has travelled (Legros, 2002) as shown in Figure 2.5. The equation proposed by Heim (1932) considered the distance travelled by the centre of mass of the rock avalanche body (Shreve, 1968; Legros, 2002). The original rock avalanche mass geometry is rarely known therefore the location of the centre of mass of the initial rock mass is generally unknown (Legros, 2002). To obtain Heim's Ratio the maximum height and length of the rock avalanche path are used in most rock avalanche literature.

Another way to represent the mobility of rock avalanches is the use of the Fahrböschung or travel angle as shown by a in Figure 2.3 (Delaney and Evans, 2014; Rait and Bowman, 2016). It has been considered as the line which represents the energy lost to friction (Hsu, 1975), and is still used to characterise the extreme distance travelled by rock avalanches (Rait and Bowman, 2016).

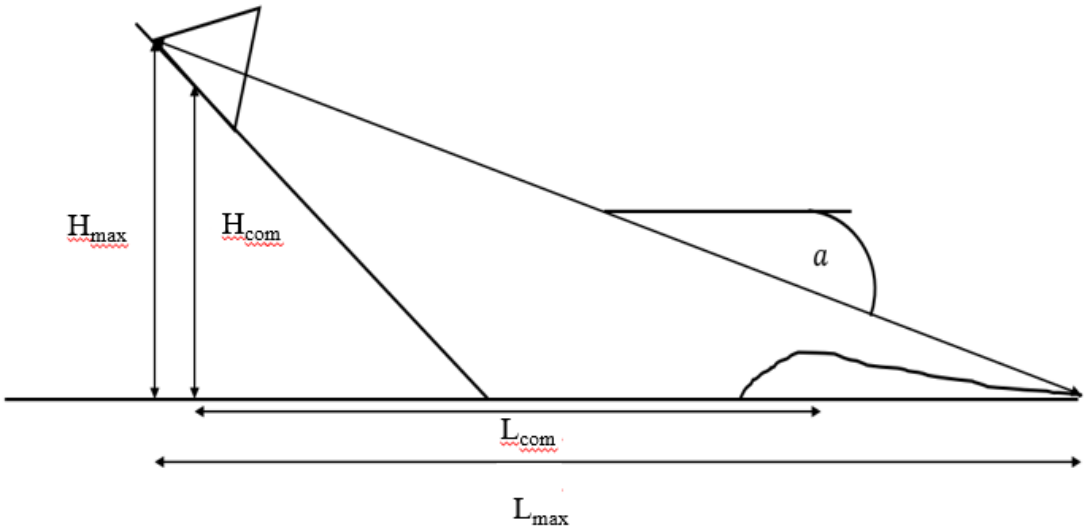

Figure 2.3 A simple representation of a rock avalanche mass before and after failure, H_{max} is the maximum height travelled, L_{max} is the maximum length travelled, H_{com} is the height of the centre of mass, L_{com} is the length travelled by the centre of mass, α is the travel angle or Fahrboschung angle.

It has been assumed that Heim's Ratio was equal to the apparent coefficient of friction of rock avalanches as it quantified the mobility of the rock avalanche body (e.g. De Blasio and Crosta, 2015; Davies et al. 2019; Haug et al. 2020). It was also determined that Heim's Ratio decreased with increase in rock avalanche volume - for that rock avalanche (Legros, 2002; Delaney and Evans, 2014, De Blasio and Crosta, 2015). As stated by Delanney et al. (2015), the use of Heim's Ratio is widely utilised in rock avalanche models. Examples of Heim's Ratio being utilised as the

apparent coefficient of friction value are Locat et al. (2006), Zhao et al. (2017), and Davies et al. (2019).

It was determined through laboratory experiments that utilised coal blocks to represent the rock mass in an avalanche that the horizontal distance travelled was controlled by Heim's Ratio (Bowman et al. 2012). It was further determined through further testing and small-scale rock falls (10^5 m^3) that Heim's Ratio obeys a simple Coulomb friction law (Scheidegger, 1973; Hutter et al. 1995; Bowman et al. 2012; Zhan et al. 2017).

There are some disputes as to the utilization of Heim's Ratio as the apparent coefficient of friction value. Hungr and Morgenstern (1984) studied rock avalanche behaviour and found the apparent coefficient of friction value required to produce accurate horizontal distances was greater than Heim's Ratio of the events studied, i.e. Heim's Ratio underestimated the real coefficient of friction associated with a rock avalanche path. The apparent coefficient of friction value for the model utilised by Davies and McSaveney (2009) had to be calibrated through a back analysis and was lower than the Heim's Ratio value. Further, Barla and Barla (2001) found that the friction angle between a glacier surface and rock avalanche body had to be determined through trial and error for the numerical analysis utilised to produce results which were consistent with field data. The apparent coefficient of friction value determined through trail and error was lower than Heim's Ratio values for the respective events (Barla and Barla, 2001). For the numerical analysis utilised by Favreau et al. (2010) the apparent coefficient of friction value was calibrated to best fit the travel path of the rock avalanche. The calibrated apparent coefficient of friction value was determined to be 0.42 as this yielded a result that followed closely to the path taken by the rock mass. A similar assumption was made by Ji et al. (2020) when completing a numerical analysis to determine the horizontal distance travelled, however a value of 0.48 was considered for the

apparent coefficient of friction term. Moore et al. (2017) found that an assumption of 0.17 for the apparent coefficient of friction model yielded accurate results. Delannay et al. (2017) determined that an apparent coefficient of friction value determined through a back analysis for numerical models would provide an improved estimate of the effective friction value rather than Heim's Ratio. Yamada et al. (2018) found that using a numerical simulation that included three-dimensional topography and mass deformation yielded better results than utilizing Heim's Ratio which does not account for those factors.

Some numerical analyses utilised apparent coefficient of friction values obtained from laboratory testing of rock avalanche debris. Yang et al. (2011) and Yang et al. (2014) determined the apparent coefficient of friction values to be utilised in their numerical analysis from large direct shear tests. Zhang et al. (2020) conducted high-velocity tests at various shear rates to determine the frictional properties of the rupture surfaces and found the friction along these surfaces to be much lower than the Heim's Ratio for the respective rock avalanches.

Another theory considered is the idea that basal shear is the mechanism controlling the friction between the rock avalanche body and the slope face and the moving mass and the path surface. Basal shear is the result of the interaction of the rock avalanche material overriding the low strength path material and low basal shear could potentially result in further travel distances of rock avalanches (Aaron and McDougall, 2019).

There are competing ideas about basal shear and the significance it has on the rock avalanche travel distance (Davies and McSaveney, 1999; Johnson et al. 2016; Zhang et al. 2016; Aaron and McDougall, 2019). Basal shear does appear to affect the mechanics controlling the rock avalanche travel distance as hummocks are often noted in rock avalanche deposits. Paguican et al. (2012) suggested that hummocks form in rock avalanche deposits due to the occurrence of basal

shear. Cagnoli and Piersanti (2015) found that basal shear affects the flow mobility of a rock avalanche when the flow does not occur as a granular column failure. An interesting trend to note is the basal shear values are often found to be higher than the Heim's Ratio values of the rock avalanches (Hsu, 1975; Mollon et al. 2012; Moore et al. 2017). Hsu (1975) and Moore et al. (2017) found that the basal shear value to be about 26°, which is close to the assumed friction angle for a dry fragmented rock of 30°. However, some numerical analyses have suggested that basal shear is not the dictating factor for the excessive runout length observed in rock avalanches (Davies and McSaveney, 1999; Johnson et al. 2016; Zhang et al. 2016).

Another well-known numerical analysis utilised for rock avalanche simulation is the Voellmy rheology which was original derived to model snow avalanches (Voellmy, 1955). The Voellmy rheology utilised in current snow avalanche literature is based on the Voellmy (1955) equation with major modifications completed by Salm (1966, 1972). The Voellmy rheology has been applied to the snow avalanche hazard zones in Switzerland to predict the horizontal distance travelled as well as the final deposit geometry (Bartelt et al. 1999; Schneider et al. 2010).

The Voellmy rheology has been modified and utilised in the simulation of rock avalanches with successful results (Crosta et al. 2004; Hunger and Evans, 1996; Schneider et al. 2010). The Voellmy rheology was modified by Schneider et al. (2010) to represent the resistance along the bottom of the rock avalanche in two dimensions:

$$S_{fx} = \frac{U_x}{\sqrt{U_x^2+U_y^2}}\left[g_z H\mu + \frac{g\left(U_x^2+U_y^2\right)}{\xi}\right] \tag{2.2}$$

$$S_{fy} = \frac{U_y}{\sqrt{U_x^2+U_y^2}}\left[g_z H\mu + \frac{g\left(U_x^2+U_y^2\right)}{\xi}\right] \tag{2.3}$$

where S_{fx} and S_{fy} is the frictional deceleration forces in the x and y directions, U is the mass balance of the event, H is the flow depth, μ is the dry Coulomb friction, and ξ is the velocity-squared turbulent friction. This modification allows for the Voellmy rheology to be utilised to simulate different stages of rock avalanche motion (Hungr, 1990; Schneider et al. 2010). The Voellmy rheology does utilise a coefficient of friction value which is typically calibrated to each rock avalanche in back analysis. The apparent coefficient of friction value has not been experimentally verified (Buser and Frutiger, 1980; Schneider et al. 2010). There are some drawbacks in utilizing the Voellmy rheology as it appears to consistently produce deposits that are thicker than the actual rock avalanche deposits (Crosta et al. 2017a). There is some debate about the accuracy of the velocity of a rock avalanche calculated from models which utilise Voellmy rheology. Strom (2006) noted that when using the Veollmy rheology the velocity values were lower than that of models which did not use the Veollmy rheology. Korner (1976), McLellan and Kaiser (1984) and Hungr (2006) found that models which utilised the Voellmy rheology presented a well-rounded representation of the velocity profile of rock avalanches.

Finally, there is disagreement about the use of a constant apparent coefficient of friction value. As rock avalanches are dynamic processes, the apparent coefficient of friction value should change as the rock avalanche travels to its final position (Haug et al. 2016). Haug et al. (2016) completed experiments showing that the assumption of a constant apparent coefficient of friction value was incorrect and invalid for further experiments completed. Kelfoun and Druitt (2005) determined that models assuming a constant apparent coefficient of friction value fail to produce results which mimicked real world scenarios. The low friction angles required to recreate the observed horizontal distance travelled would not be adequate to allow for deposition on slopes or the preservations of significant morphology in the deposit surface (Kelfoun and Druitt, 2005).

Evans and Hungr (1989) noted however that a dynamic apparent coefficient of friction value does not account for the energy lost to friction.

Various assumptions for the apparent coefficient of friction value are still utilised in current research. The most popular of these is the use of Heim's Ratio as the apparent coefficient of friction value (Delannay et al. 2017). Further research is being completed into the utilization of calibrated apparent coefficient of friction values in place of Heim's Ratio due to improved accuracy of rock avalanche models (Favreau et al. 2010; Delanney et al. 2015; Luo et al. 2019).

From the research completed thus far, it can be determined that there are numerous methods competing methods to determine the apparent coefficient of friction value. Likely the most accurate representation of this value is a value that has been calibrated though either a back analysis or trial error for each event. Further, it is probably that the apparent coefficient of friction is not constant throughout the event as typically assumed in the literature. The apparent coefficient of friction value would change as the rock mass experiences a reduction in grain size, entrains material that is either saturated or unsaturated, or deposits material.

2.2.2 Mechanistic and Numerical Models

Various authors (e.g. Straub, 1997; Crosta et al., 2007; Luo et al. 2019, and others) have put forth a variety of mechanistic and empirical models to explain the excessive runout lengths observed as well as the apparent reduction in the coefficient of friction and its relation to volume. The models are utilized to try and fill in the blanks where information is not available about rock avalanche mechanics (Dufresne et al. 2016a; Dufresne and Dunning, 2017; Luo et al. 2019).

Early rock avalanche models were based on granular flow models, after observing these events on the Moon and Mars (Howard, 1973; Campbell, 1989; McEwen, 1989). The coefficient of friction of a granular flow is reproducible and considered independent of the volume and the path of the rock avalanche (Straub, 1996). This is contrary to other findings from the different numerical analyses where calibrated coefficient of friction values are utilised (Favreau et al. 2010; Delannay et al. 2017; Luo et al. 2019). It has been noted that grain segregation induced a decrease in the coefficient of friction of the rock avalanche (Phillips et al. 2006; Linares-Guerrero et al. 2007; Zhan et al. 2017). The grain-size distribution of a rock avalanche will segregate based on rock type and grain size (Dunning, 2006; Crosta et al. 2007). Granular flows are typically broken down into two major regimes; friction and collisional (Straub, 1997; Campbell, 1989; 1990; Daviesand McSaveney, 1999; De Blasio and Crosta, 2014; Cagnoli and Piersanti, 2015; Lie et al. 2016; Delannay et al. 2017).

The frictional regimes are based on analyzing grain to grain contact during a rock avalanche. Energy is dispersed along the grain to grain contacts and provides the basis of the theory behind force chains (Davies and McSaveney, 2009; De Blasio, 2011; De Blasio and Crosta, 2014). Force chains are chains of grains that are connected vertically due to the overburden pressure during a landslide thus causing intense compressive forces along the chain as shown in Figure 2.4 (Davies and McSaveney, 2009; De Blasio, 2011; De Blasio and Crosta, 2014). Several field observations have found that the stratigraphy of the rock avalanche deposit is often the same as the stratigraphy of the failure plane, supporting the theory of force chains (Shreve 1968; Johnson, 1978; Campbell et al. 1995).

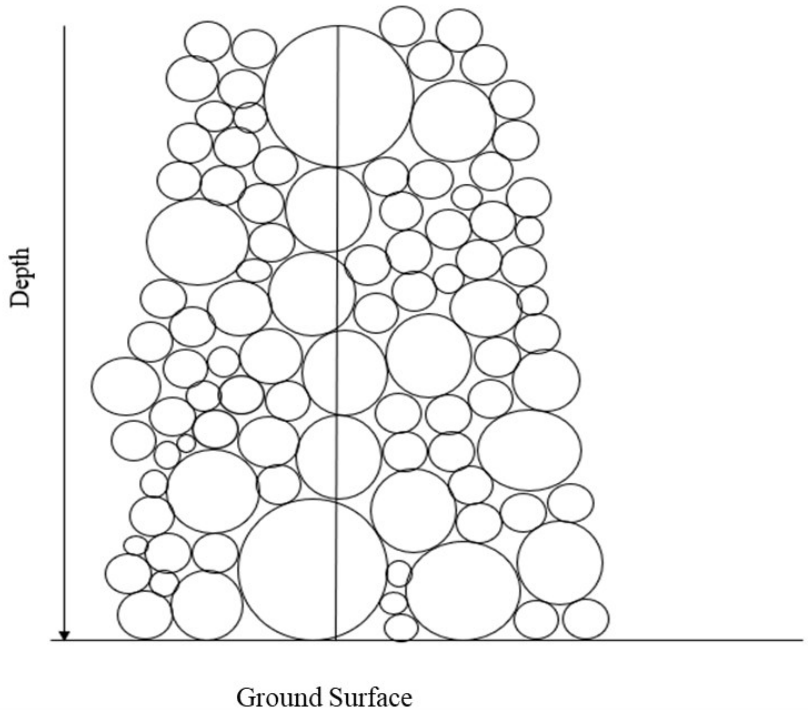

Figure 2.4 Proposed sketch of force chains in a granular medium, the grains align vertically along the vertical line shown due to intense overburden pressure (reproduced after De Blasio and Crosta, 2014).

The collisional regime considers that the grains of a rock avalanche mass are agitated, and energy dissipation occurs during short-lived collisions between grains (Bagnold, 1954; Savage and Hutter, 1989; Hungr and Morgenstern, 1984; Hanes and Inman, 1985). The collisional regime can be represented as:

$$\tau_s = f\sigma D^2 sin\alpha \frac{dU^2}{dy} \tag{2.4}$$

where τ_s is the dissipative shear stress, *dU/dy* is the vertical velocity gradient, *f* is the particle concentration, α is the critical dynamic angle of internal friction, and D is the diameter of the grains (Bagnold, 1954; Savage and Hutter, 1989; Campbell, 1990). For collisional granular flows, the collisions between the particles are assumed to be inelastic, thus a source of energy loss in the

system, however, it is the only energy sink as frictional energy is considered negligible for collision regimes (Legros, 2002). Both of these theories do not provide a sufficient explanation for the excess horizontal distance travel observed in rock avalanches and there are still discrepancies between theoretical models and experimental results, such as discrepancies between the horizontal lengths (Savage and Hutter, 1989; Campbell, 1990; Straub, 1997; Delannay et al. 2017).

Fluids have been theorised to cause a significant reduction of the coefficient of friction of rock avalanches by supporting particles which in turn decreases particle to particle friction (Kent, 1966; Shreve, 1968; Habib, 1975; Goguel, 1978; Johnson, 1978; Voight et al. 1983; De Blasio, 2007; De Blasio, 2009). The fluidization of a rock avalanche body would cause the permeability of the material to increase by decreasing the internal angle of friction, thus increasing the horizontal distance travelled (Wilson, 1984). The presence of fluid in a rock avalanche mass would decrease the normal force on the grains by acting like a lubricant thus lowering the internal angle of friction of the material (Wilson, 1984).

It had been initially suggested that when a rock mass falls away from the slope it traps a layer of air and rides down the travel path on this cushion of air (Kent, 1966, Shreve, 1968). The air would fluidise the rock mass body by passing upwards through the body which would decrease the normal stress causing the excessive travel distances observed (Kent, 1966). Another idea proposed was that the rock avalanche could ride atop the entrapped air rather than the air passing through the rock avalanche body (Shreve, 1968). Shreve (1968) derived an equation to represent this behaviour:

$$p_b = p_t + \sigma_a g s \tag{2.5}$$

where p_b is the pressure in the air layer, p_t is the pressure in the atmosphere, σ_a is the mean bulk density, g is the acceleration due to gravity and s is the thickness. This theory fails to provide an adequate explanation of the relationship observed between the volume and horizontal distance travelled by rock avalanches (Campbell, 1989). This theory has been dispelled by in-field observations of rock avalanche deposits. Air flowing through a rock avalanche body would cause rock avalanche deposits to display normal grading, most rock avalanche deposits instead display an inverse grading (Hungr and Evans, 2004; Wang et al. 2018a; Schiliro et al. 2019; Wang et al. 2020). Rock avalanche deposits may still be fluidised by another fluid besides air as some rock avalanche deposits do display normal grading (Ren et al. 2018).

Another fluid which could have a critical role in the excessive horizontal travel distances observed of rock avalanches is water. Water may be introduced into the rock avalanche material in one of two ways , either by significant rainfall events (Legros, 2002; Delaney and Evans, 2014) or by the heating of the rocks which the rock avalanche travels over (Habib, 1975; Goguel, 1978; De Blasio, 2007; 2014). Wang et al. (2018b) found that the travel path material underneath a rock avalanche body could heat up and release water into the rock avalanche body which supports findings by De Blasio (2007); (2014) and Aaron and McDougall (2019). Wang et al. (2018b) established through further experimentation that this process may be related to the velocity of the rock avalanche. The introduction of water into the rock avalanche body would decrease the friction between the particles and the normal force acting in the rock avalanche body by increasing the pore pressure (Legros, 2002). Further experimentation completed by Yang et al. (2019), found that an inter-granular water film and the related cohesion effects could significantly influence the deposition morphology of rock avalanches that are composed of gravel and ice, even if they were almost dry (Yang et al. 2019). Xu et al. (2012) and Collins and Reid (2019) noted that sand boils

developed throughout the rock avalanche travel path. Sand boils occur due to widespread elevated pore pressures that are caused when the shear strength of the material at the bottom of a rock avalanche reduces. Further, certain layers can liquefy when sheared and thus occur with rapid undrained loading (Collins and Reid, 2019). Lastly, undrained materials would cause gliding friction between the slope and initial mass at the start of the rock avalanche which would cause a decrease in the coefficient of friction (Goren and Aharonov, 2007).

On the contrary, there have been field investigations that suggest that rock avalanches are "dry" or occur without water being present in the rock avalanche body. These dry rock avalanches still had excessive horizontal travel distances as well as an unexplained apparent reduction in the coefficient of as discussed in; Van Gassen and Cruden, (1989), Hungr and Evans (2004), Kelfoun and Druitt (2005), Cagnoli and Piersanti (2015), Parez and Aharonov (2015), and Dufresne et al. (2016b). There have been numerous studies completed of the 2008 Yigong landslides in China, one study found evidence that supports the theory that rock avalanches are "dry". Wang et al. (2018b) noted a lack of flame structures in the Yigong rock avalanche deposit which suggests that liquefaction between the rock avalanche and underplaying materials did not occur. Flame structures occur in saturated unconsolidated sediments and are created when the weight of the overlying strata causes the underlying strata to push up through the overlying strata (Collinson, 1994). Rock avalanches that have occurred on the Moon or Mars would travel without interstitial fluid (Davies, 1981; Campbell et al. 1995; Struab, 1996; 1997).

Another potential cause of liquefaction is the acoustic fluidization of the rock mass as suggested by Melosh (1979). Acoustic fluidization is caused by strong acoustic waves propagating through the rock avalanche body which would momentarily decrease the normal stress of the moving mass (Melosh, 1982; Davies et al. 2007; Davies et al. 2012). Acoustic fluidization assumes

random movements of a group of fragments that form a wave allowing for the rock avalanche to flow in a liquid-like way (Collins and Melosh, 2003). It is thought that acoustic fluidization occurs only in dry masses and in favourable conditions that will facilitate a self-sustaining flow-like motion that would allow for the excessive travel distances observed in rock avalanches (Collins and Melosh, 2003). Further, Collins and Melosh (2003) derived an energy balance equation representing short-wavelength vibrations within a granular medium as shown in equation 2.6:

$$\frac{dE}{dt} = \frac{\xi}{4}\nabla^2 E - e\tau_{ij}\epsilon_{ij} \tag{2.6}$$

where *dE/dt* describes the rate of change of the elastic energy with respect to time, ξ is the scattering diffusivity, $\nabla^2 E$ is the conversion of elastic energy to heat, *e* is the efficiency parameter and $\tau_{ij}\epsilon_{ij}$ is the total rate of energy dissipation (Collins and Melosh, 2003). Collins and Melosh (2003) demonstrated acoustic fluidization by putting a sample on a vibrating plate and conducting shear tests on the sample. To better understand the probability distribution of the vibration frequency which causes liquefaction in rock masses more research is required (Melosh, 1979; Davies, McSaveney and Bolton, 2012). The theory of acoustic fluidization still requires further work to build a model which better represents the behaviours and processes that occur during a rock avalanche since field confirmation for this process has still not been obtained (Collins and Melosh, 2003).

Another mechanistic feature examined is the fragmentation of the original rock mass into the resulting rock avalanche deposit. It has been noted by several field studies that there is an ultra-fine material (less than 100 μm) generated from the rock avalanche and the emplacement of the rock mass (Dunning, 2006; McSaveney and Davies, 2007; De Blasio and Crosta, 2014; Dufresne et al. 2016a; Zhang et al. 2016; Dufresne and Dunning, 2017). Locat et al. (2006) examined the

relationship between the degree of fragmentation and the energy lost to fragmentation utilizing blasting equations. Locat et al. (2006) determined that 2 to 30% of the total energy in the system was lost to fragmentation, through the utilization of equation 2.7:

$$Efrag = 3600wb\forall\rho \tag{2.7}$$

where *Efrag* is the energy lost to fragmentation, *wb* is the work required to blast the material, ∀ is the initial volume of the mass and ρ is the density. This finding is also supported by Crosta et al. (2007), who also noted that fragmentation consumes 1 to 30% of the total energy available in the system. Crosta et al. (2007) utilised the Weibull distribution to quantify rock avalanche fragmentation as shown in equation 2.8 as the Weibull distribution can characterise the probability of fracture for solid particles:

$$\frac{M(>d)}{M_o} = 1 - \exp\left(-\left(\frac{d}{d_o}\right)^2\right) \tag{2.8}$$

where $M(>d)$ is the cumulative mass of fragments finer than d, M_o is the total mass of fragments, and d_o is the size of particle size considered (Crosta et al. 2007). De Blasio et al. (2018) completed a study on rock avalanches and determined that fragmentation consumes 0.2 to 18% of the total energy in the system. The total energy is the energy available to the rock avalanche is typically defined by the amount of energy the system has directly before failure. The importance of this inclusion or calculation of the energy lost to fragmentation in future models was further highlighted by Davies et al. (2019), as the production of fine dust from large boulders requires a large energy sink as observed in equation 2.9:

$$E_s = U(kA_1 - A_0) \tag{2.9}$$

where E_s is the energy lost to fracture-surface fragmentation, U is the specific surface energy, A_0 is the specific surface area of the initial mass, A_1 is the experimentally measured specific surface area of the deposit material samples, and k is the ratio of the specific surface area of the angular grains to the specific surface area of the spherical-equivalent grains (Davies et al. 2019). Davies et al. (2019) calculated that the process potentially consumes more energy than what is available to the rock avalanche. Davies et al. (2019) acknowledged that the model created could have an error in the calculation of the energy consumed by the rock avalanche and concluded that further work was required to determine why the results from their model did not align with field observations. Further, there are four main hypotheses as to how fragmentation is induced: by collision (Deparis et al. 2008; Preuth et al. 2010; Cagnoli and Piersanti, 2017; Zhang et al. 2019), by shear (Davies and McSaveney, 2009; Zhang et al. 2016; Zhang et al. 2019), by a combination of shear and collision (Crosta et al. 2007; Wang et al. 2015; Perinotto et al. 2015) and by high normal stress (Estep and Dufek, 2013; De Blasio and Crosta, 2014, 2015).

It has been noted by Davies et al. (1999) that fragmentation could play a large role as to why rock avalanches experience excessive horizontal travel distances as well as the mass distribution observed in rock avalanche deposits. During fragmentation the initial mass undergoes a drastic grain size reduction which would affect the properties of the rock mass and could potentially enhance the mobility of the rock avalanche through the heating of the materials which it travels over (Habib, 1975; Goguel, 1978; De Blasio, 2007; 2014). The degree of fragmentation appears to play a significant role in the amount of spreading of the rock avalanche deposit (Davies, 1981; Hungr et al. 2002; Aaron and McDougall, 2019). It has been hypothesised and suggested by numerical models that a rapidly decreasing coefficient of friction is likely the cause for the increase in spreading observed with fragmentation (Bowman et al. 2012; De Blasio and Crosta, 2015; Zhao

et al. 2018; Haug et al. 2020). Fragmentation is a necessary component of rock avalanches that should be considered in rock avalanche models; however, this mechanism alone is not sufficient to fully explain the excessive runout distances observed (Haug et al. 2020).

Other numerical models have been utilised to determine the various coefficients and parameters of fragmentation that occurs during a rock avalanche. One such model is the dynamic analysis of rapid mass movement or DAN (Hungr, 1995; Davies and McSaveney, 2002). DAN demonstrated that the increased horizontal distance of large rock avalanches can occur with the normal or expected coefficient of friction value if the internal pressures are higher than normal which would decrease the strength of the rock (Davies and McSaveney, 2002). Equation 2.10 displays the additional lateral pressure term considered in the DAN model to account for the dispersive stress due to fragmentation:

$$p_0 = k_0 \rho g h \tag{2.10}$$

where p_0 is the lateral pressure at depth h beneath the surface, ρ is the density of the material, g is acceleration due to gravity, and k_0 is found empirically (Davies and McSaveney, 2002). Zhao and Liu (2020) utilised a random discrete element analysis to further investigate this mechanism of rock fragmentation when considering uniaxial compression. A random discrete element analysis combines both the discrete element method and random field theory to characterise the spatial variation and uncertainty of microscopic material properties (Zhao and Liu, 2020).

$$F_{bn} = K_{bn} \Delta u_n \tag{2.11}$$

$$F_{bs} = K_{bs} \Delta u_s \tag{2.12}$$

$$M_b = K_b \Delta \theta_b \tag{2.13}$$

$$M_t = K_t \Delta\theta_t \tag{2.14}$$

Where F_{bn} and F_{bs}, are the normal and shear bonding forces, M_b and M_t, are the bending and twisting forces, K_{bn}, K_{bs}, K_b, and K_t, are the respective bonding stiffness, and Δu_n, Δu_s, $\Delta\theta_b$, and $\Delta\theta_t$, are the relative displacements between the bonded particles (Zhao and Liu, 2020). Fragmentation is considered difficult to model as it produces high-velocity fragments which travel in many directions at once. This results in anisotropic dispersive stress within the changing rock mass (Davies et al. 1999). As well the horizontal distance travelled by the rock avalanche appears to be determined by a combination of spreading and internal friction (Haug et al. 2020).

Several models have been created utilizing various numerical analyses to examine rock avalanche behaviour. Numerical analyses are utilised in research as they can account for three-dimensional topography changes and mass deformation (Yamada et al. 2018). Discrete element analyses have been used to successfully model various rock avalanches as shown by: Okura et al. (2000), Pirulli et al. (2003), Taboada et al. (2005), Taboada et al. (2006), Tang et al. (2009b), Richefu et al. (2012), Li et al. (2012), Zhang et al. (2019). A few of these numerical models have focused on the seismic signals created during a rock avalanche and the utilization of these signals to determine various parameters of the studied rock avalanches (Brodsky et al. 2003; Erkström and Stark 2013; Hibert et al. 2016; Favreau et al. 2010; 2018; Wang et al. 2020). The seismic recording of a rock avalanche is inverted and with the application of numerical simulations the dynamic evolution of the coefficient of friction can be determined (Allstadt 2013; Coe et al. 2016; Bai et al. 2018). From the seismic wave recordings, it is possible to determine the number of events that have occurred, when the events took place, the velocity, volume, direction, and the coefficient of friction (Yamada et al. 2018; Dufresne et al. 2019). An example of a calculation utilizing parameters gained from the inversion of the seismic record is shown in equation 2.11 which was

derived by Moretti et al. (2020). Equation 2.15 displays the calculation of the determination of the initial failure plane slope angle of the rock avalanche event:

$$\theta = \arctan\left(\frac{F_z}{F_h}\right) \tag{2.15}$$

where F_z is the vertical force amplitude and F_h is the horizontal force amplitude (Moretti et al. 2020).

Discrete element method (DEM) is another numerical model which is utilised to represent the complex dynamics of rock avalanches and fragmentation characteristics as shown by: Mead and Cleary (2015), Johnson and Campbell (2017), Moore et al. (2017), Zhao et al. (2018), Ge et al. (2019). It was determined by Kesseler (2020) that the particle shape of the grains could be accounted for by utilizing rolling resistance rather than coefficient of friction and that the discrete element model (DEM) scaled with Reynolds Number. The DEM utilised by Kesseler (2020) considered rolling-resistance rather than the coefficient of friction to allow for a quick simulation of the laboratory experiments. Further, DEM's have been utilised successfully to model dynamic fragmentation, trajectories of rock blocks, and energy dissipation (Favreau et al. 2010; Moretti et al. 2012; Mead and Cleary, 2015; Moretti et al. 2015; Zhao et al. 2018). Mollon et al. (2012) utilised DEM's to represent friction laws and simple contact between grains and discovered that a wide range of complex rock avalanche behaviours could be potentially described with great accuracy. Zhao and Liu (2020) utilised a random discrete element analysis to explore rock fragmentation behaviour during uniaxial compression.

Numerical models have also been utilised to examine the entrainment effect noted in various field studies of rock avalanches (Hungr and Evans, 2004; Delaney and Evans, 2014; Fan et al. 2019; Hu et al. 2019; Huang et al. 2019; Liu et al. 2019; Singeisen et al. 2020). Entrainment

is described as a ploughing motion in which the rock avalanche body gathers substrate from the travel path and pushes or ploughs the material in front of the rock avalanche body to its resting location (Crosta et al. 2009; Farin et al. 2014; Hu et al. 2019; Shen et al. 2019). Further, it has been observed that path material influences the horizontal distance travelled by a rock avalanche (Wang, Dong and Cheng, 2018; Aaron and McDougall, 2019). Entrainment causes the final volume of a rock avalanche to increase when compared with the initial failure mass. Further, it appears that entrainment causes an increase in the horizontal distance travelled (Hu et al. 2019; Liu et al. 2019). Crosta et al. (2009) noted the opposite effect, that entrainment of dry materials reduced the total rock avalanche travel distance, and the entrainment of substrate material became complex to model. There is some debate as to the prevalence of entrainment in rock avalanches as it has been noted by Walter (2020) that entrainment may not lead to an excessive travel distance. Farin et al. (2014) observed that rock avalanches in general often excavate substrate material and that the entrainment process is not uniform.

Shen et al. (2019) further simplified entrainment motion into a two-layer finite model which simulated the frontal ploughing, erosion of the mass, and sliding of the rock avalanche body. The interaction between the rock avalanche body and the erodible mass is simulated utilizing the normal force and shear force which acts between the contact of the rock avalanche body and travel path as observed in equation 2.16 (Shen et al. 2019):

$$\frac{dh_i}{dt} + \frac{dQ_{xi}}{dx} + \frac{dQ_{yi}}{dy} = 0 \tag{2.16}$$

where h is the height of the soil column, t is time, and Q_{xi} and Q_{yi} are the flow quantities in the x and y directions (Shen et al. 2019). Numerical models have been utilised to calculate total avalanche momentum, total kinetic energy, and total frictional energy of rock avalanches

(Schneider et al. 2010). Delannay et al. (2017) utilised basic physical principles based on equations that focus on the laws of mass and momentum shown in equations 2.17 and 2.18. These equations were utilised to describe the mechanical behaviour of a rock avalanche (Delannay et al. 2017):

$$F_d = C\left(u_f - u_p\right), \tag{2.17}$$

$$F_L \approx \left(\frac{3\pi}{2}\right)\eta_f \frac{\delta u_p}{h}, \tag{2.18}$$

where F_d, is the fluid resistance force, u_p and u_f are the velocities of the particle and fluid, C is dependent on various parameters related to the rock avalanche, F_L is the lubrication force, η_f is the fluid dynamic viscosity, h is the gap between the particles and δu_p is the relative approaching velocity (Delannay et al. 2017).

Various rock avalanche deposit features (e.g. the flow evolution of a granular mass and deposition) have been modelled using numerical analyses and various coefficient of friction values (Crosta et al. 2017a). Most numerical models of individual events utilised a calibrated coefficient of friction value. The calibrated coefficient of friction value was calculated using a back analysis and real (Delannay et al. 2017; Mergili et al. 2020).

Fuchs et al. (2018) considered creating a scaling law to relate rock avalanche magnitude with earthquake magnitudes, similar to the Richter scale. Currently, this is not able to be completed due to a lack of data and events in the literature about rock avalanches.

Energy models are a form of numerical models that have been considered for simulating large rock avalanches and the various behaviours and mechanics that occur during a rock avalanche event (Kang et al. 2017; Davies et al. 2019). An energy model which considered entrainment was created for the 2008 Yigong rock avalanche. The model considers both rolling and sliding motions

to determine the volume of material eroded (Kang et al. 2017). Davies et al. (2019) created a rock avalanche model using an energy budget that consisted of considerations for potential energy, frictional energy, and fragmentation energy. The model created however had shortcomings since it was found that there was insufficient energy in the system to account for the energy lost to fragmentation (Davies et al. 2019).

An important detail to note is that many numerical rock avalanche models created are designed for a specific rock avalanche (Kelfoun and Druitt, 2005; Ge et al. 2019; Mergili et al. 2020). When these models are utilised for other rock avalanches that do not share key similarities, the models tend to over or underestimate the travel distance and miscalculate other key elements of rock avalanche behaviour (e.g. how the failure mass evolves into a high velocity flow) (Van Gassen and Cruden, 1989).

Nicoletti and Sorriso-Volva (1991) and Straub (1996) noted that utilizing the coefficient of friction to determine the path geometry is insufficient as it does not account for the external factors (e.g. failure method, geology, initial conditions and others) which can affect rock avalanche travel distance. Nicolette and Sorriso-Volva (1991) completed a preliminary analysis to determine how external factors such as rock lithology and environment can affect the distance travelled by a rock avalanche. It was noted that these external factors do indeed affect the horizontal distance travelled and should be considered when developing rock avalanche models. Viero et al. (2012) and Mitchell et al. (2019) confirmed that external factors such as environment and topography affect the horizontal distance travelled by a rock avalanche.

It was determined that the environment, lithology and topography can affect the horizontal distance travelled by a rock avalanche (Strom, 2015; Charriere et al. 2015). Rock avalanches that occur in volcanic environments typically travel much farther than those that occur in other

environments (Legros, 2002). Entrainment has also been found to be dependent on the environment in which the rock avalanche occurs. The types of material being entrained by the rock avalanche will vary depending on the environment and can affect the horizontal distance travelled (Hungr and Evans, 2004; Sosia et al. 2012; Pudasaini and Krautblatter, 2014). Further, Zhang et al. (2019) found that various rock avalanche features are dependent on the initial lithology of the rock avalanche.

Rock avalanches that occur on glaciers were found to be mobile large failures that typically involved both rock fragments and ice (De Blasio, 2014; Deline et al. 2015; Evans and Delaney, 2015; Su et al. 2019). When the rock avalanche travels along a glacier it will incorporate snow and ice into the rock avalanche body which is likely immediately melted upon incorporation into the mass, further observations show that ice is not present in the final deposit (Mergilie et al. 2020; Walter et al. 2020). It has been further noted by Mitchell et al. (2019) that snow and ice can enhance the mobility of a rock avalanche by reducing the coefficient of friction which could be an explanation for the excessive travel distances displayed by these events.

Local terrain characteristics can control both the shape and mobility of rock avalanches through confined or unconfined topography (Nicoletti and Sorriso-Volva, 1991). Through the examination of the environmental characteristics, it is possible to determine how the deposit formed (Luo et al. 2019; Zhu et al. 2020). Investigations of the environment and topography which the rock avalanches occur have found that the degree of confinement directly affects the degree of spreading observed as well as the travel path of the rock avalanche (Shaller, 1991; Paguican et al. 2012; Walter et al. 2020). As the confinement of a rock avalanche increases the spreading observed of the deposit will decrease and the horizontal distance travel will increase when compared with an unconfined rock avalanche (Shaller, 1991; Walter et al. 2020; Zhu et al. 2020). This behaviour

can be shown in the case of two rock avalanches in the Mackenzie Mountains as displayed in Figure 2.5.

Various rock avalanche deposit features can be utilised to infer various mechanics that control the movement of the event. Hummocks tend to appear in rock avalanche deposits in which the rock avalanche experienced basal shear (Paguican et al. 2012). The grading observed in a deposit, either normal or reverse, can be utilised to infer if liquefaction of the rock avalanche materials occurred during transportation. The grain size of the rock avalanche also appears to affect the segregation observed in the deposit (Bartali et al. 2020).

There are few opportunities to observe the interior of rock avalanches; cross-sections that have been exposed by erosion can be used to examine the structure of rock avalanche deposits (Zhang et al. 2016; Haung et al. 2018; Zhang et al. 2019). Samples for grain size analysis and laboratory testing (Zhan et al. 2017; Luo et al. 2019; 2020; Bartali et al. 2020) are taken and provide a wide spectrum of mechanical flow information and allows for individual parameters to be investigated under controlled conditions (Yang et al. 2019).

Through a grain size analysis, Luo et al. (2019) determined that sand grains in rock avalanche deposits are mostly spherical, other grains in the deposit were found to be sub angular apart from slaty clay minerals. Many of the grains were under 0.075mm with the slaty clay minerals being smaller than 0.005mm. Davies et al. (2019) found similar results upon the investigation of a rock avalanche that had occurred in New Zealand. Luo et al. (2020) found that the degree of weathering of the deposit was made up of 12 different size classes of clasts. These ranged from metres-sized boulders to fines less than 25 micrometres. It was determined that the debris can be divided into two groups: fresh and weathered. Fresh debris was created from the fragmentation of the initial failure mass, and weathered material was either already present at the

initiation of the event or entrained by the failure mass. The fresh debris accounts for 80% of the weight of the rock avalanche deposit and appears necessary for a rock avalanche to occur (Luo et al. 2020).

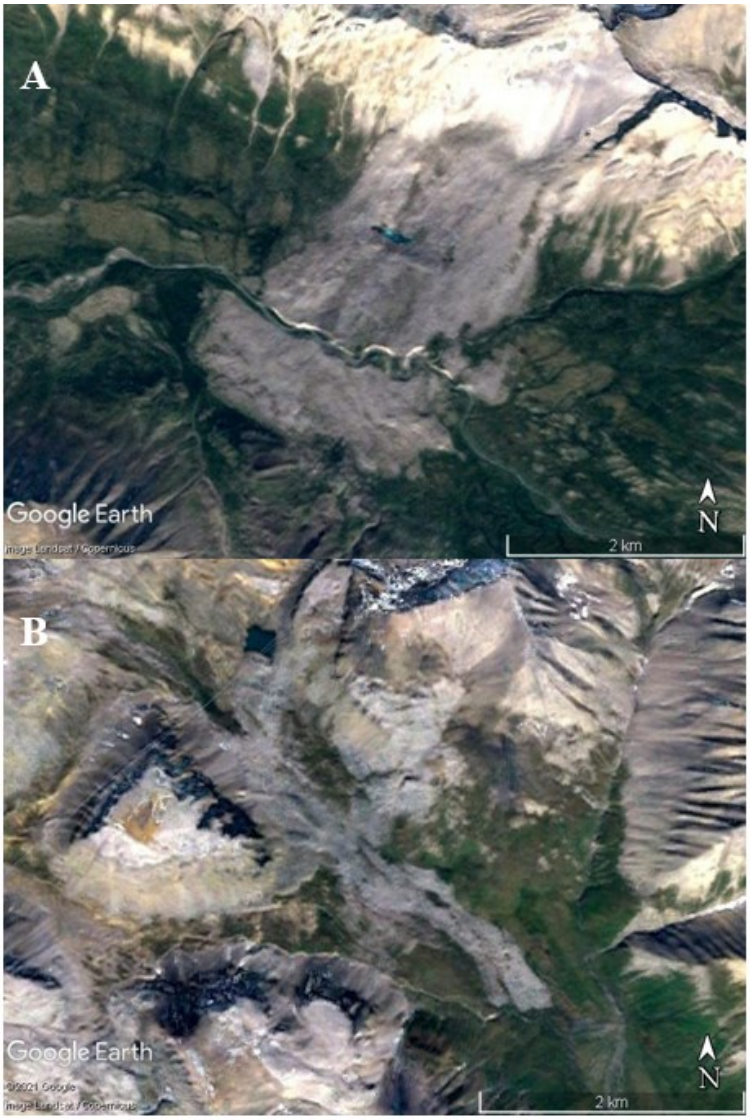

Figure 2.5 Comparison of two rock avalanche events in the Mackenzie Mountains, A is the Bonnet Plume rock avalanche and displays the large deposit area of an unconfined event whereas B is the Damocles Slide and shows the narrow deposit of a laterally confined event (Google Earth, 2021a, Google Earth, 2021b).

An experiment was completed using a flume and coal blocks to simulate the dynamic fragmentation undergone by rock avalanches and was observed that the runout obeyed Heim's Ratio (Bowman et al. 2012). Heim's Ratio will be discussed in Section 2.2.2. It was found that the Heim's Ratio only obeys a simple Coulomb friction law through the use of flume tests that simulated rockfalls (Hutter et al. 1995; Zhao et al. 2017).

Further laboratory tests were carried out by Lin et al. (2020); it determined that the initial lithology and conditions (e.g. geology, weathering, jointing, bedding and others) of the source rock can greatly influence the impact of fragmentation and the total distance travelled. Further, it was found that the degree of fragmentation controls the distance travelled by the centre of the mass (Lin et al. 2020). Fragmentation appears to be an energy sinking process that will shorten the horizontal distance travelled by the rock avalanche, thus it alone is not the reason why rock avalanches exhibit excessively long travel distances. It was further determined that the runout of the centre of mass decreased with an increasing degree of fragmentation (Lin et al. 2020). Lastly, the occurrence of discontinuities along the sliding surface appears to enhance the travel distance of the front of the rock mass as the fines appear to be able to travel farther distances (Lin et al. 2020).

De Blasio and Crosta (2013) argued that flume tests are not capable of capturing the key features of these events due to the degree of fragmentation which rock avalanches undergo. This degree of fragmentation is often overlooked in laboratory experiments as the energy for fragmentation in the experiments is drastically lower than that of a rock avalanche. Further, the observations made from the models created by De Blasio and Crosta (2013) show a further degree of fragmentation than the flume tests completed. De Blasio and Crosta (2013) argue that the small

size of the laboratory set up for the flume tests could not accurately account for all processes that occur during a rock avalanche such as force chains.

Another important relation to note is the maximum and mean velocity of the rock avalanches appears to increase with increasing volume (Lucas et al. 2014). Further research has shown that the coefficient of friction may be dependent on the velocity at which the rock avalanche travels (Dong et al. 2013; Wang, Dong and Chong, 2017; DeGiuli and Wyatt, 2017). Lucas et al. (2014) found through a 3D analytical simulation that the effective friction decreases with increasing velocity and there appears to be an apparent relationship between the velocity and volume.

Since rock avalanches are rarely measured or observed as they occur it is difficult to determine the accuracy of the various models (Imre et al. 2010; Li et al. 2012; Dufresne et al. 2016b). The lack of infield observations of a rock avalanche has led to a lively discussion on actual emplacement, kinematic and dynamic mechanisms (Zhu et al. 2020). Due to the lack of direct in-field observations of rock avalanches it is difficult to determine various parameters such as the coefficient of friction, which would pertinent to current research (Zhang et al. 2019). Thus, the current models may replicate the correct answer through an incorrect simulation of the various mechanics which occur during a rock avalanche (Moretti et al. 2020).

For rock avalanches that exhibit long travel distances, extreme fragmentation, and rapid movement, a continuum method of modelling would not work as it is disadvantaged in modelling these scenarios (Zhang et al. 2019). Continuum methods are based on fluid mechanics and assumed the granular material of the rock avalanche body is a solid block that is not affected by natural discontinuities, this would not provide an accurate representation of the rock avalanche body (Zhang et al. 2019). Secondly, the mechanisms of rock avalanche transport have been studied for

decades and remain a challenging research topic in the scientific community (Zhang et al. 2019). For most rock avalanche models, further research is required to understand the various mechanics of rock avalanches and their behaviours (Mergili et al. 2020).

From the work completed thus far on rock avalanches, there are still significant gaps in knowledge as to how certain mechanics or processes affect the horizontal distance travelled. The main areas which require research are:

1. It is still not well understood how **fragmentation** occurs in a rock avalanche and how it affects the horizontal distance travelled. Further, there is still disagreement about the amount of energy lost to this process and how it affects the distance travelled.
2. There is still debate about **entrainment** and its effects on rock avalanche behaviour. Various models consider entrainment an energy loss term, while other models consider entrainment to be an energy gain.
3. Further research into how the **environment** in which a rock avalanche occurs affects the horizontal distance travelled is required. There is preliminary evidence to show that geology, lateral confinement, and environment are all processes that can dictate the horizontal distance travelled.

2.2.3 Empirical Models

McDougall (2016) suggested that the most practical empirical methods are based on simple geometric correlations.

Empirical models have been considered alongside mechanistic and numerical analyses to examine both the excessive horizontal distances travelled by rock avalanches and the apparent correlation between volume and the horizontal distance travelled.

A well-documented parameter relationship to note is the apparent inverse correlation between volume and Heim's Ratio, i.e., as volume increases Heim's Ratio decreases (Scheideggar, 1973; Pollet et al. 2011; De Blasio and Crosta, 2014; Mitchell and McDougall, 2018). The second relationship observed is between the horizontal distance travelled and the volume of a rock avalanche, i.e., as the volume increases, the horizontal distance travelled also increases (Davies, 1982; Hsu, 1975; Hungr, 2006). The third relationship is between the volume and the deposit area of a rock avalanche, i.e., as the volume increases so does the deposit area of the rock avalanche (Dade and Huppert, 1998; Delaney and Evans, 2014). The Legros (2002) database has been utilised to create a sample of the relationships observed, as shown in Figures 2.6 to 2.8. (cf. Hungr, 2006; Delaney and Evans, 2014; Mitchell et al. 2018).

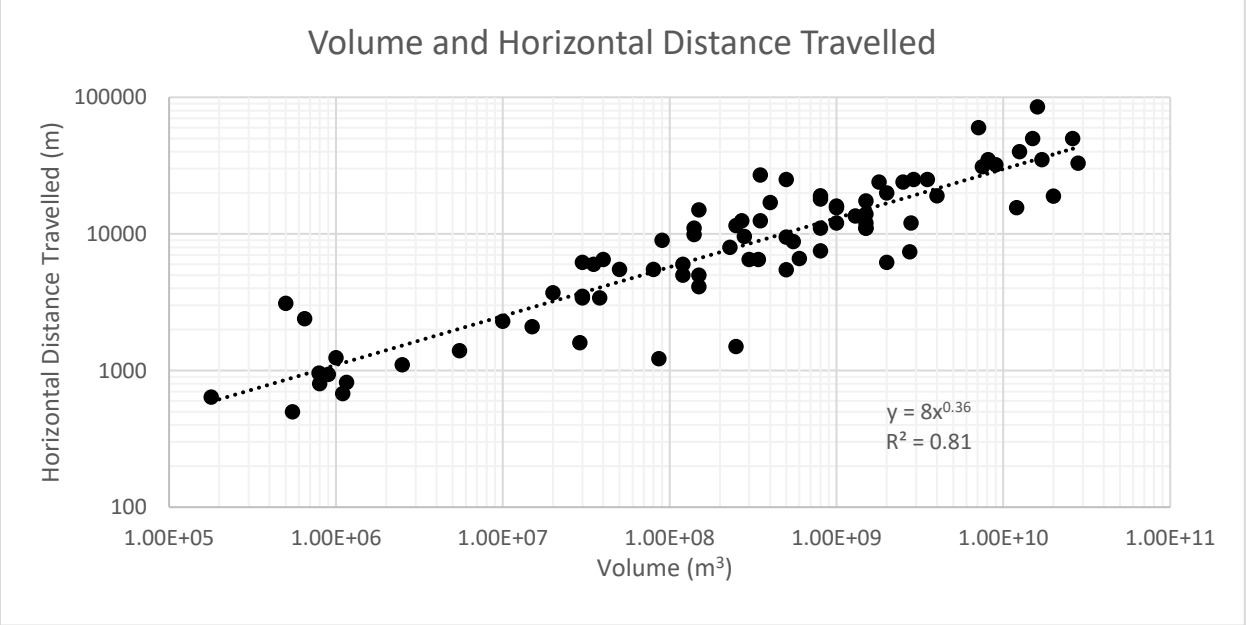

Figure 2.6 The relationship between Volume and the Horizontal Distance Travelled utilizing Legros (2002) database, the slope of the trendline of 0.36. N = 81

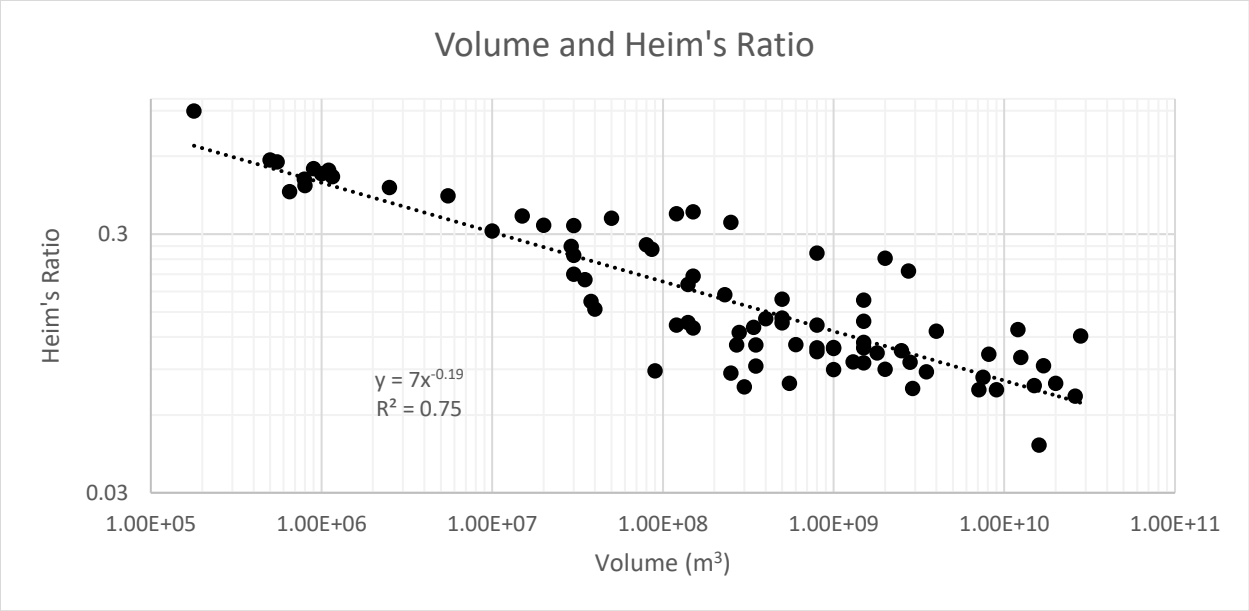

Figure 2.7 The relationship between Volume and Heim's Ratio utilizing the Legros (2002) database, as the Volume increases Heim's Ratio decreases. N = 81

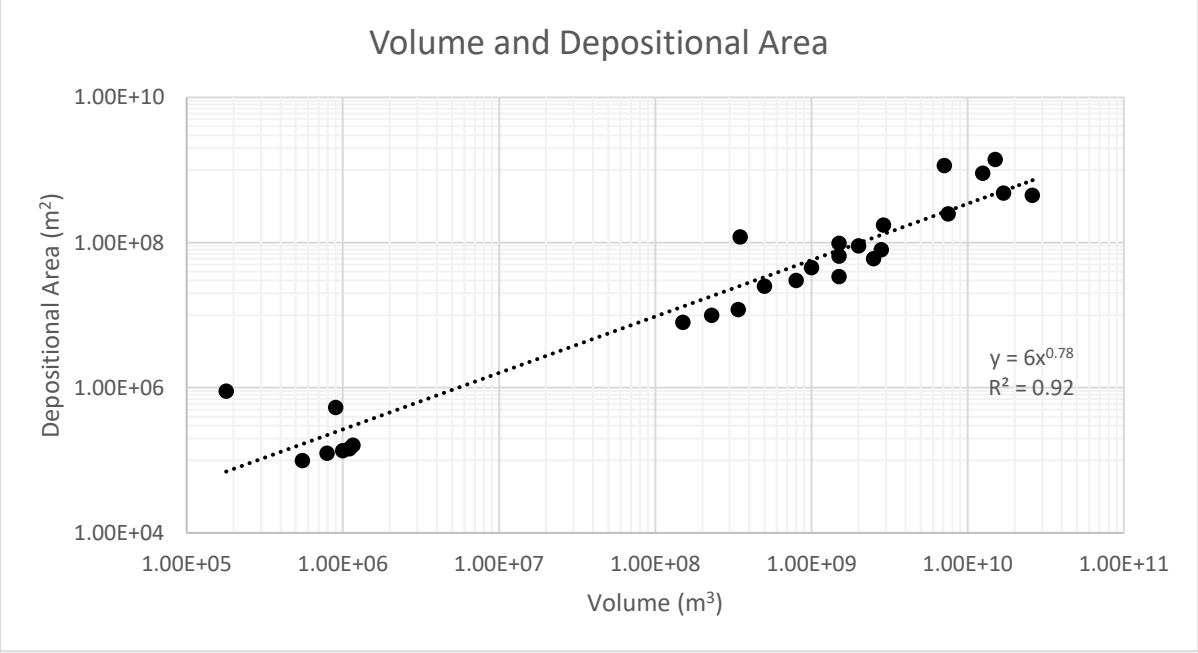

Figure 2.8 The relationship between Volume and the Depositional Area of the rock avalanche utilizing Legros (2002) database, as the Volume increases, so does the depositional area. N = 27

An empirical model was set forth by Delaney and Evans, (2014) to describe the overserved relationship between volume and the horizontal distance travelled by a rock avalanche. The relationship between the volume and horizontal distance travelled has been noted by various authors (Abele, 1974; Hungr, 2006; Sosio et al., 2012), however Delaney and Evans (2014) were the first to quantify the relationship. Delaney and Evans (2014) quantified the relationship through the use of Galileo Scaling. Delaney and Evans (2014) noted that the relationship between the volume and horizontal distance was bound by a square-cube law. A square-cube law was derived by Galilei (1638) to describe the relationship between the surface area and the volume of an object when the volume of said object is changed. It states that as the size of the object is increased, the volume will increase at a greater rate proportional to the surface area (Galilei, 1638). This can be related back to the volume and the horizontal distance travelled by a rock avalanche, as the volume increases, the horizontal distance travelled would increase at a rate proportional to the increase in volume (Delaney and Evans, 2014). It was expected that the slope of the trendline of the dataset would be 0.33 (Delaney and Evans, 2014), and from Figure 2.6 the slope of the trendline is 0.36 displaying that the relationship observed between volume and horizontal distance travelled does follow Galileo Scaling.

Abele (1974), Hsu (1975), Li (1983) and Legros (2002) tried to quantify the relationships between volume and Heim's Ratio, and volume and depositional area by examining the slope of the trendline of the Figures. It was determined that the scaling factor for the relationship between volume and Heim's Ratio changes depending on the environment in which the rock avalanche occurred, with a slope of 0.66 for non-glacial environments and a slope of 0.33 for glacial environments (Hungr, 1990; Dade and Huppert, 1998; Legros, 2002; Delaney and Evans, 2014). The scatter in these graphs however is large and spans multiple orders of magnitude (DeMatos,

1987; Hsu,1975; Hungr, 2006). Haug et al., (2020) noted that for a similar volume the horizontal distance travelled is observed to span several orders of magnitudes, which suggests additional unaccounted controlling factors.

Dufresne and Geertsema (2020) completed further research on the relationships between the volume and coefficient of friction and found that a complex analysis was required to confirm the correlation. The relationship between volume and the horizontal distance travelled has been proposed as a potential prediction tool for determining how far a potential rock avalanche will travel (Hungr, 2006; Mitchell et al., 2018). It has been noted by Mitchell et al. (2018) that there is a large scatter in data when plotting the volume and Heim's Ratio relationship. Abele (1974), Corominas (1996), and Nicolleti and Sorriso-Valvo (1991) attempted to reduce scatter in data by creating smaller databases based on confinement, topography, environment, and failure method. These smaller databases were found to have higher R^2 values than the original plot which featured all rock avalanches (Corominas, 1996). This relationship has been utilised as a prediction tool for determining the potential runout for freshly excavated faces in open pit mining (Whittall, 2019). Corominas (1996), Hungr (2006) and Mitchell et al. (2018) noted that improved correlations still had considerable errors. These errors could be attributed to the vagaries of reported volumes of rock avalanches particularly in cases in which the rock avalanche gains volume through entrainment. Some researchers question the validity of utilizing the square-cubed law to quantify rock avalanche behaviour as it may not be representative of all external factors which can affect the horizontal distance travelled (e.g. Hungr, 2006; Legros, 2002).

2.3 Current Work

The following sections will outline the current knowledge gaps in the research summarised in Section 2.1.

2.3.1 Apparent Coefficient of Friction

The use of Heim's Ratio as the apparent coefficient of friction value is widespread and is often utilised in rock avalanche models (e.g., Delannay et al., 2017, Davies et al., 2019). However, the use of a calibrated apparent coefficient of friction values, calculated in back-analysis, has gained popularity in more recent literature. Calibrated apparent coefficient of friction values have been found to increase the success of numerical simulations (Delannay et al., 2017). However, these calibrated values must be retroactively calculated from the rock avalanche in which they are being used to model after they have taken place (Favreau et al., 2010; Delannay et al., 2017). It is difficult to model rock avalanches that have not yet occurred utilizing the same numerical methodology. The apparent coefficient of friction value would have to be estimated in these scenarios.

There is disagreement about which rheological model provides the best results when considered for various numerical analyses. McSaveney (1978) and Crosta et al. (2017) found that the use of Bingham rheology provided better results than that of Voellmy's rheology or Heim's Ratio. Hungr (2006) and Sosio et al. (2012) found that Voellmy's rheology provided better results than both Heim's Ratio and Bingham. Further research is required into the apparent coefficient of friction and which method would provide the best results for numerical simulations and back analyses.

2.3.2 Rock Avalanche Behaviours

There is knowledge lacking about how entrainment, deposition, fragmentation, and impact affect the horizontal distance travelled of a rock avalanche.

There is a dispute as to how the volume increase due to entrainment affects the horizontal distance travelled by a rock avalanche. Liu et al. (2019) and Hu et al. (2019) both stated that an increase in volume due to entrainment would increase the horizontal distance travelled. Crosta et al. (2009) suggest a contrast that an increase in volume would decrease the horizontal distance travelled as entrainment is a complex motion that has consequences for the rock avalanche body. Furthermore, it is difficult to determine exactly how much material a rock avalanche gains during its transportation from its initial position to its resting place (Crosta et al., 2009; Hu et al., 2019; Liu et al., 2019). Walter (2020) concludes that entrainment does not have a large role in changing the horizontal distance travelled by a rock avalanche.

For fragmentation, there are competing ideas as to how much energy is lost to the process and the best method of calculation (e.g. Locat et al., 2006; Davies et al., 2019). Locat et al. (2006) utilised blasting equations to quantify the energy lost to fragmentation and found that 1 to 30% of the total energy in the system was lost to this process. Davies et al. (2019) found through energy and momentum equations that there was not enough energy available to the system to account for the energy lost to fragmentation.

As well, little work has been completed to determine the energy lost to impact when the rock mass breaks away from the failure surface and crashes onto the slope below. This could potentially be a large energy sink as well as the source of the majority of fragmentation that occurs during a rock avalanche (Lin et al., 2020). Research is required to determine the exact role that

impact has on the energy losses and gains for rock avalanches and ultimately how it affects the total horizontal distance travelled by a rock avalanche.

2.3.3 Statistical Relationships

There appears to be a lack of consensus about the usefulness of the apparent square-cube law relationship observed between the volume and the horizontal distance travelled. Corominas (1996), Dade and Huppert (1998) and Delaney and Evans (2014) found that the use of smaller, well-constrained databases yielded plots that displayed less scatter about the trendline. The scatter of these smaller datasets was noticeably less when compared with a large dataset encompassing multiple topographies, environments, and failure types.

When examining the relationship between volume and the apparent coefficient of friction as defined by Heim's Ratio, Hsu (1975), DeMatos (1987) and Hungr (2004) argue that this relationship is not of value for prediction if the rock avalanche is not controlled by frictional properties.

The scatter observed with these graphs is not well understood, but some hypotheses have been proposed. It may be that the recorded volume of the rock avalanches is not accurate (e.g., Hungr, 2006). The volumes of rock avalanches are calculated through a variety of methods that can raise uncertainty in these calculations as there is no generally applicable method for calculating rock avalanche volume (Hungr, 2004). Dade and Huppert (1998) theorised that the scatter observed was due to varying obstacles and topographic constraints between different rock avalanches. Many rock avalanches lack sufficient data or poorly conditioned data due to lack of identifying information (Corominas, 1996). On some occasions, rock avalanches are listed without

site coordinates, as observed in the database created by Eisbacher (1979) and Legros (2002). Without site coordinates, it is difficult to locate the rock avalanche deposits and confirm that the data provided is correct.

While the data sparsity is difficult to remedy, constraining databases could potentially generate insightful information about the observed square-cube law between volume, Heim's Ratio and the horizontal distance travelled

2.2.4 Summary of Knowledge Gaps

The following areas require further research as highlighted by the literature review:

1. There have been various models put forth to represent rock avalanche **fragmentation**. These models do not agree as to how much energy is consumed by this process and how rock avalanche fragmentation affects the horizontal distance travelled event.
2. It is still debated if energy is lost or gained when a rock avalanche incorporates new mass during the event. Further, there are still active discussions as to if **entrainment** would cause a rock avalanche to travel farther than a rock avalanche that did not gain new material.
3. Further work is required to quantitively determine how the **environment** affects the horizontal distance travelled by a rock avalanche. It has been noted that the environment, degree of lateral confinement, geology and the failure trigger and mechanism may all affect the horizontal distance travelled yet these parameters are rarely considered in models.

4. A single method for calculating the **apparent coefficient of friction** has yet to be adopted in rock avalanche literature, leading to potential errors between the multiple methods of calculation. Moreover, it is assumed that the apparent coefficient of friction of a rock avalanche stays constant throughout the event. This assumption may be inaccurate as the coefficient of friction likely changes depending on the processes that occur during a rock avalanche.
5. **Galileo Scaling** could explain the observed relationship between volume and the horizontal distance travelled; however, data sparsity does not allow for an in-depth analysis. Rock avalanche databases often do not include information beyond the event name and the rock avalanche fall height and horizontal distance travelled. The geological setting is typically overlooked. Including these parameters would allow for the creation of smaller datasets that represent rock avalanches with similar behaviours and the analysis of these smaller datasets could improve the understanding of the relationship between volume and the horizontal distance travelled.

Chapter 3 : Insights of Rock Avalanche Behaviour from Simple Physics

3.1 Introduction

The mechanics and behaviours of individual rock avalanches are not well understood, especially how these mechanics pertain to the horizontal distance travelled (Legros, 2002). To address this knowledge gap energy models based on simple physics were used to investigate the individual rock avalanche behaviours which dictate the horizontal distance travelled. Investigating the case-specific behaviours allows for a better understanding of which parameters control the distance travelled by a rock avalanche.

The simple physics energy models created each focus on a different mechanism of rock avalanches and how various parameters in these models dictate the horizontal distance travelled. The five models presented in this chapter are sliding, entrainment deposition, rock fragmentation and impact. These five behaviours have been noted in most rock avalanches (Hungr et al., 2001; Legros, 2002; Dunning, 2006; Locat et al., 2006; Crosta et al., 2007; McSaveney and Davies, 2007; De Blasio and Crosta, 2014; Delaney and Evans, 2014; Farin et al., 2014; Deline et al., 2015; Dufresne et al., 2016b; Haug et al., 2016; Dufresne and Dunning, 2017; Zhang and McSaveney, 2017; Ren et al., 2018; Zhao et al., 2018; Davies et al., 2019; Zhang et al., 2019). The five simple physics energy models have been derived from energy equations and for each model, a parametric analysis has been performed. The energy and momentum equations utilised in Chapter 3 can be found in Edwards (2003), with the exception of the equations for energy loss to fragmentation and impact.

For each model two travel paths were considered which are shown in Figures 3.1 and 3.2, the travel paths represent common rock avalanche paths noted in the literature (eg. Legros, 2002).

For each simple model, it is assumed that the initial starting height, the mass of the blocks, the orientation of the slopes and the apparent coefficient of friction are known. The models are utilised to calculate the horizontal distance travelled by the rock avalanche except for the impact energy model.

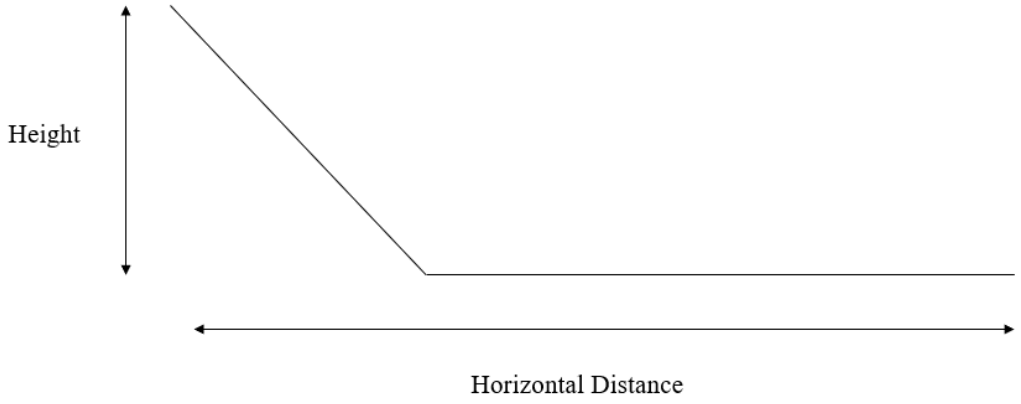

Figure 3.1 The geometry of Path 1. The first travel path considered in the simple physics models, considers two surfaces, one (the upper one) of which is a steep slope and the second (the lower one) is assumed horizontal.

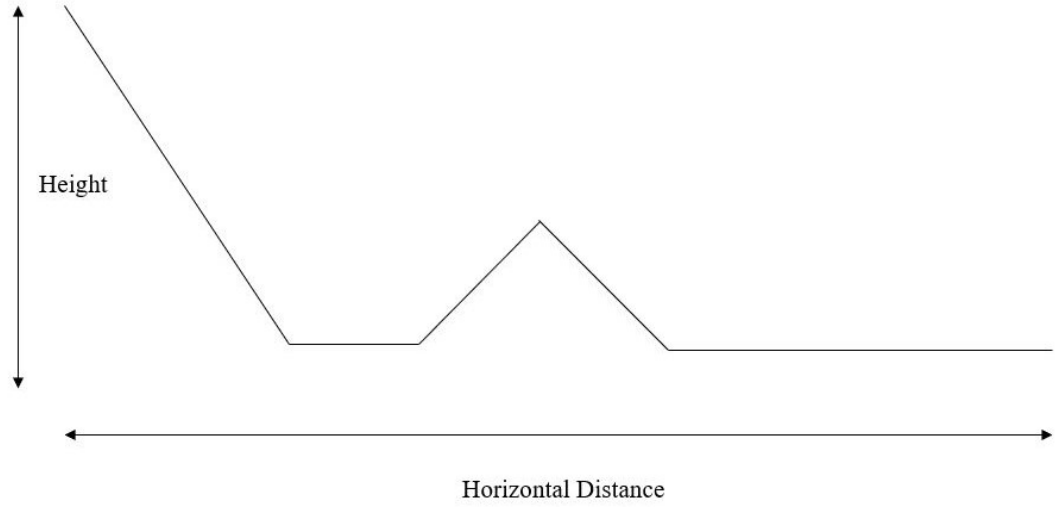

Figure 3.2 The geometry of Path 2. The second travel path analysed in the simple models, includes a second smaller hill to simulated a rock avalanche travelling up and down a neighbouring slope.

3.2 Model 1: Simple Sliding

The first model looks at the results of simple sliding motion in which the rock avalanche mass initially slides along a planar surface as often occurs in rock avalanches in sedimentary rock (e.g. Eisbacher, 1979; Zygouri and Koukouvelas, 2017). The model analyses how changes in height, mass, and the apparent coefficient of friction affect the horizontal distance travelled by a mass.

For the simple sliding energy model, it is assumed that the only energy loss is friction and that the total energy of the system is equal to the potential energy of the mass at Point 1 in Figure 3.3. The model assumes that the rock avalanche can be represented by a simple block that does not deform throughout motion. It is also assumed that there is no energy lost on the transitions between slopes. This model may be used to retroactively determine the horizontal distance travelled by a rock avalanche. Lastly, it is assumed that energy is conserved throughout the model. Figures 3.3 and 3.4 display the two travel paths considered for the simple sliding energy model.

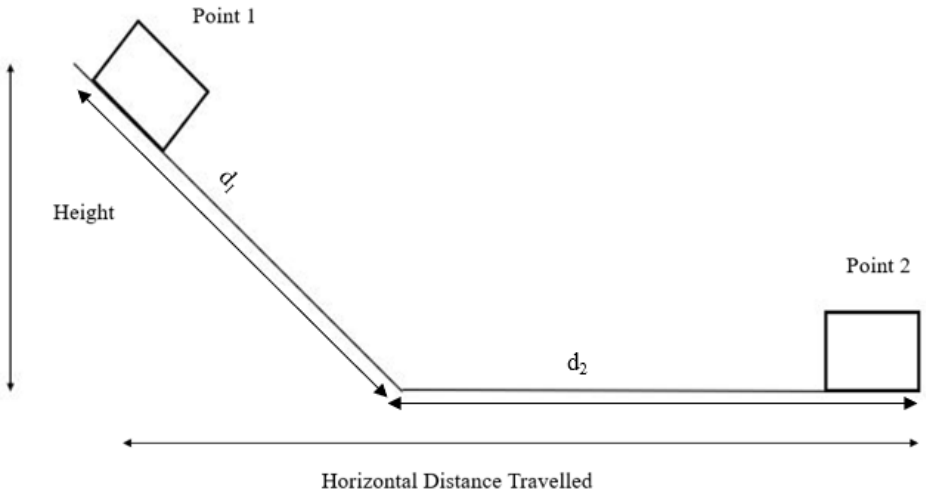

Figure 3.3 The simple sliding model on travel Path 1, Point 1 is the initial moment of failure, the velocity of the failure mass is negligible, therefore the energy at this point is equivalent to the potential energy of the block, Point 2 is the final resting position of the failure mass, all energy has been lost to friction at this point.

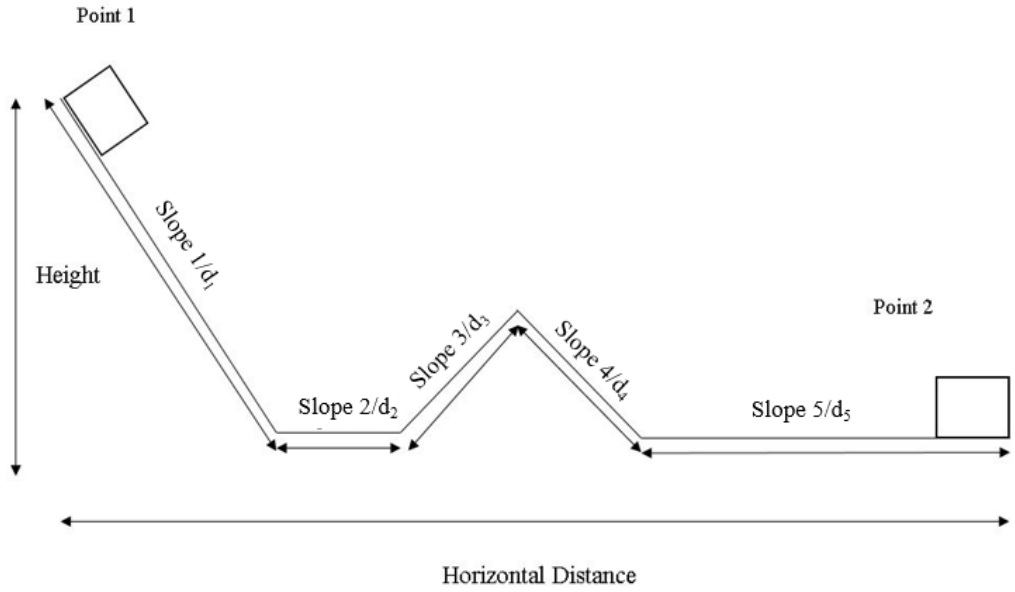

Figure 3.4 The simple sliding model on travel Path 2, Point 1 represents the initial failure of the mass, and Point 2 represents the final resting position of the failure mass, the mass travels over a small hill in this model.

3.2.1 Travel Path 1

The basis of the model is displayed in Figure 3.3, the block starts at rest at Point 1 and starts to move down the initial slope onto the second slope coming to rest at Point 2 at some distance d_2 along the lower slope. Since energy is conserved, it is assumed that the energy at Point 1 is equal to the energy at Point 2:

$$PE = FE \tag{3.1}$$

$$mgh = mgcos\theta\mu d_1 + mg\mu d_2 \tag{3.2}$$

where *PE* is the potential energy of the rock avalanche, *FE* is the energy lost to friction, *m* is the mass, g is gravity θ is the angle of the slope, μ is the apparent coefficient of friction, which is assumed to be Heim's (1932) ratio, d_1 is the distance travelled along the slope and d_2 is the distance travelled along the lower slope.

The total horizontal distance travelled by a rock avalanche is calculated utilizing d_1 and d_2 as shown in equation 3.3:

$$L = d_1 cos\theta + d_2 \tag{3.3}$$

Since d_2 is unknown, equation 3.3 is rearranged to solve for this variable:

$$d_2 = \frac{h - cos\theta\mu d_1}{\mu} \tag{3.4}$$

Equation 3.4 can then be substituted into equation 3.3:

$$L = d_1 cos\theta + \frac{h - cos\theta\mu d_1}{\mu} \tag{3.5}$$

$$L = \frac{h}{\mu} \text{ or } \mu = \frac{h}{L} \tag{3.6}$$

rearranging equation 3.6 gives Heim's Ratio. Heim's Ratio is derived from a simple sliding energy model much like the one considered.

3.2.2 Travel Path 2

The second model for the simple sliding energy model has the addition of two new slopes, the final resting point of the block as shown in Figure 3.4. It is assumed for this model that d_2, d_3, d_4 are known and d_5 is unknown. Again, the energy at Point 1 is equal to the energy at Point 2:

$$mgh = mgcos\theta\mu d_1 + mg\mu d_2 + mgcos\alpha\mu d_3 + mgcos\beta\mu d_4 + mg\mu d_5 \quad (3.7)$$

where α is the angle of the third slope, β is the angle of the fourth slope, d_2 is the distance between the initial slope and hill, d_3 is the distance travelled along the third slope, d_4 is the distance travelled along the fourth slope, and d_5 is the distance travelled along the fifth slope. The horizontal distance is solved for by:

$$L = d_1cos\theta + d_2 + d_3cos\alpha + d_4cos\beta + d_5 \quad (3.8)$$

To solve for the horizontal distance travelled equation 3.8 is solved for d_5 and substituted into equation 3.7:

$$L = \frac{h}{\mu} \text{ or } \mu = \frac{h}{L} \quad (3.9)$$

Rearranging equation 3.9 gives Heim's Ratio. The two different travel path geometries yielded the same final equation when solving for the total horizontal distance travelled, thus it is expected that the travel paths will not affect the horizontal distance when completing the parametric analysis.

3.2.3 Results

A parametric analysis was completed to determine which parameters of the simple sliding energy model would affect the total horizontal runout distance of the rock avalanche mass. The parameters considered are the mass of the block, the initial starting height, the height of the third and fourth slopes in the second travel path, the angle of θ, α and β, the distance to the third and fourth slopes, and the apparent coefficient of friction. The results are displayed in Figures 3.5 to 3.7. Various constants were selected for each value as each parameter is investigated individually, the constant values are listed in Table 3.1.

The constants in Table 3.1 are based on values found in the database in Appendix A and a literature survey. Average values from the database were utilised for the constant parameters for the initial height, the apparent coefficient of friction, and mass. The angle of the initial slope is based on values often found in the literature (eg. Legros, 2002; Geertsema et al., 2006). The height and angles of the second hill of the second travel path model are based on values found in Evans and Delaney (2015). Various height and apparent coefficient of friction values were considered to analyse how this changed the horizontal distance travelled.

Table 3.1 The constants used for the simple sliding parametric analysis, these were obtained from average values of the database provided in Appendix A, the angle of the slope is based on values often found in literature (e.g. Legros, 2002).

Constants

Variable	Value	Unit
Mass	$1.8x10^{12}$	kg
Gravity	9.81	m/s^2
Height 1	1000	m
Height 2	355	m
θ	50	°
α	60	°
β	60	°
μ	0.26	N/A
d_2	250	m

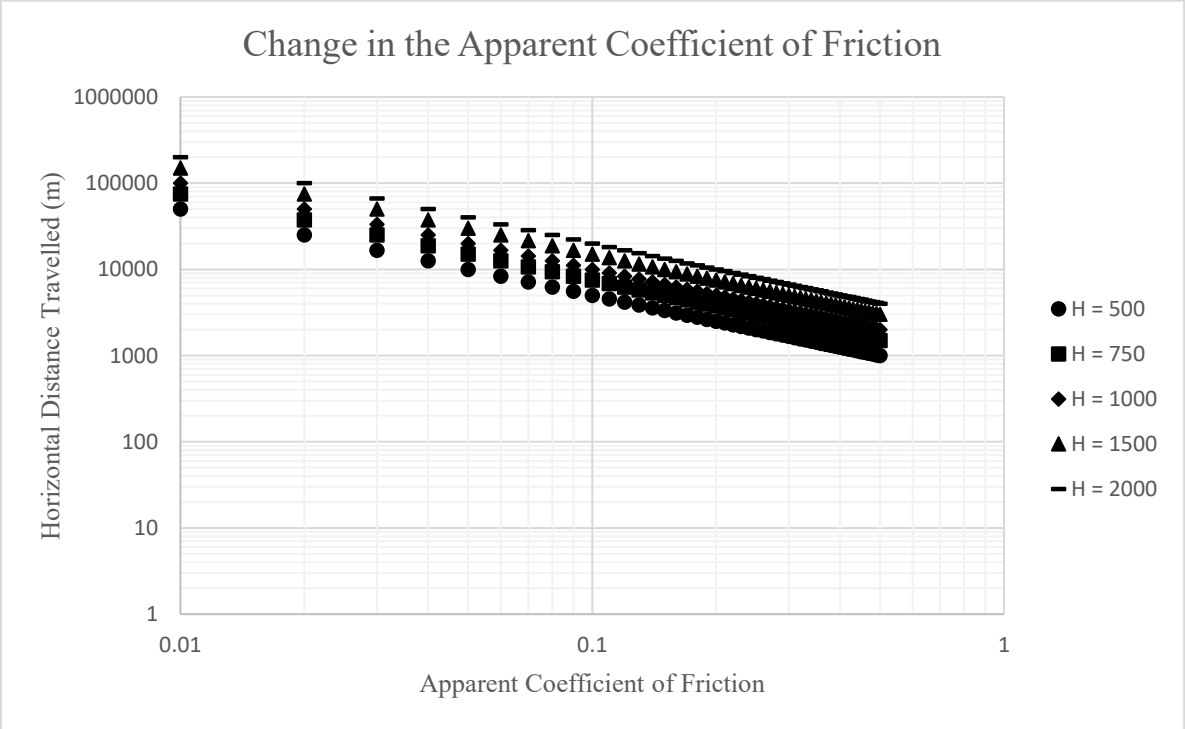

Figure 3.5 Comparison of the apparent coefficient of friction with the change in height and the horizontal distance, as the apparent coefficient of friction value increases, the horizontal distance travelled decreases exponentially.

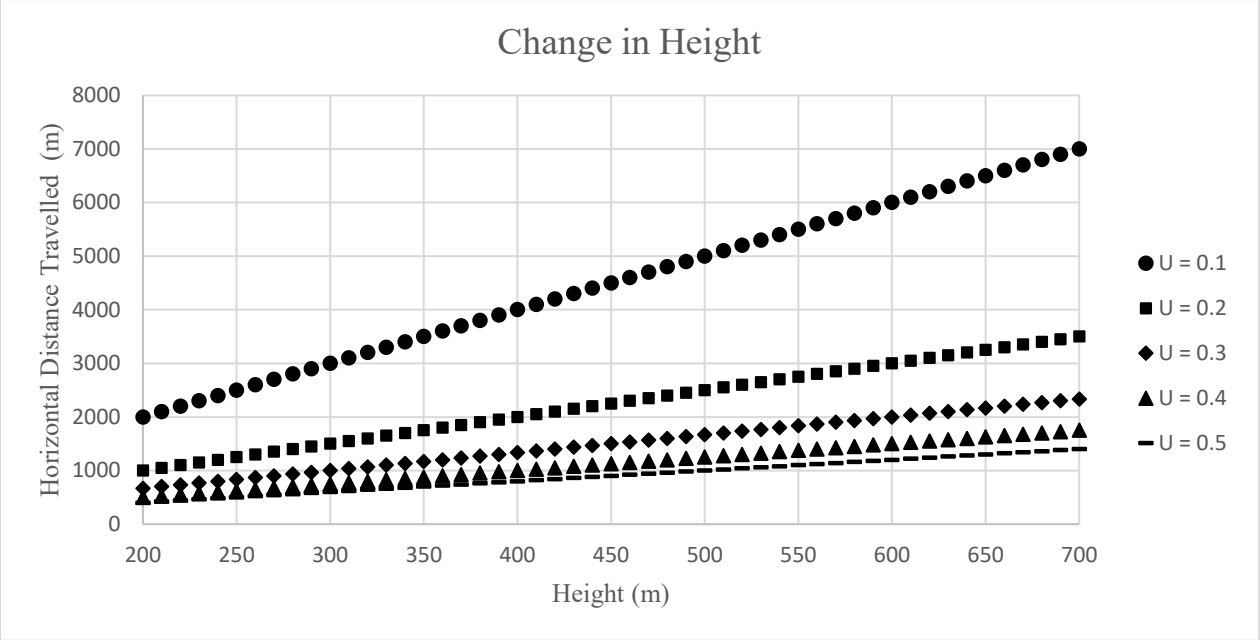

Figure 3.6 Change in height with changing the apparent coefficient of friction values and its effect on horizontal distance for Path 1, as the height increases and apparent coefficient of friction decreases, the horizontal distance travelled also increases.

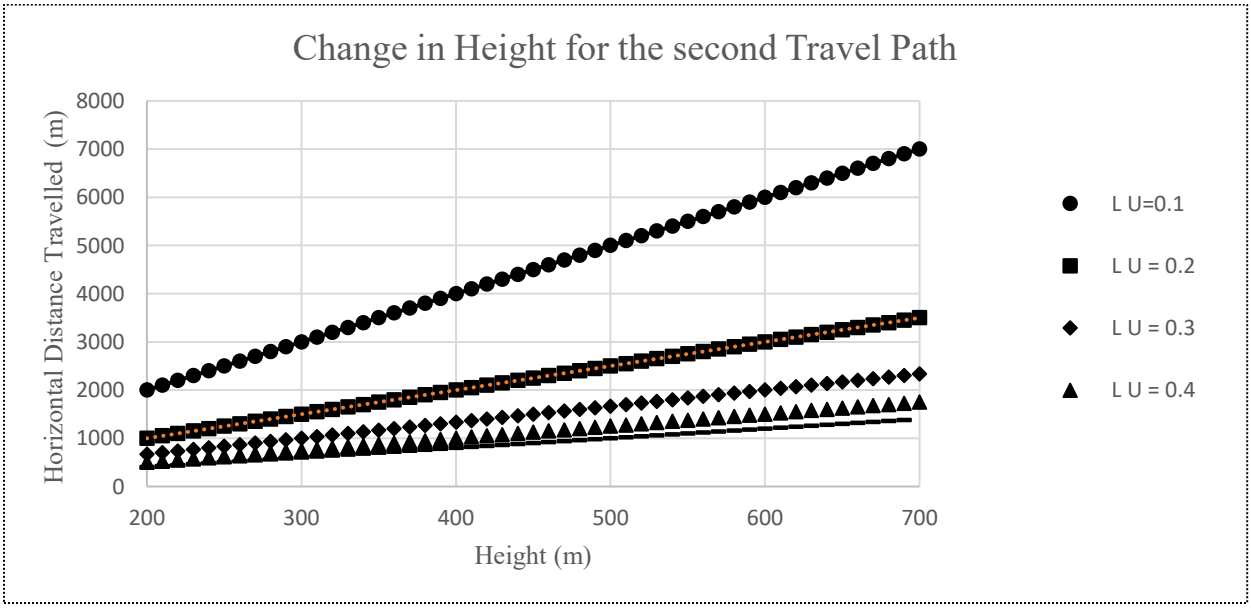

Figure 3.7 Change in height with changing coefficient of friction values and its effect on the horizontal distance for Path 2, this analysis yielded the same results as the one that was completed for Path 1 thus path geometry does not effect the horizontal distance travelled for the sliding model.

3.2.4 Discussion

From equations 3.6 and 3.9, the geometry of the travel paths and their orientation do not affect the horizontal distance travelled by the mass as these parameters are not in the final equation for the simple sliding energy model. Further, the mass does not appear to influence the horizontal distance travelled, i.e., the simple sliding energy model is not mass-dependent. This model does not explain the mass dependency observed in Figure 2.2 from Chapter 2.2.3.

Examining Figures 3.5 to 3.7, both apparent coefficient of friction and the initial height of the mass affect the horizontal distance travelled by the block. From Figure 3.7, a linear relationship exists between the initial height of the mass and the total horizontal distance travelled, in that as the height increases the horizontal distance travelled also increases. The value of the slope between the two parameters is the inverse of the apparent coefficient of friction, which displays that the relationship between height of the mass and the horizonal distance travelled is dependent on the apparent coefficient of friction value.

Various heights were considered to analyse the relationship between the apparent coefficient of friction and the horizontal distance travelled by the mass as shown in Figures 3.5 and 3.7. From Figure 3.5 as the apparent coefficient of friction decreases the horizontal distance travelled increase exponentially. A change in height by 100 m causes a change in the horizontal distance travelled by a magnitude of 10^2 m.

3.3 Model 2: Entrainment

The second model focuses on the entrainment of mass (mass gain) by the rock avalanche. This model is represented by blocks which again are assumed to remain undeformed throughout the event. Typically, when a mass is entrained into a rock avalanche it does not bounce off the mass, it is instead incorporated into the initial mass increasing the volume of the moving mass (Hungr and Evans, 2004; Geertsema et al., 2005; McKinnon et al., 2008, Delaney and Evans, 2014; Farin et al., 2014).

It is assumed that the collision between the initial mass and entrained mass can be represented by an inelastic collision. This energy model considers potential energy, friction energy and energy lost due to the inelastic collision. It is assumed that energy and momentum are conserved in this model.

3.3.1 Travel Path 1

Figure 3.8 gives a representation of the model and various points in time which are utilised to determine the horizontal distance travelled.

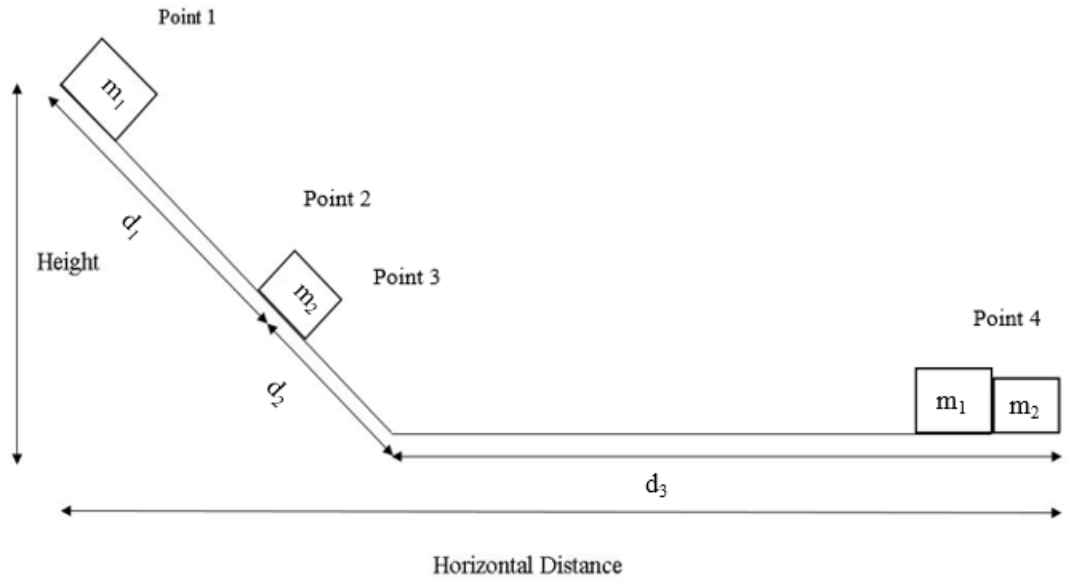

Figure 3.8 Path 1 of the entrainment model, where m_1 is the initial mass, h_1 is the height at which the initial mass is located, m_2 is the entrained mass, h_2 is the height of the entrained mass, and d_1 is the distance travelled before the collision with the second mass.

As energy is conserved, Point 1 can be equated to Point 4:

$$PE = FE + KEl_1 \tag{3.10}$$

where KEl_1 is the kinetic energy lost during the inelastic collision between the masses. Expanding equation 3.10:

$$m_1gh_1 + m_2gh_2 = m_1gcos\theta\mu d_1 + (m_1 + m_2)gcos\theta\mu d_2 + (m_1 + m_2)g\mu d_3 + KEl_1 \tag{3.11}$$

where m_1 is the initial mass, h_1 is the height at which the initial mass is located, m_2 is the entrained mass, h_2 is the height of the entrained mass, d_1 is the distance travelled before the collision with the second mass, d_2 is the distance travelled down the slope after collision with the second mass, and d_3 is the distance travelled along the lower slope.

The kinetic energy lost during the collision between the two masses is determined by using momentum equations for an inelastic collision (Edwards, 2003). It is assumed that the momentum of the block is equal to the momentum of the two blocks after the collision:

$$m_1 V_{1f} = (m_1 + m_2) V_{2i} \tag{3.12}$$

where V_{1f} is the velocity of the initial mass directly before impact and V_{2i} is the velocity of the two masses after impact. V_{1f} is calculated by assuming that Point 1 and Point 2 are equal through energy conservation laws:

$$m_1 g h_1 + m_2 g h_2 = (m_1 + m_2) g h_2 + m_1 g cos\theta \mu d_1 + \frac{1}{2} m_1 V_{1f}^2 \tag{3.13}$$

The kinetic energy lost to the collision is determined by calculating the difference in kinetic energy of the system before and after the collision:

$$\frac{1}{2} m_1 V_{1f}^2 - \frac{1}{2} (m_1 + m_2) V_{2i}^2 = KEl_1 \tag{3.14}$$

Equations 3.12 to 3.14 are repeated for each collision incurred by the mass; thus, the model can account for an infinite amount of non-elastic collisions. The horizontal distance travelled by the two masses is determined by isolating for d_3 from equation 3.15 and substituting into equation 3.11:

$$L = d_1 \cos\theta + d_2 \cos\theta + d_3 \tag{3.15}$$

$$L = \frac{m_1 g h_1 + m_2 g h_2 + m_2 g cos\theta \mu d_1 - KEl_1}{(m_1 + m_2) g \mu} \tag{3.16}$$

3.3.2 Travel Path 2

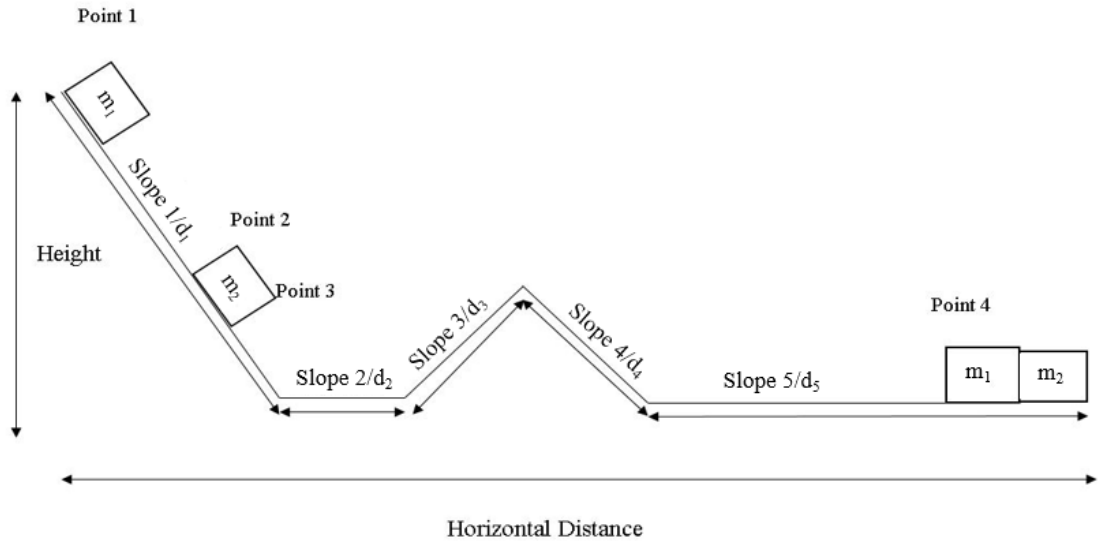

Figure 3.9 Path 2 of the entrainment model, this path includes a hill of which the mass runs over before coming to rest at some distance d_5 along the final slope.

The second model is based on the scenario presented in Figure 3.9, in which the initial mass entrains a second mass on a slope and travels over a hill coming to a rest:

$$m_1gh_1 + m_2gh_2 = m_1gcos\theta\mu d_1 + (m_1 + m_2)gcos\theta\mu d_2 + (m_1 + m_2)g\mu d_3 +$$

$$(m_1 + m_2)gcos\alpha\mu d_4 + (m_1 + m_2)gcos\beta\mu d_5 + (m_1 + m_2)g\mu d_6 + KEl_1 \qquad (3.17)$$

where α is the angle of Slope 3, d_4 is the distance travelled along Slope 3, β is the angle of Slope 4, d_5 is the distance travelled along the fourth slope and d_6 is the distance travelled along Slope 5. Equation 3.18 can be rearranged to isolate for d_6 and substituted back into equation 3.17 to solve for the horizontal distance travelled:

$$L = d_1\cos\theta + d_2\cos\theta + d_3 + d_4cos\alpha + d_5cos\beta + d_6 \qquad (3.18)$$

$$L = \frac{m_1gh_1 + m_2gh_2 + m_2gcos\theta\mu d_1 - KEl_1}{(m_1 + m_2)g\mu} \qquad (3.19)$$

3.3.3 Results

A parametric analysis was completed to determine which parameters of the entrainment energy model affect the horizontal distance travelled by the masses. The parameters considered are the initial mass, the entrained mass, the height of both masses, the apparent coefficient of friction and the path geometry. The values utilised to complete the analysis are listed in Table 3.2. For this analysis, the constant value for the second mass was assumed to be 30% of the initial mass (e.g., Bessette-Kirton et al., 2018).

Table 3.2 The constants considered for the parametric analysis of the entrainment model, the average values where used from Appendix A for the constants considered, and the second mass was considered to be 30% of the initial mass as determined by Bessette-Kirton et al. (2018).

Constants		
Variable	**Value**	**Unit**
Mass 1	1.8×10^{12}	kg
Mass 2	0.54×10^{12}	kg
Gravity	9.81	m/s^2
Height 1	1000	m
Height 2	250	m
Height 3	355	m
θ	50	°
α	60	°
β	60	°
μ	0.26	N/a

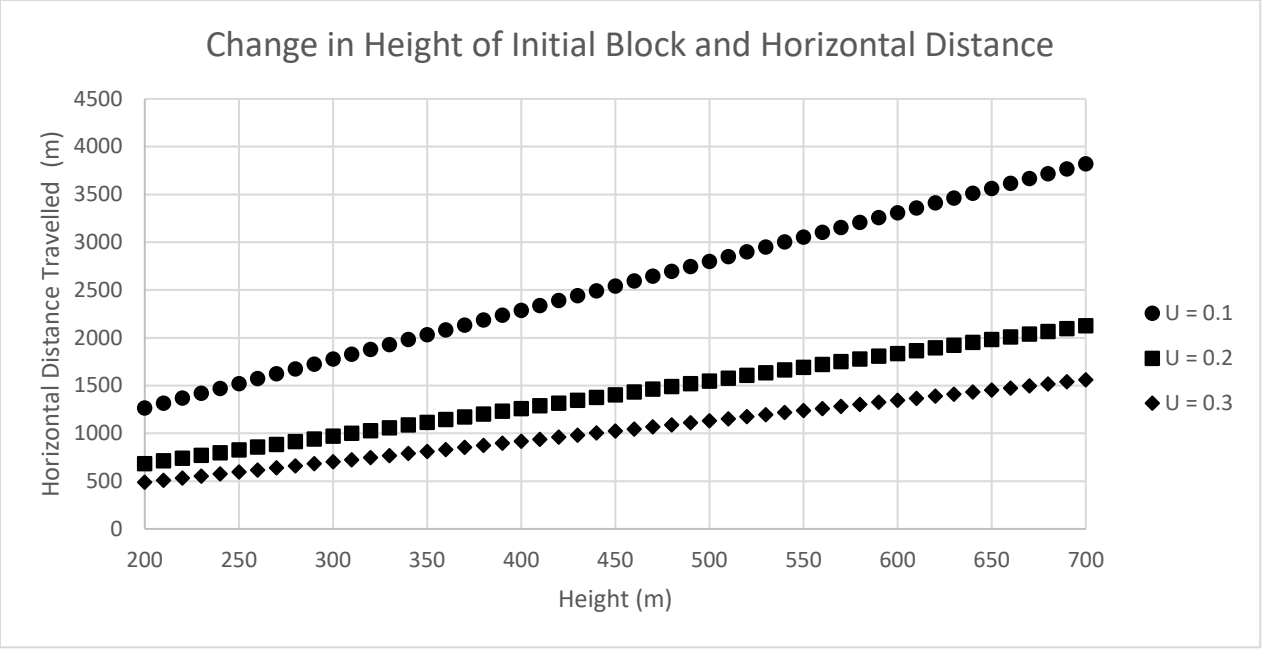

Figure 3.10 The analysis of how a change in height of the initial block, and a change in the apparent coefficient of friction value affects the horizontal distance travelled, as the height increases and the apparent coefficient of friction value decreases, the distance traveled increases.

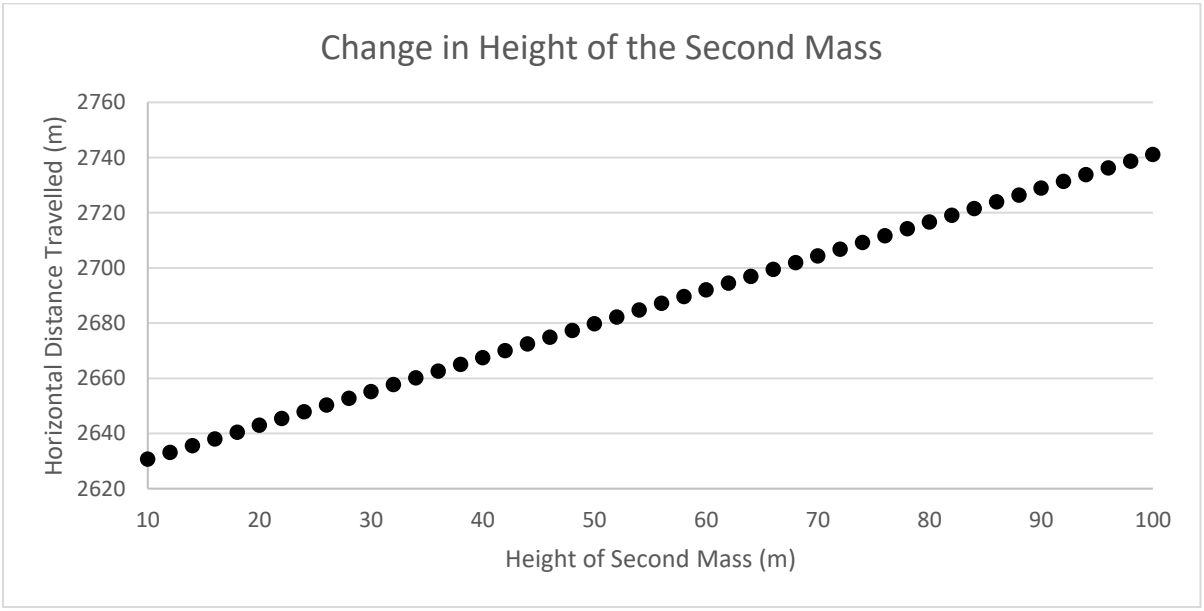

Figure 3.11 The analysis of the change in height of the second mass, as the height of the second mass increases the horizontal distance travelled also increases as increasing the height of the second mass increases the potential energy available to the system.

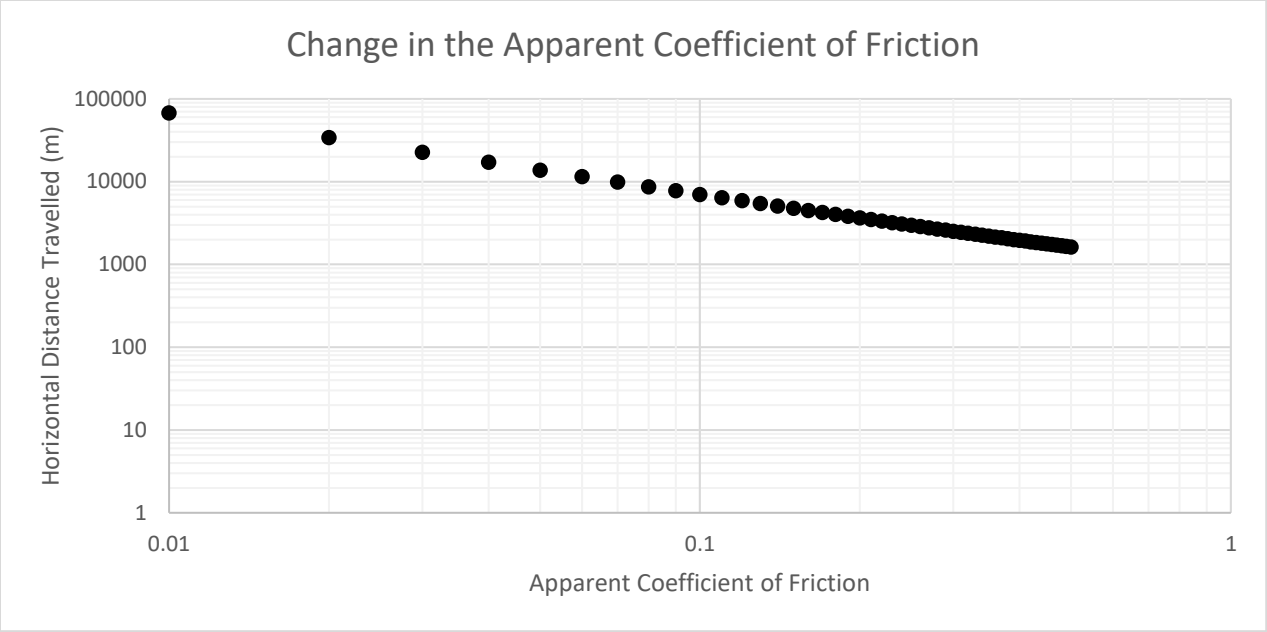

Figure 3.12 The analysis of the change in the apparent coefficient of friction value, as the apparent coefficient of friction increases, the horizontal distance travelled decreases exponentially.

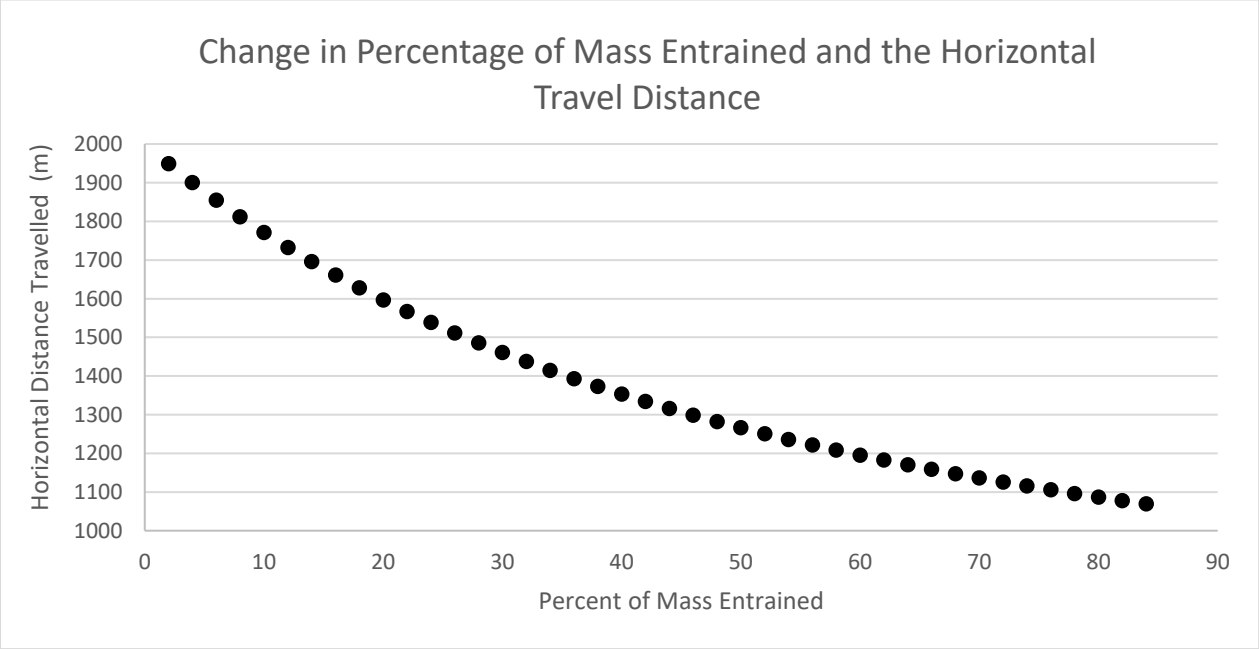

Figure 3.13 As the percentage of mass entrained is increased the horizontal distance travelled decreases as more energy is lost to the inelastic collision between the initial and entrained mass, this is an unexpected behaviour highlighted by the entrainment model.

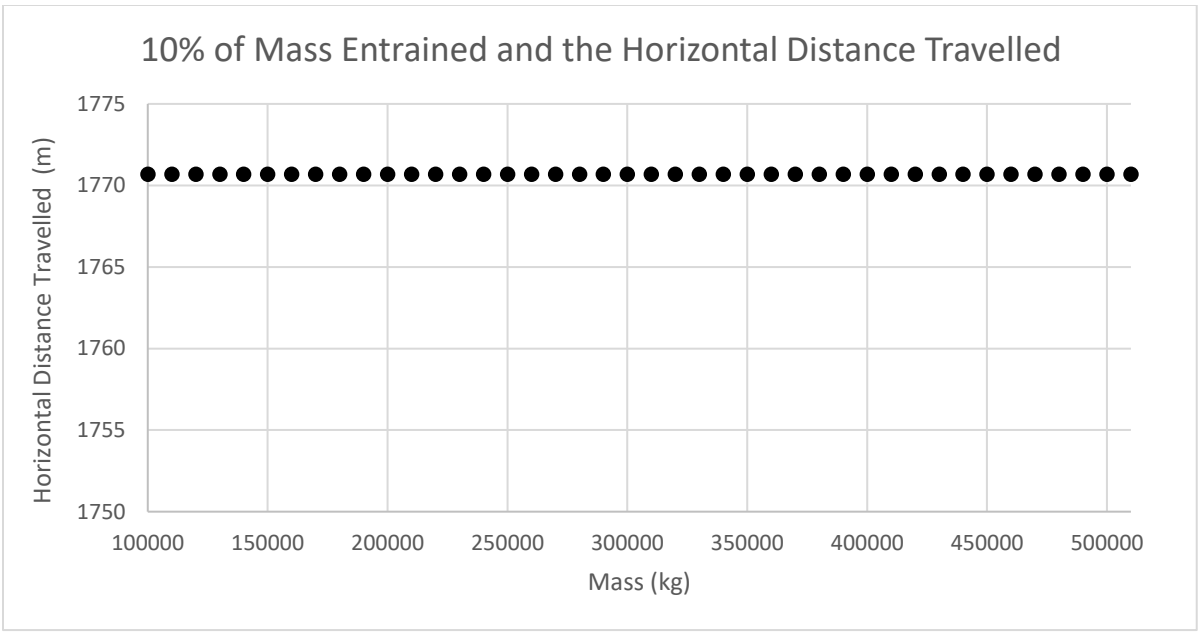

Figure 3.14 The entrained mass was kept constant at 10% of the initial mass, which was increased to determine role of which mass had on the horizontal distance travelled, the increase in the initial mass did not affect the horizontal distance travelled when the entrained mass was kept at a constant percentage of the initial mass.

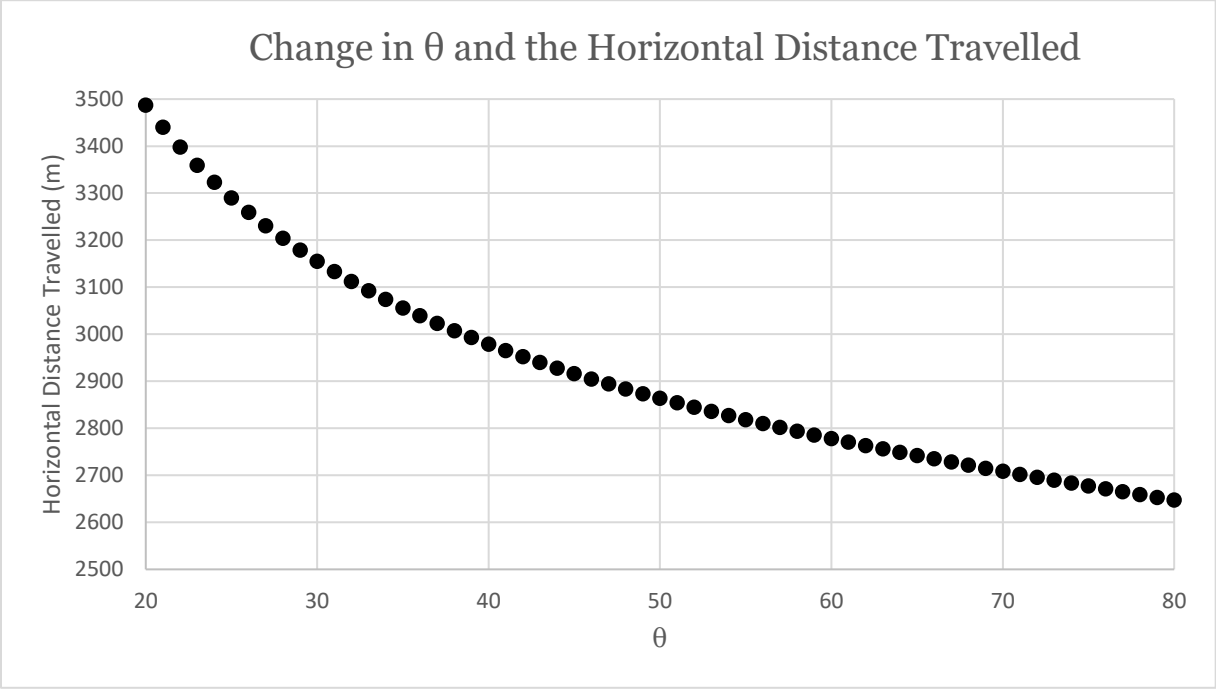

Figure 3.15 For the entrainment model, the mass was shown to be entrained on the Slope 1 and changing the angle of the Slope 1 would change the distance between the two masses and thus would change the horizontal distance travelled, as shown, as the angle of the Slope increased, the distance travelled decreased.

3.3.4 Discussion

The results of the parametric analysis are displayed in Figures 3.10 to 3.15. The change in the angles of slopes 3 and 4 and the distance between the initial slope and the hill does not appear to affect the horizontal distance travelled. The change in the angle of the initial slope does affect the horizontal distance travelled as shown in Figure 3.15, as the angle of the slope increases the horizontal distance travelled decreases. The increase in the angle of the initial slope induces a decrease in the distance between the two masses; after the collision between the two masses, the energy lost to friction increases at a greater rate as energy lost to friction is mass-dependent.

An important feature of this model is that it does not appear to depend on the initial mass; rather, the percentage of mass entrained with respect to the initial mass dictates the horizontal distance travelled. From Figure 3.13, as the percentage of the mass entrained increases with respect to the initial mass the horizontal distance travels decreases. Increasing the percentage of mass entrained increases the energy lost to the inelastic collision between the two masses limiting the energy available in the system. Further, if the initial mass changes and the percentage of mass entrained is kept constant at 10% of the initial mass the horizontal distance travelled does not change as observed in Figure 3.14.

It can also be concluded that a change in height in either block has a direct effect on the horizontal distance travelled. As shown in Figures 3.10 and 3.11 increasing the height of both blocks increased the horizontal distance travelled. An increase in the height of the initial mass increases the potential and total energy of the system.

As observed from Figure 3.12, as the apparent coefficient of friction increases the horizontal distance decreases exponentially. The relationship exhibits the same behaviours discussed in Section 3.3.4.

3.4 Model 3: Deposition

The depositional energy model examines the process of mass loss during a rock avalanche and considers the momentum equations as the entrainment model. This process is shown in Figures 3.16 and 3.17 and is represented as two blocks sliding down a slope where one block stops at some distance while the other block continues until coming to rest. As with the entrainment model, this model assumes that both energy and momentum are conserved, and the only energy losses are to friction and kinetic energy when mass is lost.

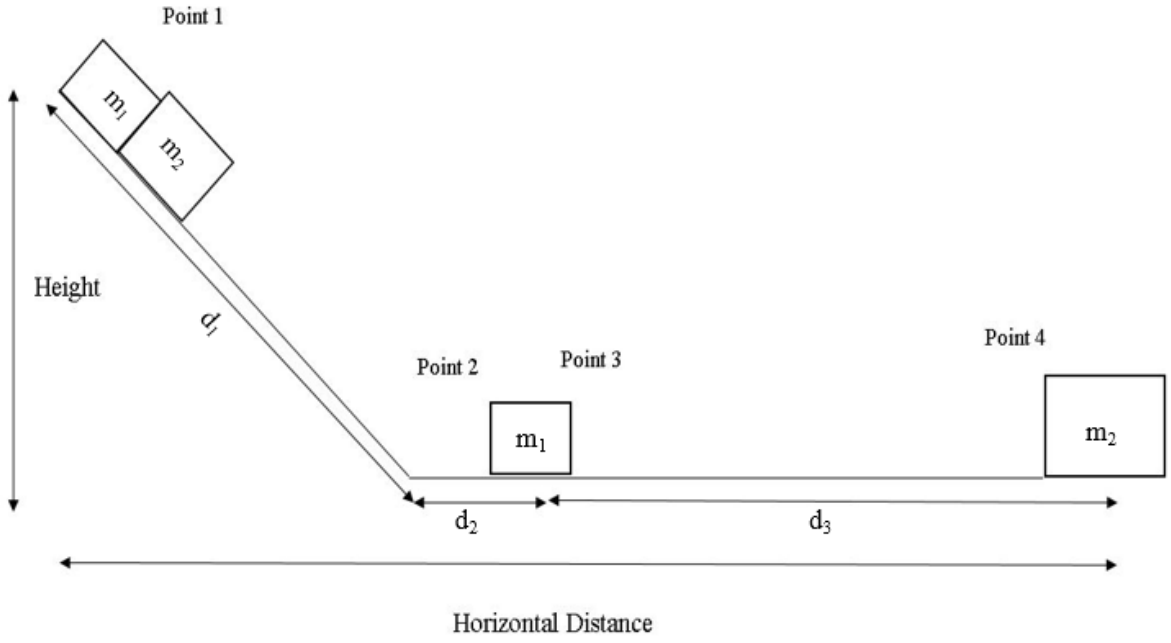

Figure 3.16 Path 1 for the depositional model, where d_1 and d_2 are the distance travelled by both m_1 and m_2, and Point 2 represents the moment directly before m_1 is deposited.

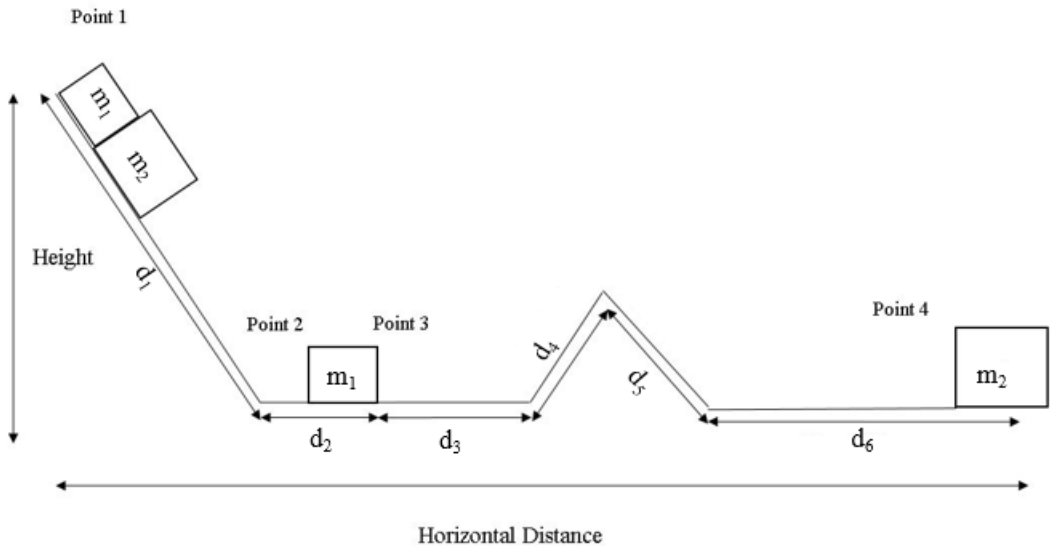

Figure 3.17 Path 2 for the depositional model, some of the failure mass is lost before the main body of the rock avalanche travels up and over a small hill .

3.4.1 Travel Path 1

The first model is based on Figure 3.16, where the two blocks start at Point 1 as a single mass and transition onto the lower slope where m_1 is deposited and m_2 continues to Point 4. Since energy is conserved, the energy at Point 1 can be equated to the energy at Point 4:

$$(m_1 + m_2)gh = (m_1 + m_2)gcos\theta\mu d_1 + (m_1 + m_2)g\mu d_2 + m_2 g\mu d_3 + KEl_1 \qquad (3.19)$$

The KEl_1 is determined utilizing conservation of momentum, the momentum before deposition will equal the momentum after deposition:

$$(m_1 + m_2)V_1 = m_1 V_{2a} + m_2 V_{2b} \qquad (3.20)$$

where V_1 is the velocity directly before the mass lost, V_{2a} is the velocity of the mass deposited (which is assumed to be 0), and V_{2b} is the velocity of the mass which continues to travel after deposition. This equation is rearranged to solve for V_{2b}:

$$V_{2b} = \frac{(m_1+m_2)V_1}{m_2} \tag{3.21}$$

The energy loss to the collision is determined by comparing the change in kinetic energy before and after the loss of mass:

$$KEl_1 = \frac{1}{2}(m_1 + m_2)V_{1f}^2 - \frac{1}{2}m_2V_{2i}^2 \tag{3.22}$$

The horizontal distance travelled is determined by isolation for d_3 in equation 3.23 and substituting into equation 3.19:

$$L = d_1cos\theta + d_2 + d_3 \tag{3.23}$$

$$L = \frac{(m_1+m_2)gh - m_1gcos\theta\mu d_1 - m_1g\mu d_2 - KEl_1}{m_2g\mu} \tag{3.24}$$

3.4.2 Travel Path 2

The next model is based on Figure 3.17. From the conservation of energy laws, it can be assumed that Point 1 is equal to Point 4:

$$(m_1 + m_2)gh = (m_1 + m_2)gcos\theta\mu d_1 + (m_1 + m_2)g\mu d_2 + m_2g\mu d_3 + m_2gcos\alpha\mu d_4 + m_2gcos\beta\mu d_5 + m_2g\mu d_6 + KEl_1 \tag{3.25}$$

The calculation of KEl_1 has been shown in equation 3.22. The horizontal distance is calculated by isolation for d_6 and substituting equation 3.26 into 3.27:

$$L = d_1cos\theta + d_2 + d_3 + d_4cos\alpha + d_5cos\beta + d_6 \tag{3.26}$$

$$L = \frac{(m_1+m_2)gh - m_1gcos\theta\mu d_1 - m_1g\mu d_2 - KEl_1}{m_2g\mu} \tag{3.27}$$

3.4.3 Results

The parametric analysis considered the following parameters: the deposited mass, the final mass, the initial height, the angle of the first, the apparent coefficient of friction and the percentage of mass deposited with respect to the initial mass. The angle of the third and fourth slopes and the distance to the second hill were not considered for the parametric analysis as these parameters were not found to affect the horizontal distance travelled by a rock avalanche for the entrainment energy model. Table 3.3 displays the constant parameters used for the parametric analysis. The depositional behaviour observed in rock avalanches is not as well studied as other behaviours, therefore it is assumed that the deposited mass is 30% of the initial mass. The results are displayed in Figures 3.18 to 3.24.

Table 3.3 The constants for the parametric analysis for the depositional model were obtained by taking the average value of the variables from Appendix A, and it was assumed that the deposited mass is 30% of the initial mass.

Constants		
Variable	**Value**	**Unit**
Mass 1	1.8×10^{12}	kg
Mass 2	0.54×10^{12}	kg
Gravity	9.81	m/s^2
Height 1	1000	m
Height 2	355	m
θ	50	°
α	60	°
β	60	°
μ	0.26	N/A

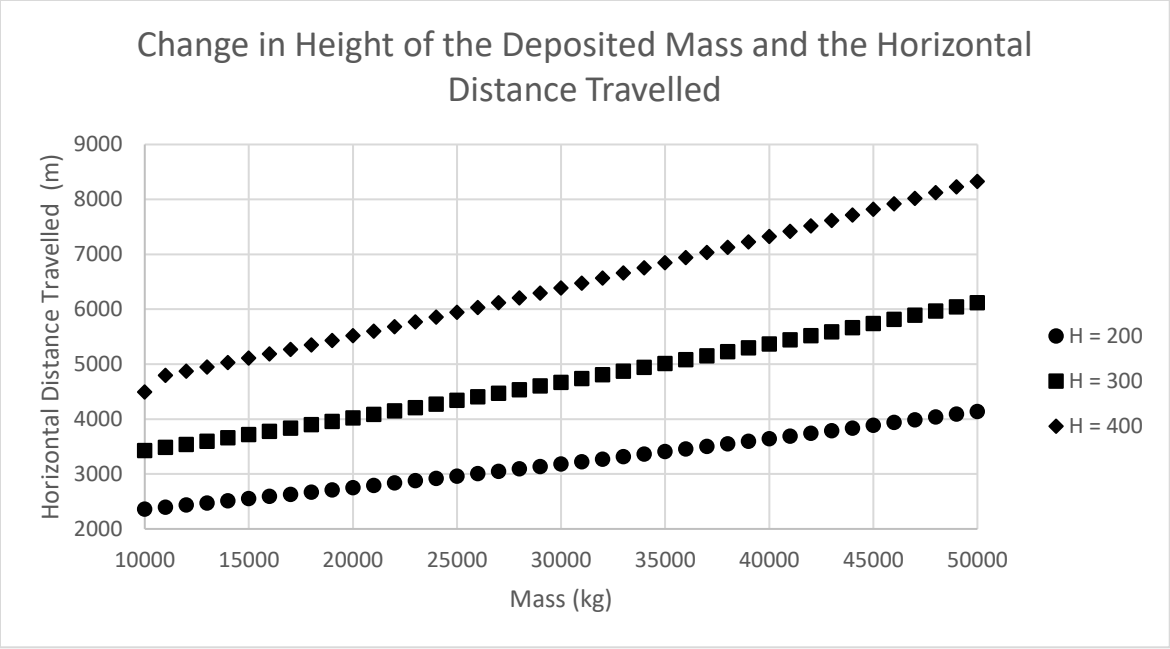

Figure 3.18 As both the height of the deposited mass and the amount of mass deposited increases the horizontal distance travelled also increases, a smaller mass does not loose energy as quickly to friction as a larger mass, thus the sooner the mass is deposited the quicker the rate lost to friction decreases.

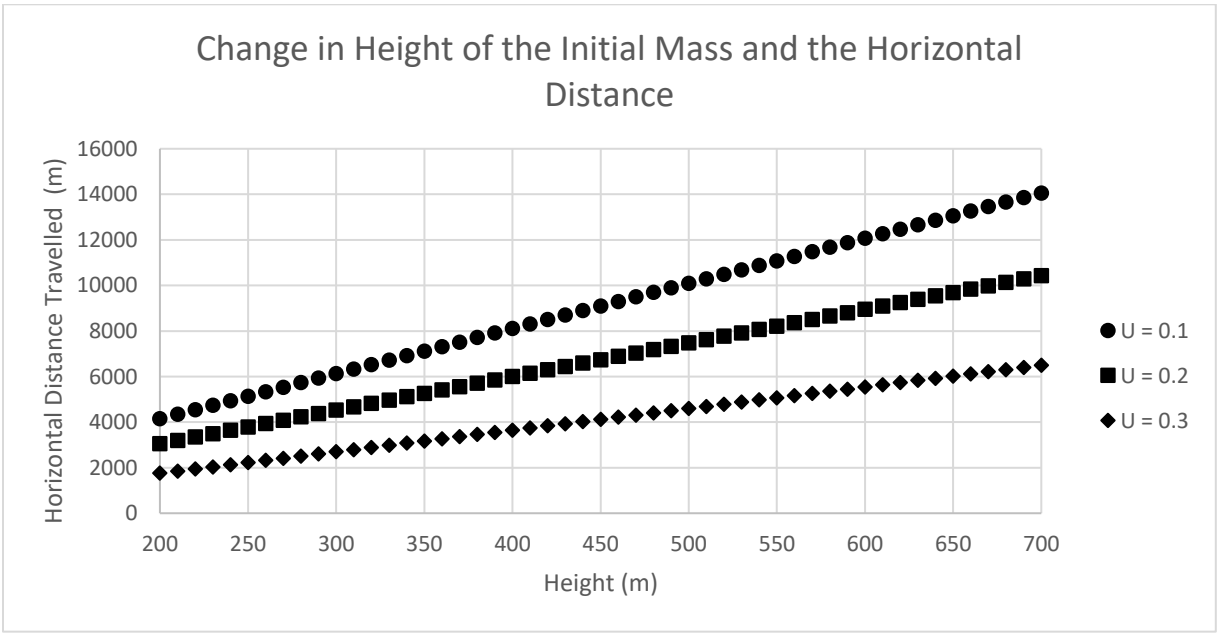

Figure 3.19 As the height of the initial mass increased and the apparent coefficient of friction decreased the horizontal distance travelled increased, which is in line with results from the previous two models, increasing the height of the initial mass increases the potential energy and total energy of the system.

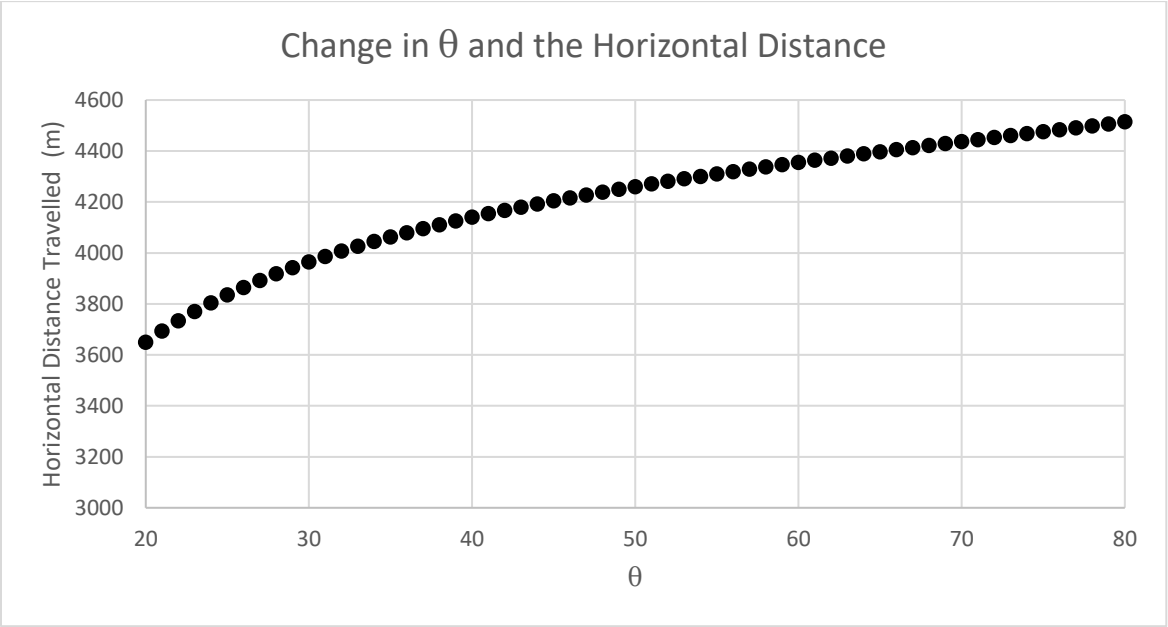

Figure 3.20 Like the entrainment model, the depositional model considers that mass is lost on Slope 1, an increase in the angle of Slope 1 increased the horizontal distance travelled, increasing the angle of Slope 1 decreases the distance between initial starting point of the model and the position at which mass is lost.

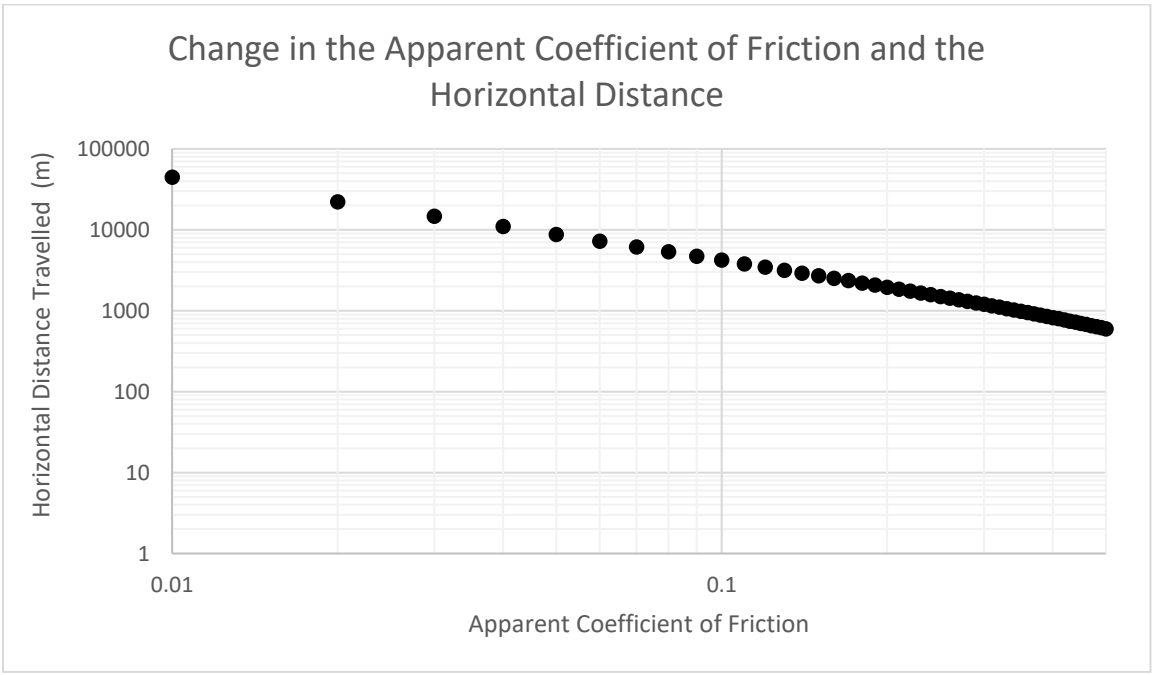

Figure 3.21 As the coefficient of friction increases, the horizontal distance travelled decreases exponentially which is consistent with the results from the previous models.

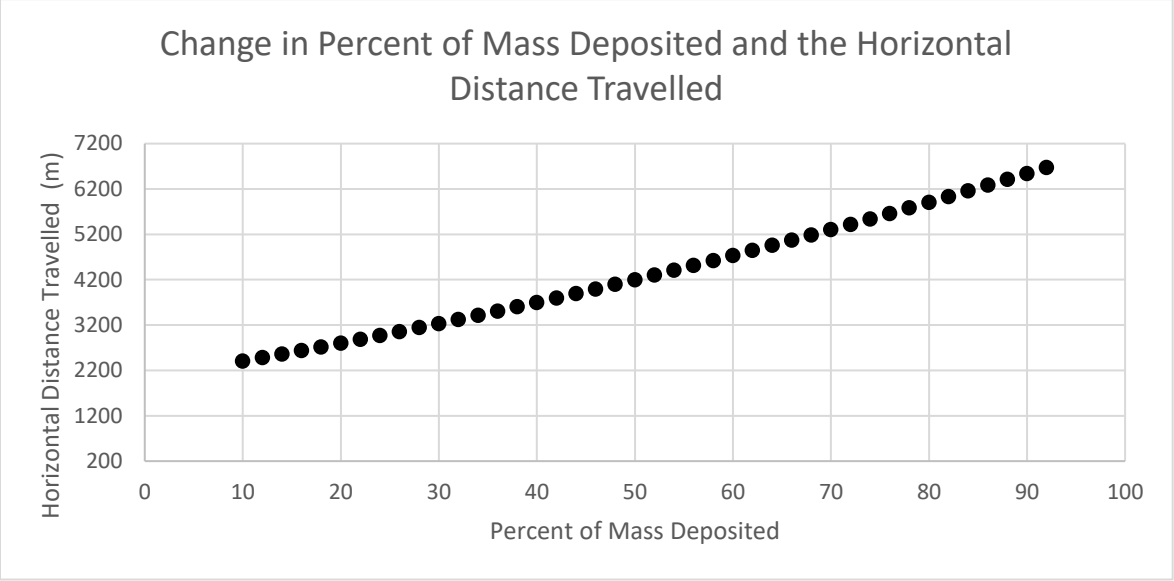

Figure 3.22 As the percentage of mass deposited increased with respect to the initial mass, the horizontal distance travelled increased, as more mass is lost with respect to the initial the rate at which energy is lost to friction will decrease, as friction is a mass dependent term in this model. The lower final mass will not loose energy as quickly to friction as the initial mass of the model.

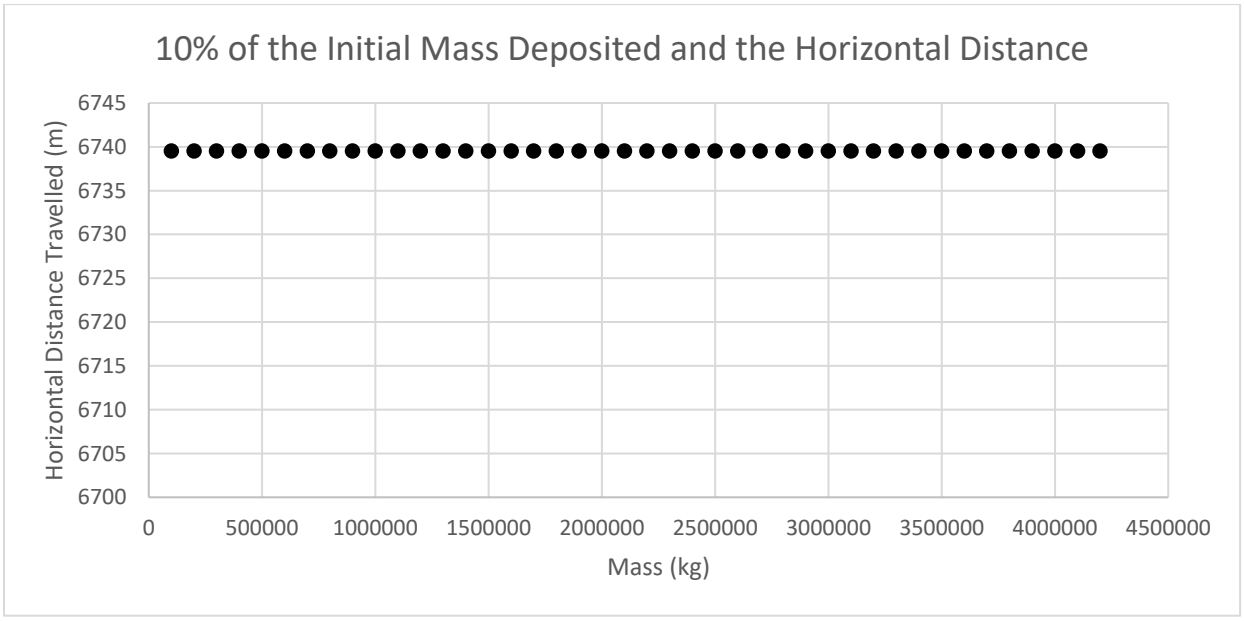

Figure 3.23 If the percent of mass lost is kept constant with respect to the initial mass, and the initial mass is increased, there will be no effect on the horizontal distance travelled by the rock avalanche. The system is not dependent on the initial mass but rather the percentage of mass lost with respect to the initial mass.

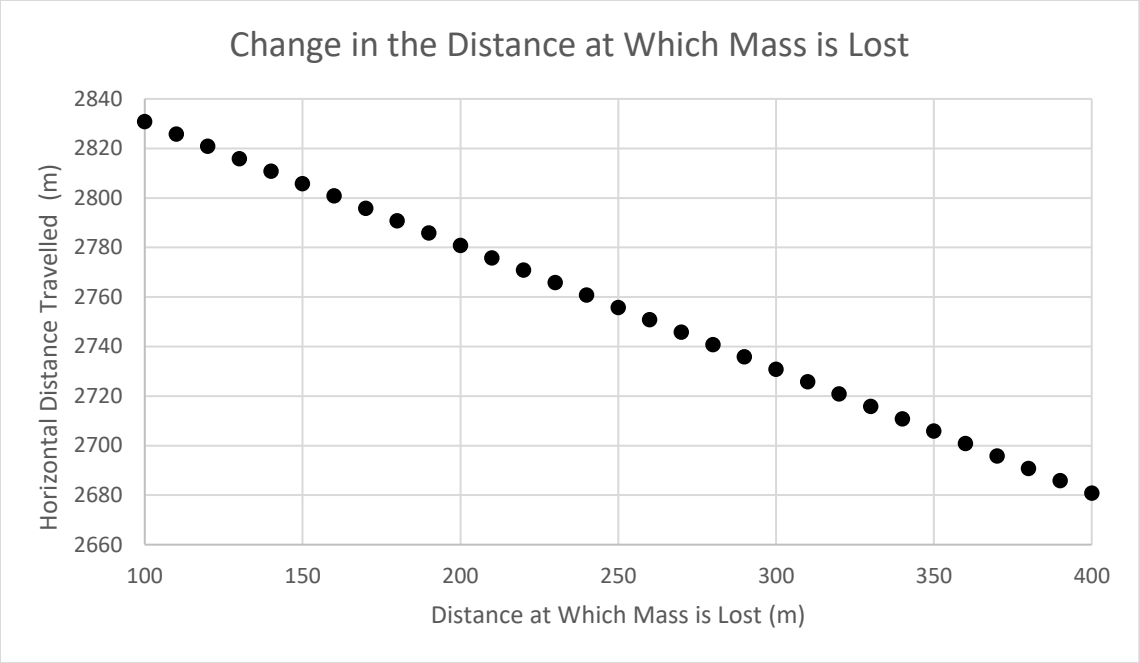

Figure 3.24 As the distance at which the mass lost is increased with respect to the initial position, the horizontal distance travelled decreases. This is likely due to the rate at which energy is lost to friction, the longer the mass stays together the rate at which energy is lost to friction increases, and more energy is lost to this process before the mass splits apart.

3.4.4 Discussion

Figure 3.20 shows that the change in the angle of the initial slope influenced the horizontal distance travelled by the event, as the slope increases the horizontal distance travelled also increased. An increase in the angle of the initial slope decreases the distance travelled by the combined mass, decreasing the rate at which energy is lost to friction.

Further, as displayed in Figure 3.24, as the distance the combined masses travels together increased the horizontal distance travelled decreased. As the distance of the deposition increases the horizontal distance decreases due to energy loss to friction. The rate at which energy is lost to friction increases with increasing mass. Thus, the increased distance the two masses travelled together would cause the rate of energy lost to friction to be greater.

As shown in Figure 3.19 the height of the first slope is increased the horizontal distance increases, which is consistent with the results of the first two models. From Figure 3.21 as the apparent coefficient of friction is increased the horizontal distance travelled decreases, these findings are consistent with the results from the first two models. Similar to the first model, the slope of the height and horizontal distance travelled is the inverse of the apparent coefficient of friction.

It was observed in Figure 3.22 that if the percentage of mass deposited increased with respect to the initial mass, the horizontal distance travelled would also increase. Increasing the percentage of mass lost with respect to the initial mass allows for the rate of energy lost to friction to decrease after deposition. This would allow for the final mass to travel farther than the initial mass. Further, it was found that if the initial mass was increased and the percentage of mass deposited was kept at 10% of the initial mass, the horizontal distance travelled would not change as shown in Figure 3.23 reflecting the independence of runout distance on initial mass. Similar behaviour was noted for the entrainment energy model. It can be concluded that the entrainment and depositional energy models are not directly mass-dependent, rather they appear to be dependent on the mass gained or lost with respect to the initial mass during motion.

There are very limited examples in which all of the values are known for deposition and further research is required to determine the accuracy of the model.

3.5 Model 4: Fragmentation

The fragmentation energy model is a combination of the simple sliding energy model and the fragmentation model from Locat et al. (2006). Locat et al. (2006)'s fragmentation model utilised blasting equations which have been derived to quantify rock avalanche fragmentation.

It was assumed that the block which represents the mass remains undeformed throughout the entirety of the event. The block represents the mass and does not necessarily represent the final shape of the rock avalanche deposit, rather the furthest extent to which a rock avalanche could travel as discussed in Section 3.1. It is assumed that the only energy losses are friction and fragmentation. Since the fragmentation energy model combines both the simple sliding energy model and the Locat et al. (2006) fragmentation equations, the first travel path was considered as it was shown in the simple sliding energy model that the travel path does not affect the horizontal distance travelled.

3.5.1 Travel Path 1

The fragmentation model was derived from potential energy, energy lost to friction and energy lost to fragmentation. It is based on Figure 3.3 from the simple sliding model:

$$mgh = mgcos\theta\mu d_1 + mg\mu d_2 + EFrag \tag{3.28}$$

where $EFrag$ is the energy lost to fragmentation from Locat et al. (2006):

$$Efrag = 3600wb\forall\rho \tag{3.29}$$

where wb is the work needed to blast material (Locat et al., 2006), $\forall$ is the volume and ρ is the density of the rock avalanche mass. The work needed to blast the material can be calculated by:

$$wb = \sqrt{k\frac{S_b}{S_a}} \tag{3.30}$$

where k is a blast constant, S_b is the size of the blocks before fragmentation, and S_a is the size of the blocks after fragmentation, the average grain size (D_{50} and d_{50}, respectively) is used for the

S_b and S_a values (Locat et al., 2006). The k value is a blasting constant that is 0.092 for limestone, 0.112 for granite and 0.128 for basalt (Locat et al., 2006).

The fragmentation energy is first calculated before determining the distance of which the block has travelled. The horizontal distance travelled is determined by utilizing equation 3.31 to solve for d_2 and substituting into equation 3.28:

$$L = d_1 cos\theta + d_2 \tag{3.31}$$

$$L = \frac{gh - 3600wb}{g\mu} \tag{3.32}$$

3.5.2 Results

The parametric analysis completed for the fragmentation energy model considered only the parameters utilised to calculate the energy lost to fragmentation. The parametric analysis for the simple sliding energy model can be found in Section 3.2.3. The parametric analysis explored the relationship between the horizontal distance and S_a, S_b, and the mass. The results are displayed in Figures 3.25 and 3.26. The parameters used for the parametric analysis are listed in Table 3.4. An average value was utilised for both the D_{50} and d_{50} values in the parametric analysis, and it was assumed that k was equivalent to the value for limestone as five of the eight events considered in Locat et al. (2006) occurred in limestone.

Table 3.4 The constants utilised in the parametric analysis for the fragmentation energy model were obtained from average values from Appendix A, and from Locat et al. (2006).

Constants		
Variable	**Value**	**Unit**
Mass	$1.8x10^{12}$	kg
Gravity	9.81	m/s^2
Height	1000	m
D_{50}	2.25	m
d_{50}	0.25	m
k	0.092	N/A
θ	50	°

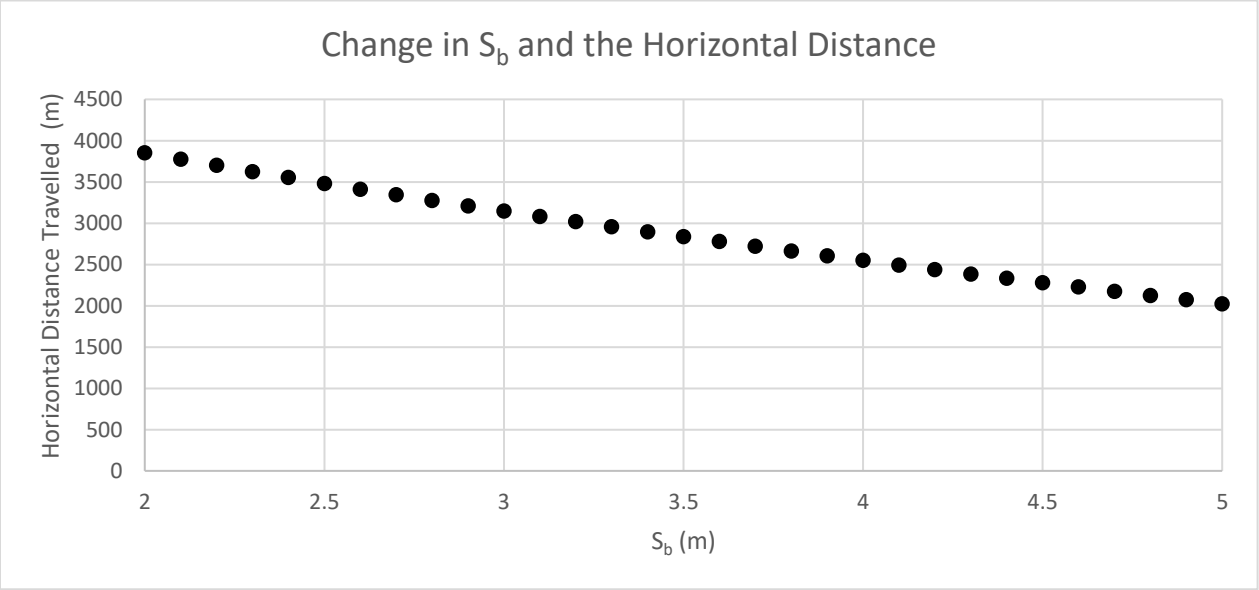

Figure 3.25 As the initial grain size, S_b (D_{50}) is increased and the final grain size is kept constant, the horizontal distance travelled decreased as more energy is required to break the initial large grain size down to the final grain size. The increase in energy spent in fragmentation leaves less energy available to the system for the other processes which occur thus limiting the horizontal distance travelled.

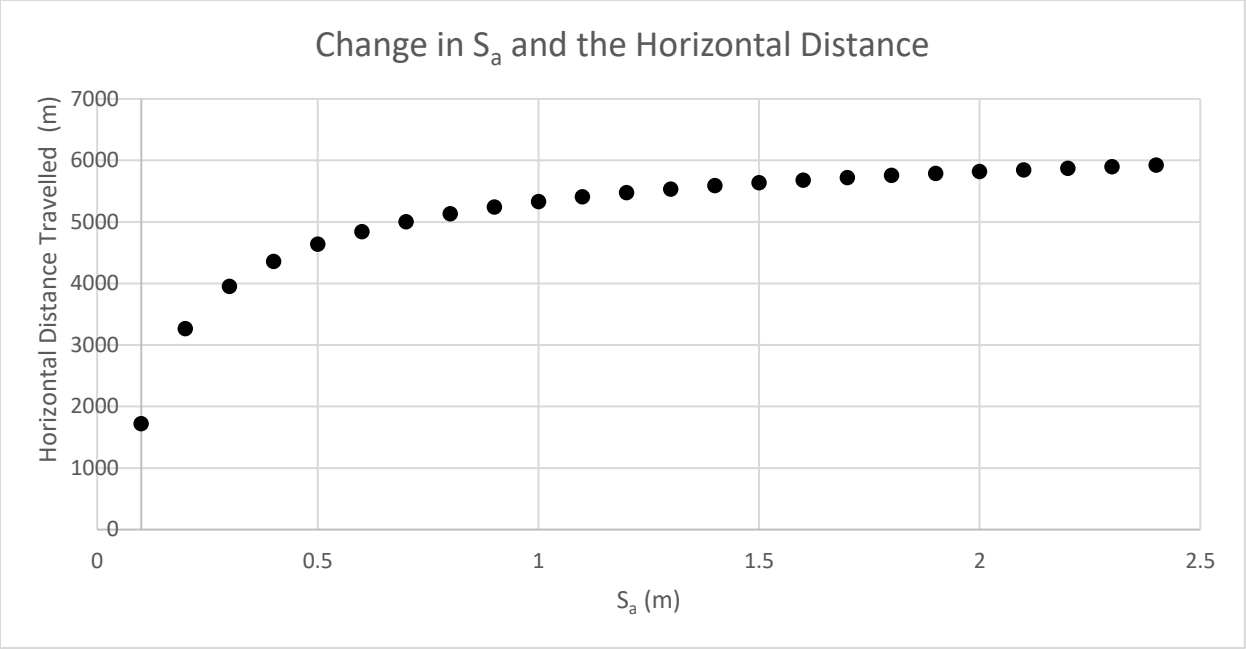

Figure 3.26 As the final grain size, S_a (d_{50}) is increased, and the initial grain size is kept constant, the horizontal distance travelled increased. Increasing S_a decreases the difference in size between the initial and final grain size, thus less energy would be lost to fragmentation, leaving more energy available to the system.

3.5.3 Discussion

From Figure 3.25, as the grain size of the initial mass increases, S_b, the horizontal distance travelled decreases. The increase in initial grain size while keeping the final grain size constant increases the energy required to break the initial block. From Figure 3.26, as the final grain size increases so does the horizontal distance travelled as less energy is lost to fragmentation. Since the initial grain size is kept constant the gap in size between the two values decreases thus less energy is lost to fragmentation. Fragmentation energy appears to be dictated by the amount of change between the initial and final grain size, which is consistent with findings in current literature (e.g., Dunning, 2006; Locat et al., 2006; Crosta et al., 2007; Haug et al., 2016; Zhao et al., 2017).

As per equation 3.32, this model is not mass-dependent and a change in mass will not affect the horizontal distance travelled for this model.

3.6 Model 5: Impact

3.6.1 Impact Energy Model Path

The impact energy model examines energy loss to the initial impact of a failure mass along a lower stiff slope after falling away from the failure surface. The impact energy model is in the preliminary stages and requires further research to better understand how it would affect the horizontal distance travelled by a rock avalanche. Few models explore the energy lost to initial impact and its relationship with the horizontal distance. This process could potentially be a significant source of energy loss and may be the cause for the large degree of fragmentation observed in some rock avalanche deposits.

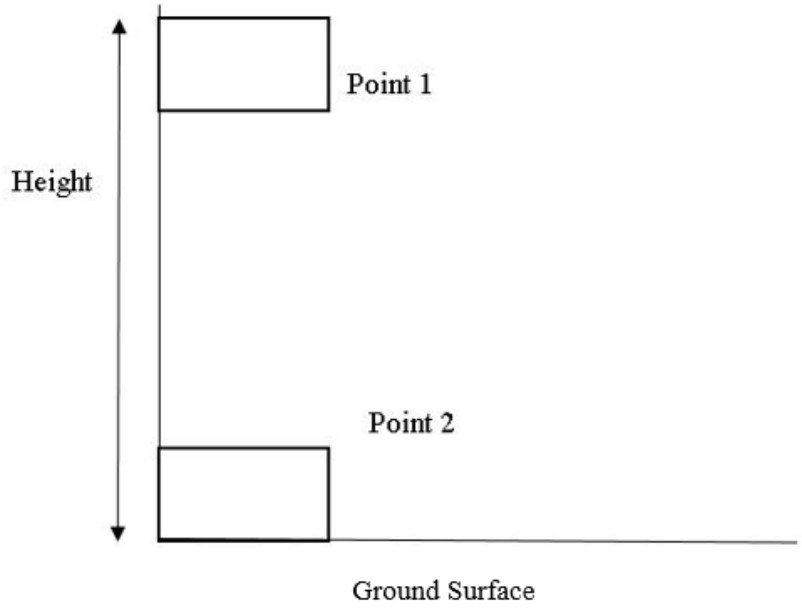

Figure 3.27 A representation of the preliminary impact energy model, a failure mass falls some height away from the failure surface onto a slope below, in the future this model would be calibrated for Path 1 and Path 2.

Figure 3.27 displays the basis of the impact energy model. The failure mass falls from some height (H) and impacts on a stiff surface which does not deform upon impact. In the future, this

model will be completed utilizing Travel Path 1. It is assumed that no rotation occurs during the fall and the block or cylinder hits flat on its face. It becomes difficult to calculate the surface area of the impact of the block or cylinder when it rotates and strikes the ground in another position besides what is shown in Figure 3.27. Therefore, this model is not used to describe horizontal distance as the transition between two slopes would cause an impact to occur on an unknown surface area. Friction and air resistance are neglected in this model. This model assumes that energy is conserved and Point 1 is equal to Point 2:

$$PE = IE = EL \tag{3.33}$$

where *PE* is potential energy, *IE* is potential spring energy of the block and *EL* is energy lost to impact. The mass upon impact with the ground is assumed to deform acting like a compressed spring:

$$IE = \frac{1}{2}kx^2 \tag{3.34}$$

where *x* is the amount of deformation and *k* is a spring constant which can be calculated utilizing Hook's Law:

$$\frac{kx}{A} = E\frac{d}{l} \tag{3.35}$$

where *k* is the spring constant, *x* and *d* is the amount of which the block deforms by, *A* is the area of impact, *E* is the modulus of elasticity and *l* is the undeformed length of the block. The spring constant is calculated by:

$$k = E\frac{A}{l} \tag{3.36}$$

Substituting equation 3.36 into the *k* value of equation 3.34 gives:

$$IE = \frac{1}{2} E \frac{A}{l} asl^2 \tag{3.37}$$

$$IE = \frac{1}{2} EAlas^2 \tag{3.38}$$

where *as* is the axial strain of the material is divided by 100 to represent the degree of deformation which the material undergoes. For the mass to fragment the potential spring energy of the rock would need to be exceeded, once this has occurred any other energy would be lost.

The deformation of the mass is assumed to be the axial strain multiplied by the length of the body of the sample. The axial strain of the material is determined from a uniaxial compressive strength test and is a measurement of how much the sample deformed before breaking (Saadati et al., 2018).

3.6.2 Results

A parametric analysis was completed to determine how each parameter affects the energy lost to impact. The parametric analysis considered the change in mass, initial height, the surface area of impact and the mass geometry.

The constant values are displayed in Table 3.5. The values for granite were obtained from Saadati et al. (2018). Granite was chosen for the parametric analysis as it displays brittle deformation during a uniaxial compression test which follows closely to the impact behaviour of a material (Saadati et al., 2018). An arbitrary size was chosen for the block as this model is in its preliminary stages and does not represent a complete rock avalanche event.

Table 3.5 The constants for the parametric analysis completed, the values for the rock were obtained from Saadati et al. (2018), an arbitrary size was chosen for the block as this model is in its preliminary stages.

Variable	Value	Unit
E	32.2	Gpa
as	0.117	
ρ	2700	kg/m^3
V	0.000051	m^3
A	0.0008	m^2
L	0.062	m
H	200	m
g	9.81	m/s^2

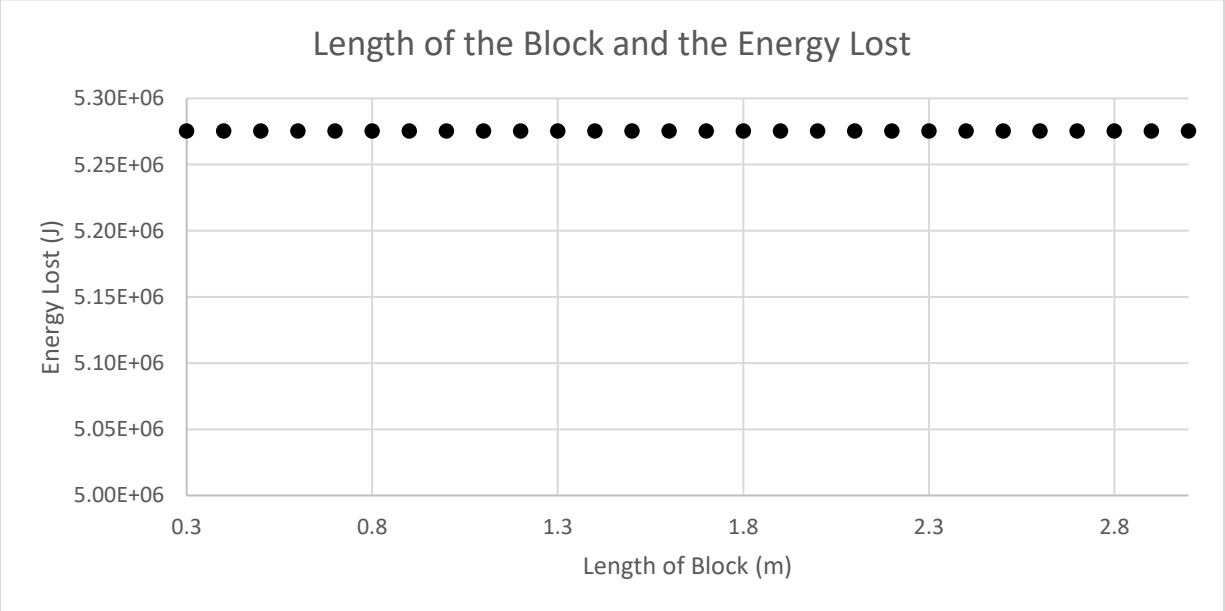

Figure 3.28 The length of the block was increased and the energy lost to impact did not change thus the energy term is not dependent on the length of the block.

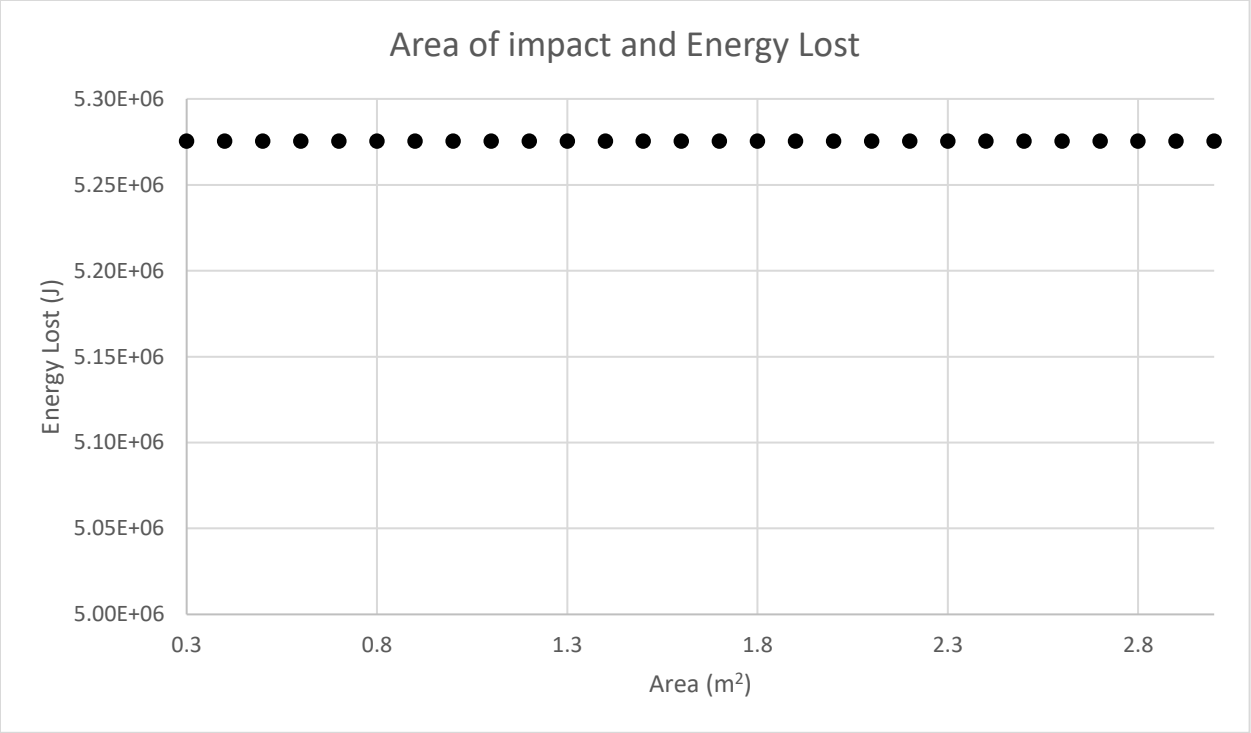

Figure 3.29 The surface area of the block at impact was increased and the energy lost to impact did not change, thus the energy term is not dependent on the geometry of the block itself.

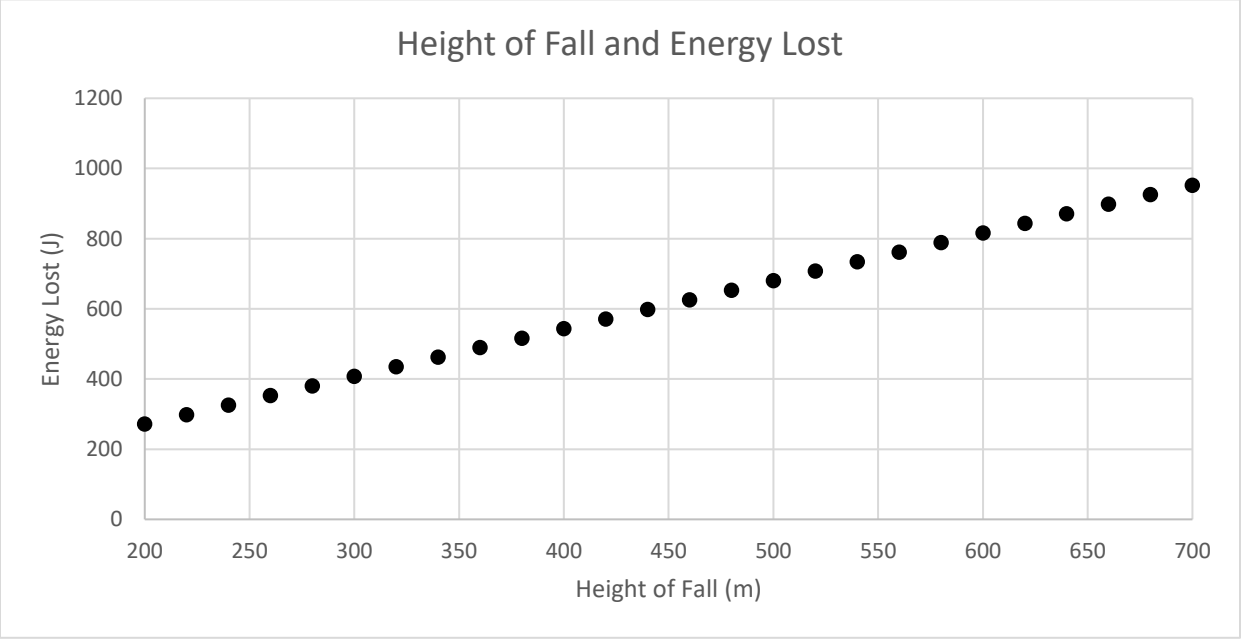

Figure 3.30 As the height at which the block fell was increased, the energy lost to impact also increased displaying that the impact energy is dependent on the height of which the block fell.

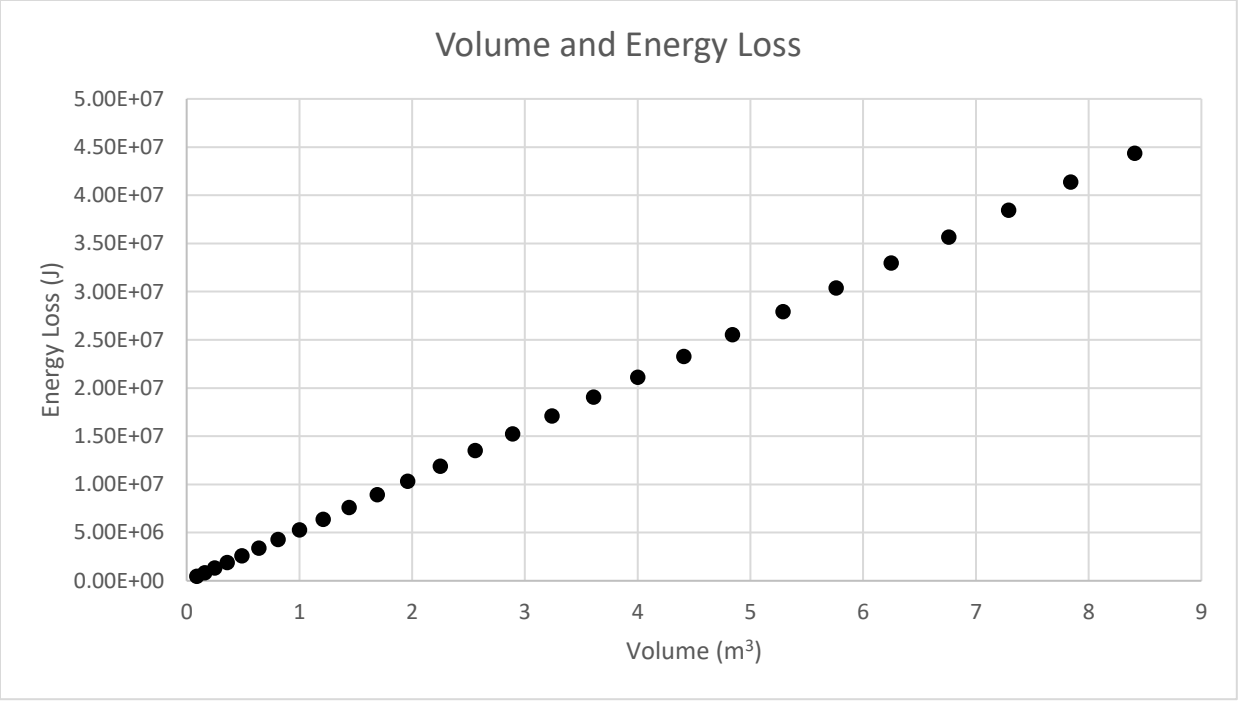

Figure 3.31 The energy lost to impact is directly related to the mass or volume of the block, as the volume of the block was increased and the energy lost to impact also increased. The impact energy term is a mass dependent term.

3.6.3 Discussion

Increasing the volume and height from which the block is dropped increases the energy lost at impact as displayed in Figures 3.30 and 3.31 respectively. The potential spring energy of the sample does not depend on the potential energy of the system; thus, the potential spring energy does not change with increasing potential energy. The excess energy not consumed by the potential spring energy is either lost to impact or stays within the system and is consumed by either fragmentation or friction. The amount of excess energy is directly related to the potential energy.

As shown in Figures 3.28 and 3.29 the change in impact surface area and change in the block length does not affect the energy lost to impact. Thus, the impact energy model is dependent on the initial mass of the block.

The impact energy model requires further research to include this process in a simple sliding energy model with the consideration of brittle behaviours of rock, to fully understand how energy is lost to this process. As well, further work is required to determine the impact surface area of the failure mass when it initially falls onto the lower slope.

3.7 The Utilization of Blasting Equations to Represent Fragmentation

Blasting equations have been used to quantify rock avalanche fragmentation as shown by Locat et al. (2006). Rock blasting and rock avalanche fragmentation are unique processes and blasting equations likely do not provide an accurate representation of rock avalanche fragmentation. Since the Locat et al. (2006) model is based on blasting theory a few assumptions would vary from field observations. The blasting theory was designed to break a rock mass in an efficient and controlled manner with the product being a material with a fairly uniform grain size to ease transportation and processing (Wyllie and Mah, 2004). Rock avalanche deposits do not display a uniform grain size, rather the grain size ranges from micrometres to blocks larger than houses (Dunning, 2006; Dufresne et al., 2016b; Dufresne and Dunning, 2017; Zhang and McSaveney 2017). Further, when blasting a rock mass a grid-like pattern is utilised to ensure that the energy required to break the rock radiates equally throughout the mass (Wyllie and Mah, 2004). Lastly blasting aims to break a rock in tension as rocks are weakest in this manor and it would utilise the least amount of energy (Wyllie and Mah, 2004).

The Locat et al. (2006) model does not account for the initial geometry of the rock mass, the ground stiffness of the lower slope and the impact energy of the failure mass on the slope. It has been observed that the rock mass will fragment along pre-existing discontinuities and is dependent on the initial join set, impact energy and ground stiffness (Turcotte, 1986; Ruiz-Carulla

et al., 2017; Zhao et al., 2017, 2018). The energy lost to the impact between the rock mass and the ground or another obstacle such as loose materials on the slope is likely the energy consumed by fragmentation.

Rock avalanche fragmentation more than likely originates from the face which impacts the ground and the energy would radiate throughout the block originating from the impact face. This would cause a nonuniform grain size as the rock mass at the impact face would be pulverised to fine-grain particles while the rock mass furthest from the impact would not receive the same energy and would break into larger fragments (Farin et al., 2014; Zhao et al., 2017). Rock avalanche fragmentation is likely due to a rock mass breaking in compression rather than tension. Overall rock avalanche fragmentation is a chaotic uncontrolled process when compared with the blasting of a rock mass.

Davies et al. (2019) found that energy lost or required by fragmentation was greater than what was available in the system. In constrast De Blasio et al. (2018) found that fragmentation energy only required 0.2 to 18% of the total energy available in the system. The discrepancy between the two models highlights the knowledge gap in this area of research.

3.8 Accuracy of the Apparent Coefficient of Friction Values

Using the entrainment, fragmentation and real-world data it was determined that the calculated horizontal distance travelled by a rock avalanche is less than the actual distance travelled when it is assumed that the apparent coefficient of friction was the Heim's Ratio value. The results of this analysis are shown in Table 3.6. The consistent underestimation of the horizontal distance

travelled by a rock avalanche by both the entrainment and fragmentation energy models led to further investigation to determine the cause.

The calculated horizontal travel distance is underestimated by 2 to 32 % that represents a significant reduction in the run out values.

Table 3.6 Comparison of the lengths calculated utilizing the entrainment and fragmentation models which assume the apparent coefficient of friction value is the Heim's Ratio value of the events and actual horizontal lengths travelled by rock avalanches, data from (Evans and Hungr, 2004; Geertsema et al., 2006; Locat et al., 2006).

Name	Length (m)	Length Calculated (m)	% Reduction
Frank Slide	3500	3034	13
Slide Mountain	1650	1309	21
Queen Elizabeth	2645	2309	13
Jonas Creek north	2800	2665	5
Jonas Creek south	1830	1774	3
Claps de Luc	800	716	11
La Madeliene	4500	3825	15
Arvel	350	290	17
Nomash River	2270	1552	32
Pink Mountain	1950	1914	2

The apparent coefficient of friction value is not known for rock avalanches as we can not directly measure for it (Cruden, 1980). A common assumption in rock avalanche literature is to assume that the apparent coefficient of friction value is equal to Heim's Ratio value for each event. However, this assumption may be incorrect, as shown in Section 3.2.1, Heim's Ratio (taken as the representation of the coefficient of apparent friction) was derived from a simple sliding energy model which only considers potential and frictional energy. When the entrainment and fragmentation energy models are solved for the apparent coefficient of friction value, the equations

do not simplify to Heim's Ratio as shown in equations 3.39 and 3.40 respectively. This prompted an analysis of the validity of using Heim's Ratio as the apparent coefficient of friction value for energy models which consider other energy terms besides potential and frictional energy:

$$\mu = \frac{m_1 g h_1 + m_2 g h_2 - KEl_1}{(m_1 + m_2) gL - m_2 g cos\theta d_1} \tag{3.39}$$

$$\mu = \frac{gh - 3600wb}{gL} \tag{3.40}$$

For the examples considered, the height, mass, degree of fragmentation, and amount of mass entrained have been directly observed whereas the apparent coefficient of friction has not. Instead of utilizing the models to solve for the horizontal distance travelled, the entrainment and fragmentation energy models have been utilised to solve for the apparent coefficient of friction value. Table 3.7 displays the new apparent coefficient of friction values which have been calculated using Microsoft Excel's Goal Seek Function.

From Table 3.8, there is a reduction of 3 to 33% of the calculated (Goal Seek) apparent coefficient of friction value when compared with Heim's Ratio values suggesting that actual runout exceeds that inferred by Heim's Ratio. As stated earlier, Heim's Ratio is derived from a simple sliding energy model which fails to account for other energy terms such as energy lost to inelastic collisions.

Table 3.7 Comparison of Heim's Ratio as the apparent coefficient of friction value (μ) and a calculated μ value using rock avalanche data and the entrainment and fragmentation models to analyse the difference of the two values.

Name	μ = H/L	μ (Goal Seek)	% μ Reduction
Frank Slide	0.22	0.19	13
Slide Mountain	0.25	0.20	21
Queen Elizabeth	0.36	0.31	13
Jonas Creek north	0.31	0.29	5
Jonas Creek south	0.49	0.48	3
Claps de Luc	0.46	0.41	11
La Madeliene	0.28	0.24	15
Arvel	0.71	0.59	17
Nomash River	0.24	0.16	33
Pink Mountain	0.25	0.20	20

The continued use of Heim's ratio in models which consider other energy loss values would yield inconsistent results. This may already be occurring in current literature as Davies et al. (2019) utilised the Heim's Ratio value as the apparent coefficient of friction value for their fragmentation energy model, which may account for the error observed in their model. Davies et al. (2019) concluded that the fragmentation energy term consumed more energy than what was available in the system, although this may not hold if a lower apparent coefficient of friction value is utilised.

When utilizing energy models besides the simple sliding energy model, Heim's Ratio is not a sufficient assumption for the apparent coefficient of friction value. A calibrated apparent coefficient of friction value would provide improved accuracy and could provide insight into the coefficient of friction.

Chapter 4 : Galileo Scaling and Rock Avalanche Geometry

4.1 Introduction

Through the statistical analysis of various rock avalanche databases, an interesting relationship between volume, area, horizontal length travelled, and Heim's Ratio has been noted. The volume and the horizontal distance travelled appear to follow a square-cube scaling relationship. A square-cube scaling relationship was derived by Galilie (1638) to describe how the various parameters of an object would change if the volume of the object was increased or decreased. Galilie (1638) square-cube scaling law states that as the size of an object is increased, the volume of the object will increase greater at a greater rate proportional to the surface area of the object. For a given object such as a cube, if the size of the cube was to be increased, the volume would increase at a greater rate proportional to that of the surface area as shown in Figure 4.1. This theory can be applied to other parameters such as the resting heart rate for varying sizes of mammal species. The relationships between volume and area, volume and Heim's Ratio and volume and horizontal distance travelled have been noted to potentially follow a square-cube scaling law (Davies, 1981; Hungr, 1990; Hungr and Evans, 2004; Delaney and Evans, 2014). Delaney and Evans (2014) were the first to recognise this as Galiloe Scaling.

These relationships can be considered as empirical models and could potentially be used as predictive tools for determining the distance a rock avalanche will travel as well as the deposit area (Whittall et al., 2019). This chapter will not go into detail about the efficiency of these models as predictive tools. Instead, this chapter provides a preliminary analysis for these relationships.

To perform the statistical analysis, a database was created using rock avalanche information available in the literature and can be found in Appendix A. Table 4.1 displays an example of the information provided in a typical rock avalanche database in the literature.

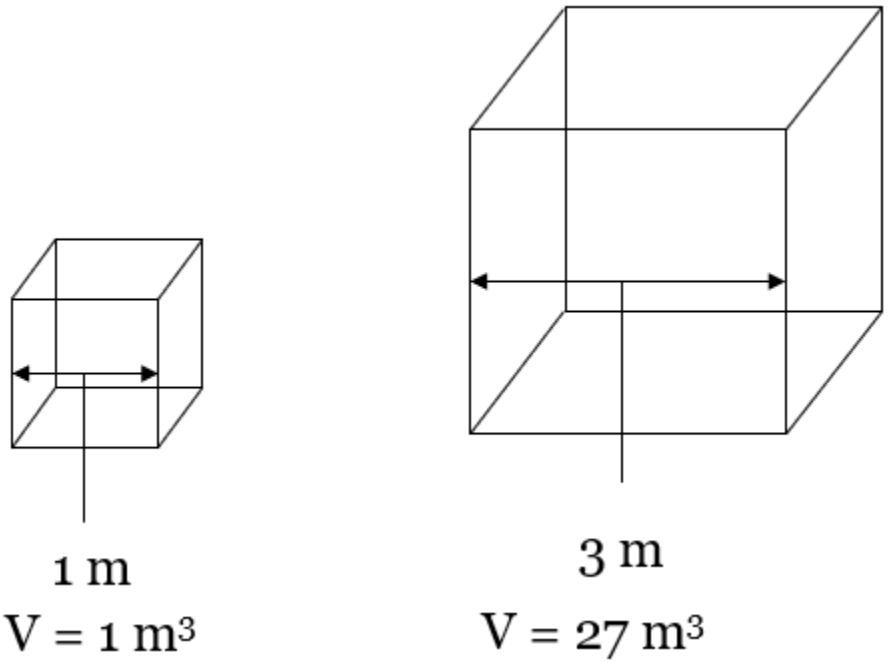

Figure 4.1 A visualisation of Galileo Scaling, as the cube increases in size, the volume will increase at a greater rate proportional to the that of the surface area of the cube, as defined by Galilie (1638).

Table 4.1 The ten largest rock avalanches in the database and the information currently available from databases in literature, the location, thickness of the deposit, depositional length, and rock type were not provided.

Name	Location	Height (km)	Length (km)	H/L	Volume (km^3)	Area (km^2)	Thickness (m)	Deposition Length (m)	Rock Type	Reference
Popocatepetl		4	33	0.12	28					Legros, 2002
Shasta		3.55	50	0.071	26	450				Legros, 2002
Saidmarreh		1.5	18.9	0.079	20					Legros, 2002
Socompa		3.25	35	0.092	17	480				Legros, 2002
Peteroa		3.9	85	0.045	16					Legros, 2002
Meru		3.9	50	0.078	15	1400				Legros, 2002
Colima		4	40	0.1	12.5	900				Legros, 2002
Flims		2	15.6	0.12	12					Legros, 2002
Yatsugatake (Nirasaki)		2.4	32	0.075	9					Legros, 2002
Chimborazo		3.6	35	0.1	8.1					Legros, 2002
Egmont (Pungarehu)		2.6	31	0.083	7.5	250				Legros, 2002

Typically, the only information available from the datasets is the name of the rock avalanche, a vague or rough location of the deposit, the height and length it travelled and the volume. Further information such as geology, path topography, the thickness of rock avalanche deposit, the depositional area is not typically available in the published data. From the database, 36% of datasets did include deposit length, thickness, area, or geology of the rock avalanche. This data has been included in the database when this information is provided. The statistical analysis considers the following parameters: volume, horizontal distance travelled, vertical distance travelled, apparent coefficient of friction determined from Heim's Ratio, thickness, area and deposit length. Geology was not considered as there was insufficient data to create meaningful results as only 17% of cases included geological information, and 3% were of the same rock type.

4.2 Results

The relationships considered for the statistical analysis are volume and Heim's Ratio, area and Heim's Ratio, volume and area, volume and deposit thickness, area and thickness, volume and horizontal distance travelled, and volume and length of the deposit. Except for the area and deposit thickness plot, the figures have been plotted on a log-log scale to better display the relationships between parameters. The results of the statistical analysis are shown in Figures 4.2 to 4.8.

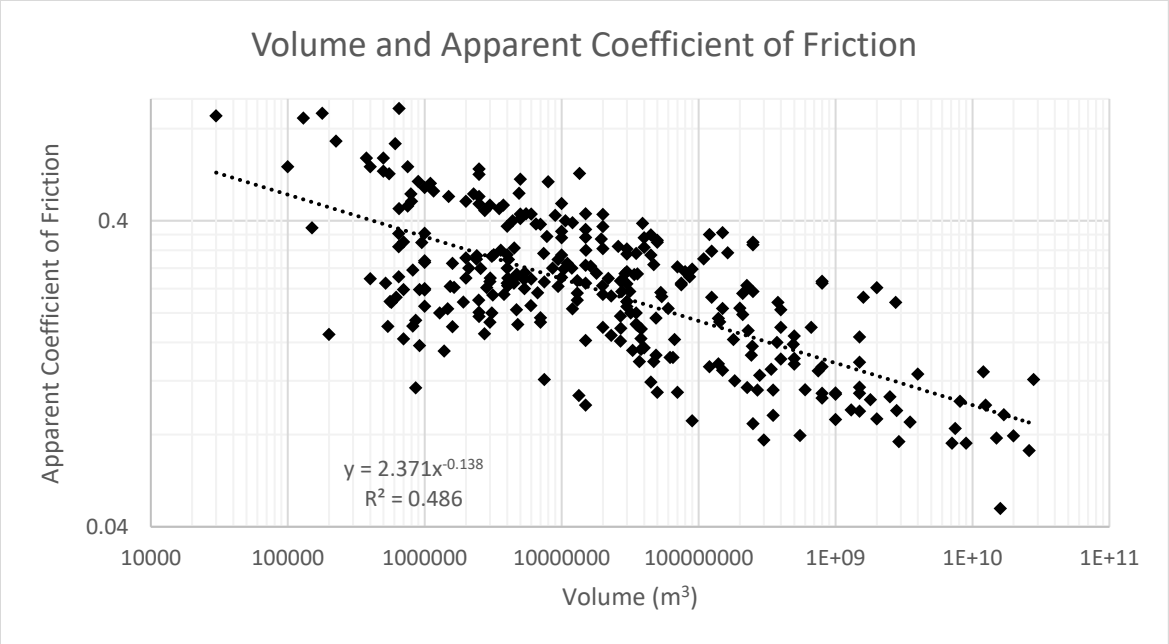

Figure 4.2 Comparison of the volume and apparent coefficient of friction or Heim's Ratio, as the volume increases the Heim's Ratio decreases, N = 336.

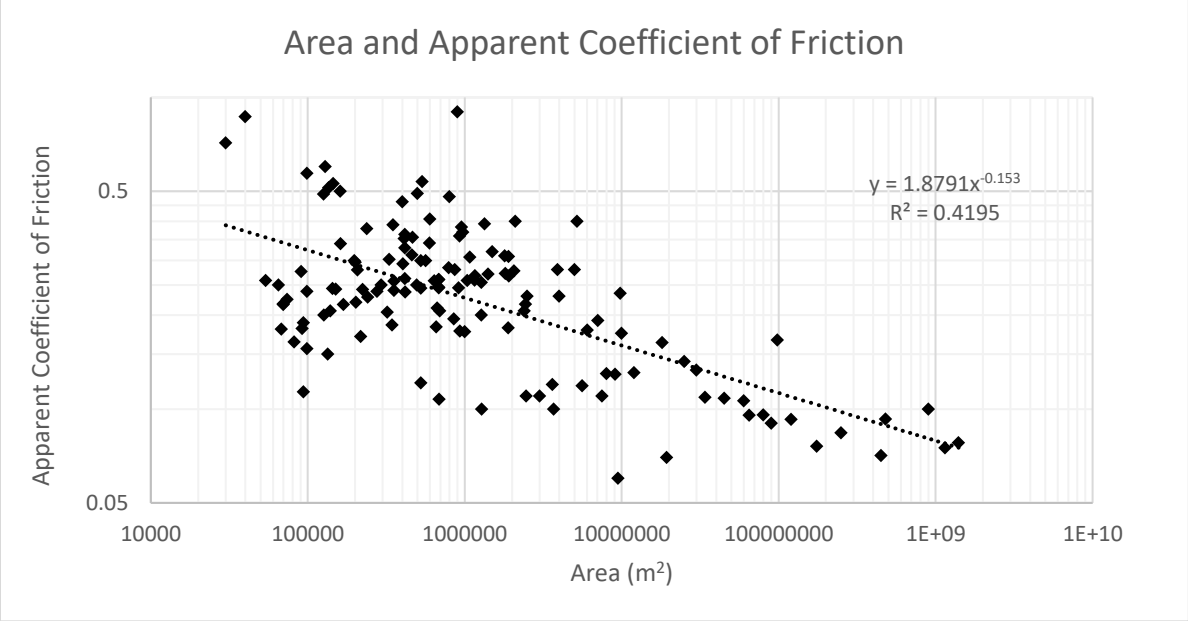

Figure 4.3 A comparison of the area and the apparent coefficient of friction or Heim's Ratio, as the area increases the Heim's Ratio decreases, following a similar trend as the previous analysis. There are less data points in this analysis as area is not as often recorded as volume, N = 143.

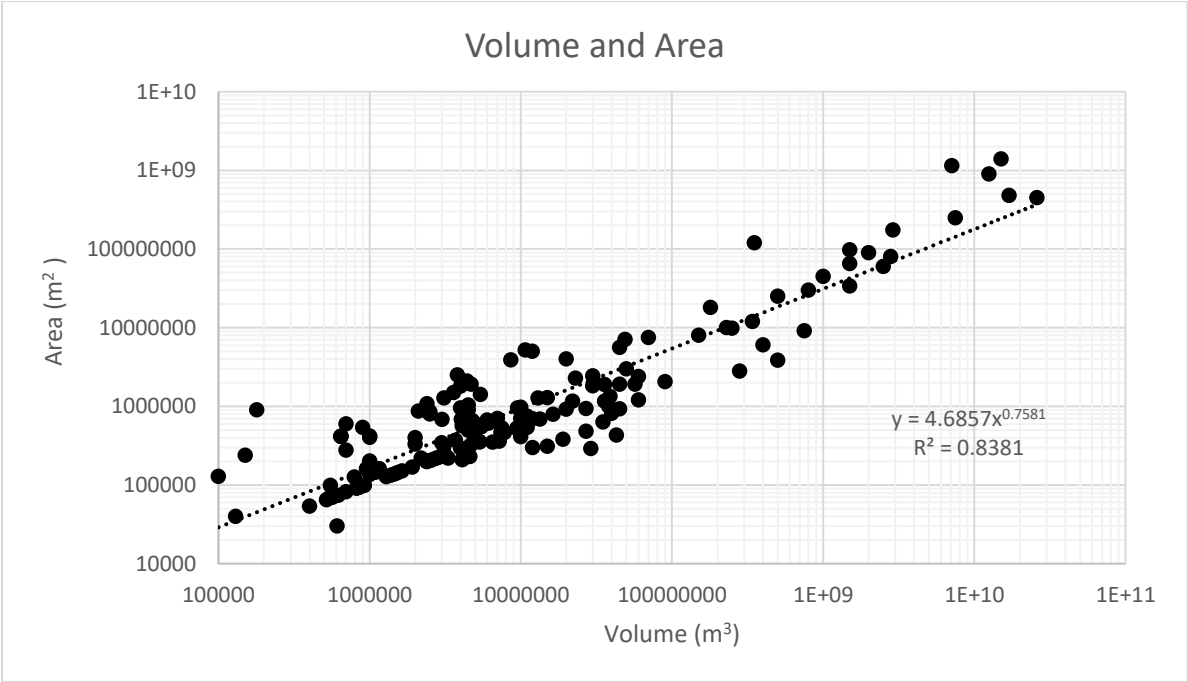

Figure 4.4 The analysis of the volume and area, as the volume increases, the depositional area also increases, the data is well confined about the trendline, N = 162.

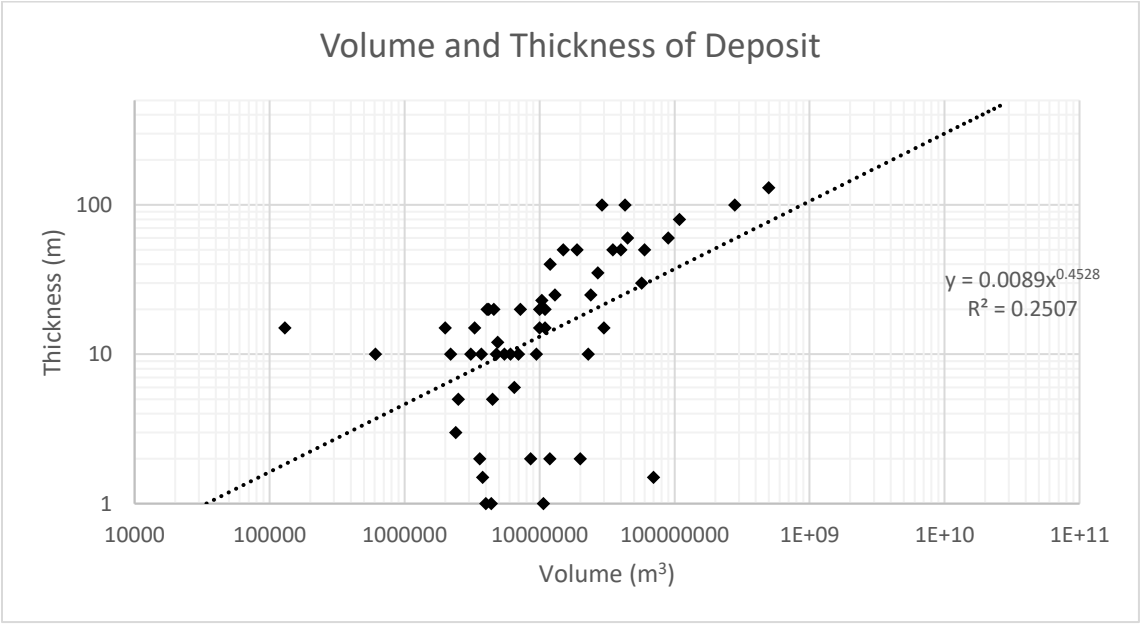

Figure 4.5 The comparison of the volume and deposit thickness, a general trend does appear in that as the volume increases the deposit thickness also increases, better data is required to further analyse this relationship, N = 54.

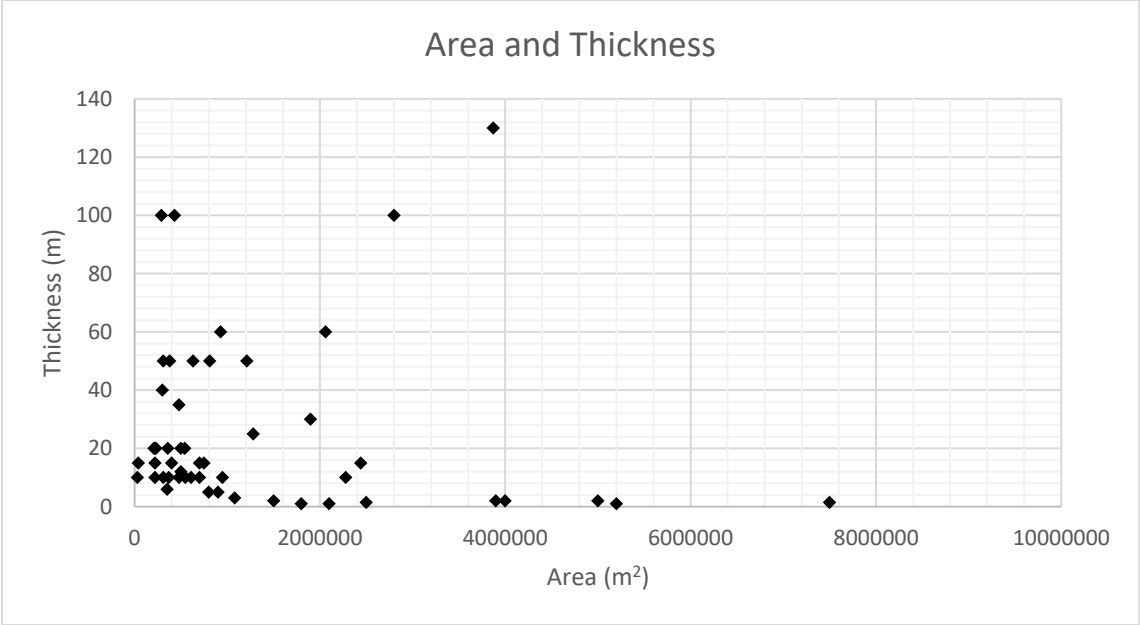

Figure 4.6 The analysis of the area and thickness of a deposit, a relationship is not observed between these two parameters, N = 54.

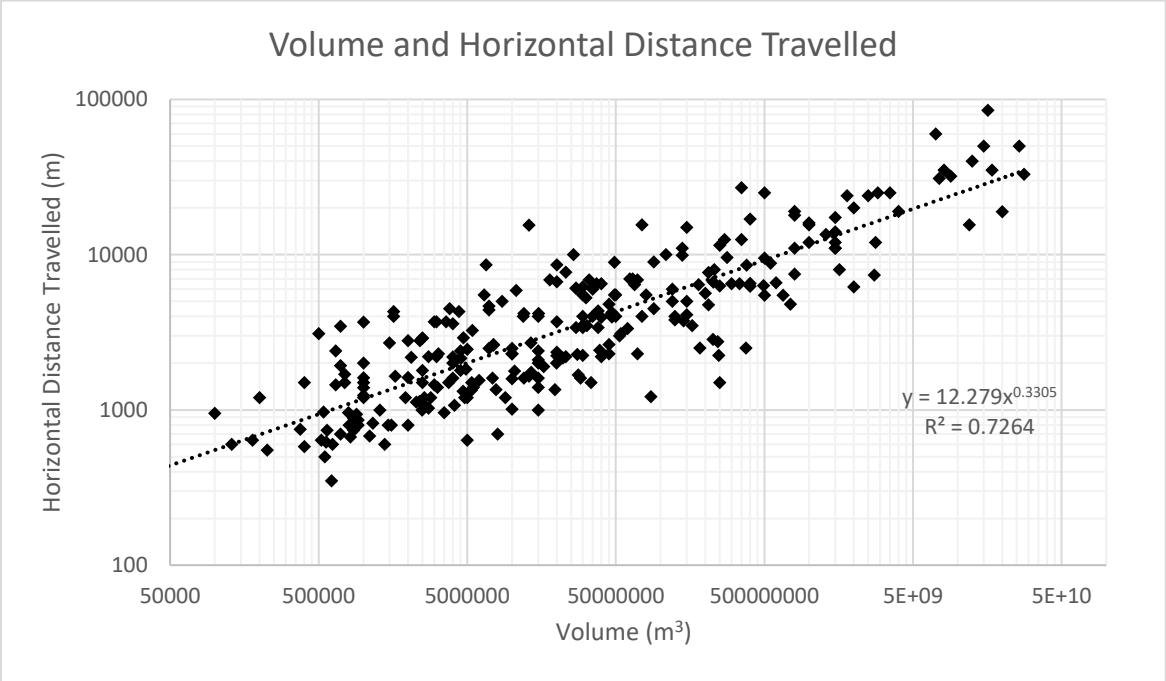

Figure 4.7 The analysis of the volume and horizontal distance travelled, as the volume increases the horizontal distance travelled also increase, the slope of the trendline is 0.33, or Galileo Scaling, N = 336.

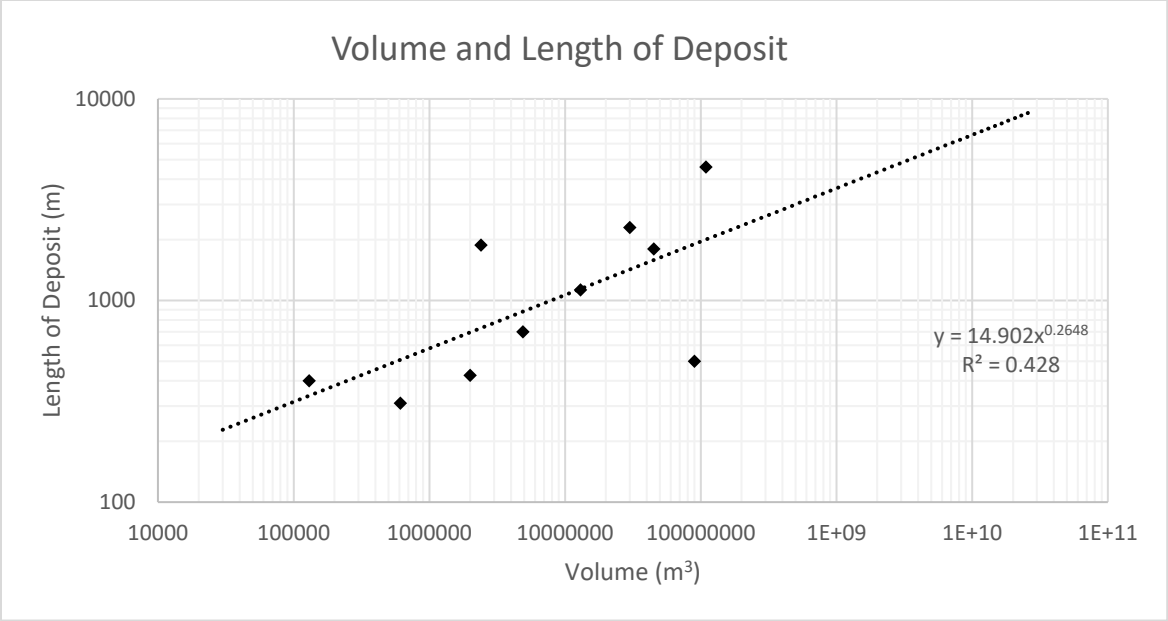

Figure 4.8 Comparison of the volume and length of the rock avalanche deposit, there is a correlation between these two parameters in that as the volume increases, the length of the deposit also increases, more data is required to confirm this relationship, N = 9.

From Figures 4.2 to 4.8, only one parameter analysis did not show a significant relationship or trend when plotted. Figure 4.6 displays the analysis of the depositional area and the reported thickness of the deposit, and no significant relationship is observed between these two parameters. Thus, the thickness of the deposit is not dependent on the depositional area of a rock avalanche. This could be due to the lack of recorded thicknesses of rock avalanche deposits. The reported thickness does appear to be related to the volume, however, as shown in Figure 4.5. As the volume increases the thickness of the rock avalanche also increases suggesting that a certain thickness is required for rock avalanche movement. From Figure 4.4, as the volume increases the depositional area also increases and since both area and thickness are dimensional parameters if the volume increased, the thickness and area should increase as well. This is further supported by Figure 4.8, which shows that as the volume increases so does the length of the deposit.

Another trend to note which is displayed in both Figures 4.2 and 4.3 is that the Heim's Ratio decreases with increasing volume and area. The relationship between the parameters does display a large scatter, with the similar volume rock avalanches having a large range in Heim's values (eg. Volume of 1M m3, the Heim's value ranges from 0.1 to 0.9). The scatter is most likely due to external factors (e.g. geology, environment, degree of path confinement, and potential trigger mechanisms) which affect rock avalanche runout that is not accounted for through this correlation.

Lastly, Figure 4.7 displays the relationship between volume and the horizontal distance travelled by a rock avalanche. As the volume increases, the horizontal distance travelled by the rock avalanche also increases. However, there is a large degree of scatter about the trendline, for a volume of 5 Mm^3 there is a horizontal distance travelled of 650 m and 9000 m. This variance in the degree of magnitude difference the runout distance can have for similar volumes is not acceptable for a prediction tool. This could mean the difference between catastrophic and non-catastrophic effects from the rock avalanche. The methods to further constrain the scatter present in the data will be discussed in section 4.4.

4.3 Discussion

The volume and horizontal distance travelled appears to follow a Galileo Scaling relationship, as the slope of the trendline is 0.33. The volume, area and Heim's Ratio also appear to follow some sort of scaling relationship that is not Galileo Scaling.

As noted in the previous section, there is significant scatter. A method that is commonly utilised for building empirical relationships is to divide the database down into smaller datasets

based on the general location of the rock avalanches. Using this method of analysis, three new datasets were considered alongside the Legros (2002) database. The Legros (2002) database is a baseline to compare the results of the new datasets as it is a large database. The three different datasets were based on the location of which the rock avalanche occurred: Norway, China and Canada (Cruden, 1976; Eisbacher, 1977, 1979; Clague and Souther, 1982; Cruden, 1982; Cruden and Eaton, 1987; Jackson and Isobe, 1990; Ryder et al., 1990; Evans and Clauge, 1991; Evans et al., 2001; Levson et al., 2003; Hungr and Evans, 2004; Huscroft et al., 2004; Orwin et al., 2004; Geertsema et al., 2006; Brideau et al., 2010; Brideau et al., 2012; Guthrie et al., 2012; Hermanns et al., 2012; Sakals et al., 2012; Blais-Stevens et al., 2015; Schleier et al., 2017; Zhan et al., 2017; Mitchell et al., 2019). The results are shown in Figures 4.9, 4.10 and 4.11 and Tables 4.2, 4.3 and 4.4.

Figures 4.10 and 4.11 show a correlation between the parameters however these relationships do not necessarily follow Galileo Scaling as the exponents are not 0.33 or 0.66. Further, from Figure 4.10, the trendlines exponents vary greatly between the datasets with none following Galileo Scaling. From Table 4.4, the R^2 values of both the Chinese and Canadian databases are low. The Norwegian database is not considered for Figure 4.9 as the area was not recorded for any of the events.

Table 4.2 The equation of the trendline and R^2 value for Figure 4.9.

Dataset	Trendline Equation	R^2	N
Legros, 2002	$y = 8x^{0.36}$	0.81	81
Norway	$y = 93x^{0.18}$	0.36	24
China	$y = 6x^{0.36}$	0.84	37
Canada	$y = 90x^{0.21}$	0.47	29

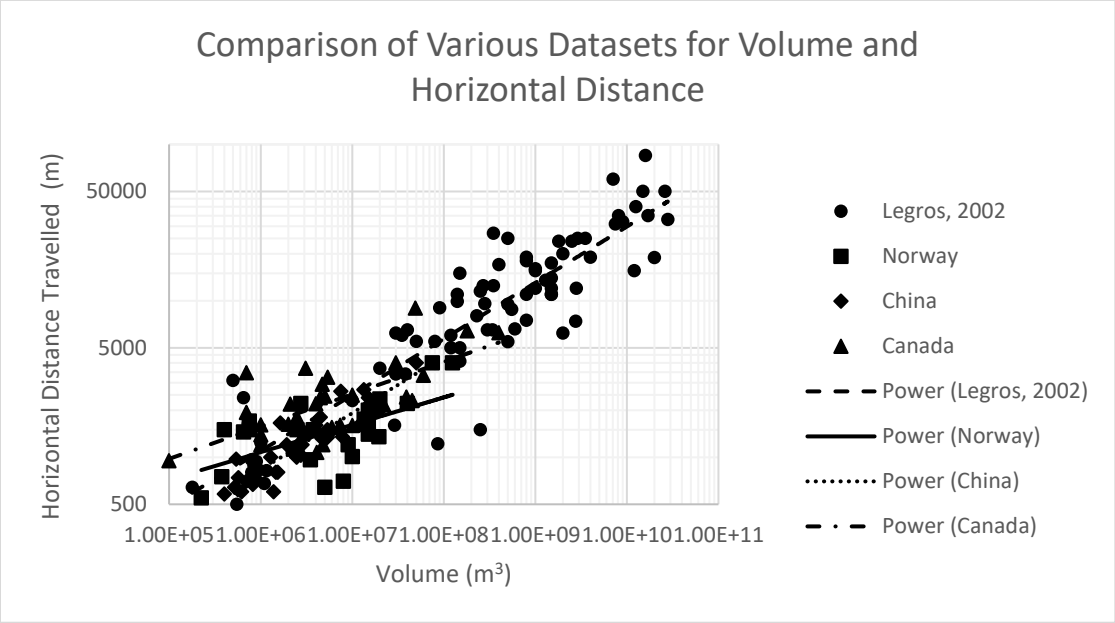

Figure 4.9 The analysis of volume and horizontal distance travelled from the four datasets, the equations of the trendlines and the R^2 values can be found in Table 4.8, the Legros, (2002) and Chinese database both have slope values of 0.36, whereas the Norwegian and Canadian databases have trendline values of 0.18 and 0.21 respectively.

Table 4.3 The equation of the trend lines and R^2 values for Figure 4.10.

Dataset	Trendline Equation	R^2	N
Legros (2002)	$y = 6x^{0.78}$	0.92	81
Norway	N/A	N/A	0
China	$y = 325x^{0.51}$	0.73	37
Canada	$y = 2x^{0.78}$	0.98	29

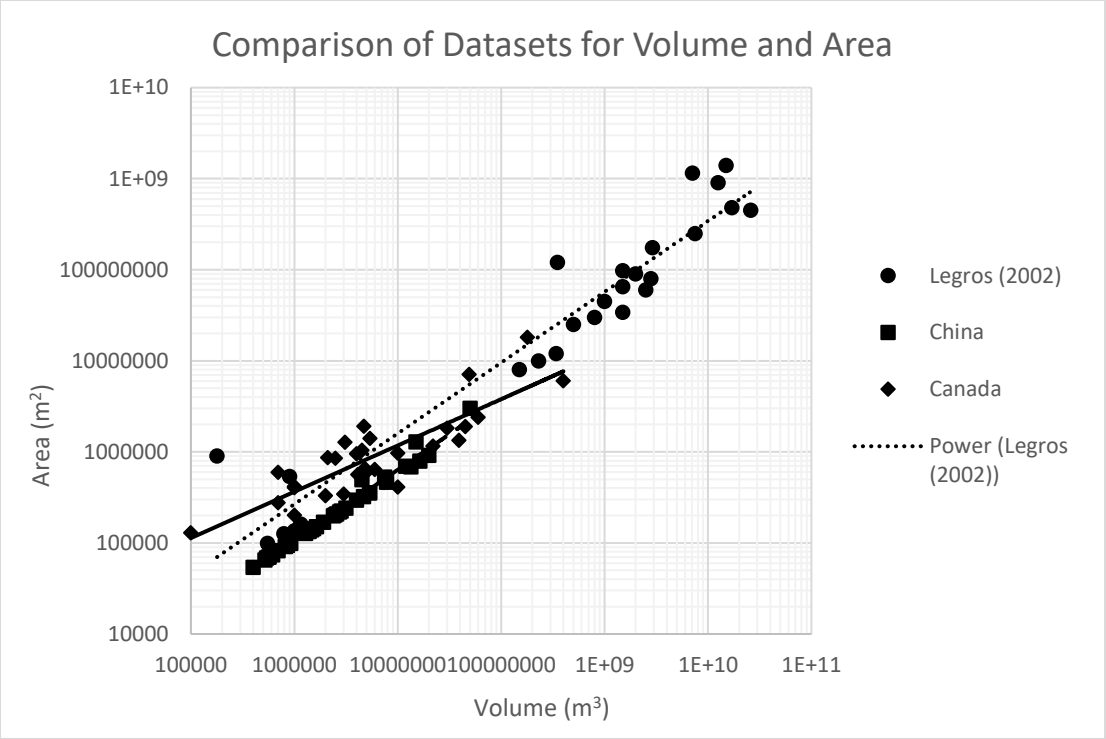

Figure 4.10 The analysis of the volume and area using the Legros (2002), Chinese and Canadian database, the Norwegian database did not list area for the rock avalanche deposits and is not included in this analysis. The trendline equations and R^2 values can be found in Table 4.3.

Table 4.4 The equation of the trend lines and R^2 values for Figure 4.11.

Dataset	Trendline Equation	R^2	N
Legros (2002)	$y = 7x^{-0.19}$	0.75	81
Norway	$y = 6x^{-0.16}$	0.70	24
China	$y = 0.41x^{-0.047}$	0.03	37
Canada	$y = 0.84x^{-0.73}$	0.19	29

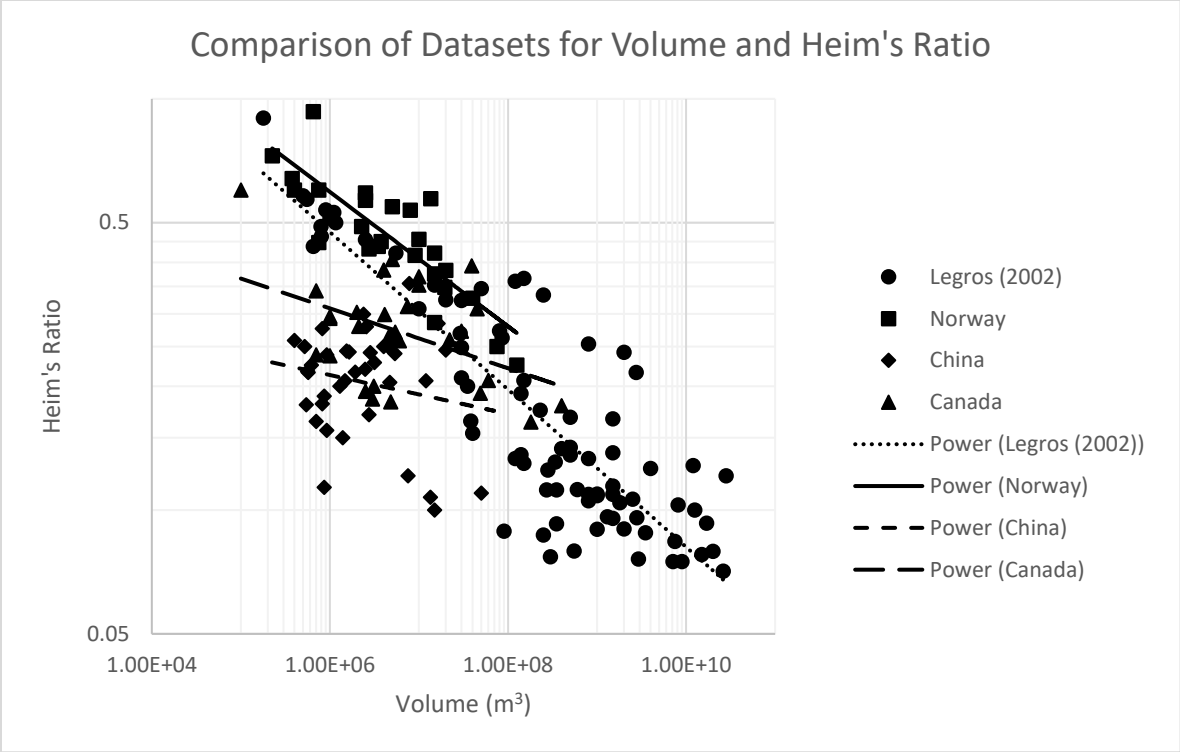

Figure 4.11 The analysis of the volume and Heim's ratio using four datasets, the equation of the trendlines and R^2 values are listed in Table 4.4, the slopes of the four trendlines vary, with the Chinese trendline having a slope value of 0.047, and the Canadian database having a slope value of 0.73.

Figure 4.9 illustrates an important knowledge gap in rock avalanches. The Legros (2002) dataset is created of rock avalanches on a global scale, which would average the trendline to Galileo Scaling. Examining the individual datasets, the Chinese dataset consists of similar rock avalanche events whereas the Norwegian and Canadian datasets do not. The Chinese dataset of rock avalanches originates from the 2008 Wenchuan earthquake and occur in similar geologies and environments. This increases the confinement of the data about the trendline as the rock avalanches would have similar dictating properties. The Norwegian and Canadian datasets consist of rock avalanches from across their respective countries and generally occur within a similar time span. These rock avalanches occurred under different conditions and have different controlling

properties, essentially the data is not well confined. These datasets could be reorganised in a way that would allow for improved organization of the data and potentially increase our understanding of rock avalanches. Nicoletti and Sorriso-Volva (1991), Straub (1996) and Mitchell et al. (2019) have determined that environment, topography, and source geology can affect the horizontal distance and Heim's Ratio for a given rock avalanche. Datasets could be reconstructed based on rock avalanche properties rather than location. Rock avalanches that occur in the same locality may not display similar characteristics and the properties dictating the horizontal distance travelled could vary drastically. For instance, a large factor that controls rock avalanche travel distance is if it is laterally confined. Rock avalanches may occur in the same area and one may be channelised and the other unconfined, where the latter does not travel as far as a channelised rock avalanche (Eisbacher, 1979). However, this information is rarely provided as shown in Table 4.5, as well as other prominent characteristics about rock avalanches such as their geology, degree of entrainment, the grain size of the deposit etc. Table 4.5 has been created to display the information provided in the Legros (2002) paper of the rock avalanches across the world. Due to data sparsity, further analysis to determine if datasets arranged by their properties rather than their location would yield better results can not be examined.

To examine the scaling relationship the volume and horizontal distance travelled were compared against a synthetic horizontal distance travelled value that has been calculated from Galileo Scaling. The results of this comparison are shown in Figure 4.11. The equation used to calculate the synthetic value from Galileo scaling is given as:

$$L_p = V^{0.33} \tag{4.1}$$

where L_p is the calculated horizontal distance from the Galileo Scaling and V is the volume of the rock avalanche.

Table 4.5 An example of the information available in a rock avalanche database (Legros, 2002).

Rock Avalanche Name	Location	Height (km)	Length (km)	H/L	V (Mm^3)	Area (km^2)
Asama		1.8	20	0.090	2	90
Bandai-san 1888		1.2	11	0.109	1.5	34
Bezymianni 1956		2.4	18	0.133	0.8	30
Callaqui		3.1	15	0.207	0.15	
Chaos Crags		0.65	5	0.130	0.15	8
Chimborazo		3.6	35	0.103	8.1	
Chokai		2.2	25	0.088	3.5	
Colima		4	40	0.100	12.5	900
Egmont (Pungarehu)		2.6	31	0.084	7.5	250
Egmont (Opua)		2.5	27	0.093	0.35	120

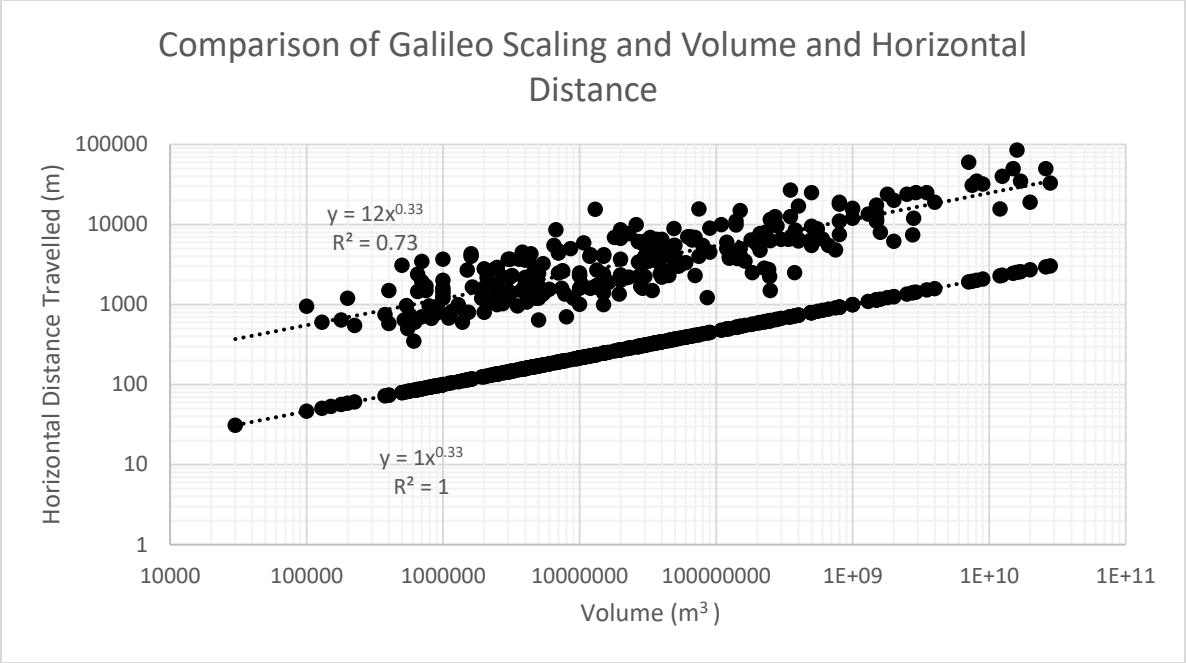

Figure 4.12 The synthetic Galileo Scaling values have been compared with the volume and horizontal distance travelled data, the synthetic Galileo Scaling values plot an order of magnitude below the actual data. The trendlines for these two datasets are parallel as both have a slope of 0.33.

From Figure 4.12, the horizontal distance travelled (L) calculated for a given volume (V) (based on Eq. 4.1) plots an order of magnitude below the volume and horizontal distance trend line. The trend line of the two datasets is parallel to each other (i.e., the exponent is 0.33) thus, showing that the volume and horizontal distance relationship follows a Galileo Scaling relationship. The order of magnitude difference between the two trend-lines is found to be 1 and there appears to be an offset between the two databases of about 12 (if we multiplied the Galileo Scaling values by 12, we would obtain a value close to the actual value of the rock avalanche). This value does not appear to be related to any rock avalanche parameter and changes when considering different databases. Figure 4.13 displays the three smaller databases compared against the synthetic Galileo Scaling value. The Chinese database appears to have a smaller offset value

of 6 whereas the Canadian and Norwegian databases are offset by 89 and 92 respectively, these values are obtained from the trendline equation. This value could be related to the degree of confidence of the dataset. Further work is required to determine why this value changes with different databases.

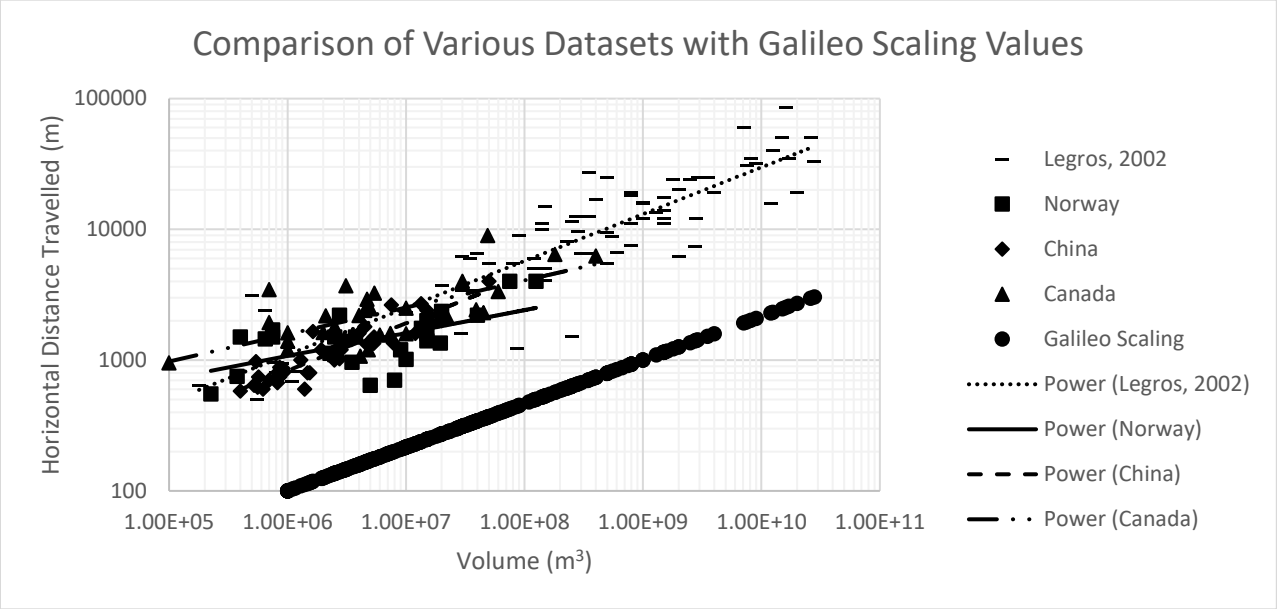

Figure 4.13 The comparison of the four smaller datasets with the synthetic Galileo Scaling values, again, the real datasets plot an order of magnitude above the synthetic values and the trendlines of the datasets appear to be parallel to the synthetic Galileo Scaling values with the exception of the Norwegian database.

The horizontal distance represented by Galileo Scaling underestimates the horizontal distance travelled by a rock avalanche in the field. Galileo Scaling appears to be a simple geometric concept that does not account for any of the mechanics and/or field conditions which cause an increase in the travel distance of a rock avalanche. However, this does not account for the scatter observed in the data, as discussed earlier, smaller datasets with similar characteristics will likely yield results that follow closer to a trend line. These smaller datasets could potentially be a useful simple prediction tool however further research is required.

The synthetic Galileo Scaling value was utilised to analyse the relationship observed between the volume and Heim's Ratio value in Figure 4.14. Figure 4.14 examines utilizing real height data of the rock avalanches and the synthetic horizontal distance travelled to calculate a new Heim's Ratio value. The new dataset was analysed with the real-world Heim's Ratio values.

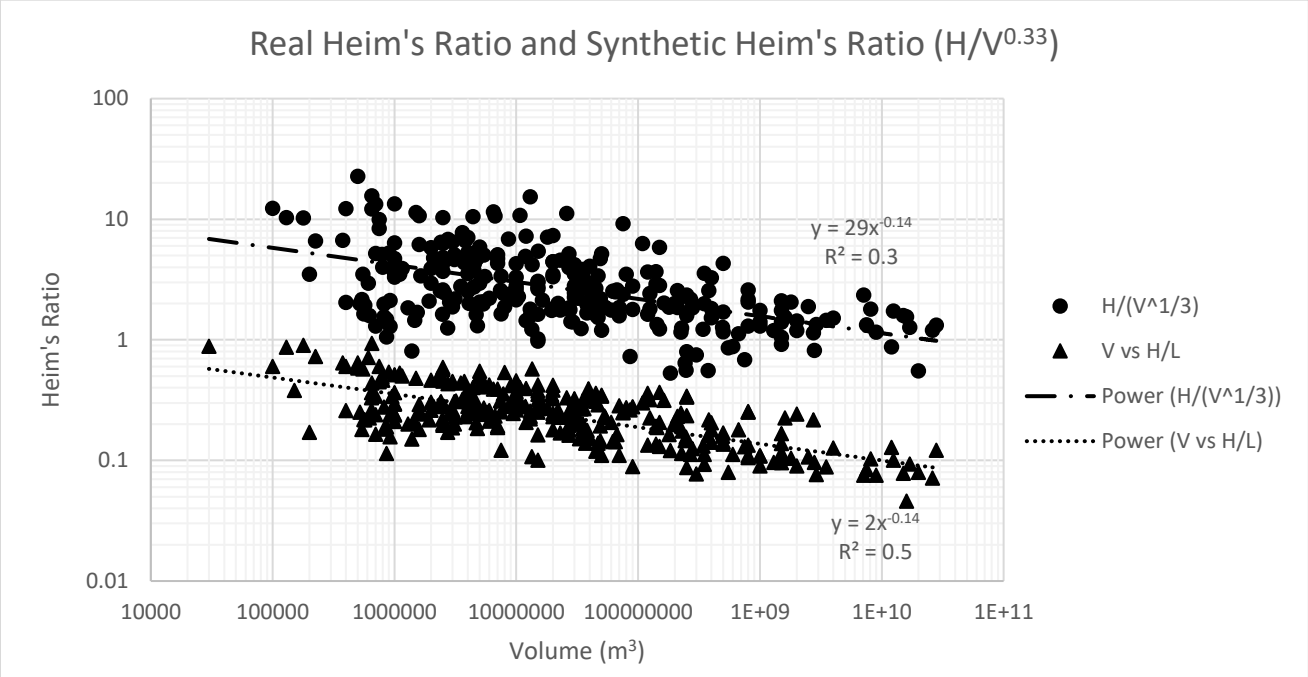

Figure 4.14 A synthetic Heim's Ratio value was compared with the actual Heim's Ratio value against volume, the synthitec Heim's Ratio was calculated by dividing the height of the rock avalanche by the synthetic length calculated from Galileo Scaling. The synthetic Heim's Ratio values plot above the actual as the length values calculated from Galileo Scaling are less than the actual lengths of the events.

The relationship observed in Figure 4.14 displays the comparison between the real Heim's Ratio values for rock avalanche events and a synthetic Hiem's Ratio value. This value was determined by utilizing real-world height data for rock avalanches and the synthetic horizontal distance value to calculate a new synthetic Heim's Ratio value. Per Figure 4.14, the trendline for these two databases appears to be parallel with an exponent of ~ 0.33 consistent with Galileo Scaling. The synthetic data points is offset by roughly an order of magnitude from the actual field

data. Again, it is not known what causes this offset as it does not relate to any rock avalanche parameters. A probable cause is that as explained earlier, the calculation for the synthetic horizontal distance value does not account for external factors that influence the horizontal distance travelled.

4.4 Conclusion

Galileo Scaling can be used as a rough prediction tool for determining the total horizontal distance travelled by a rock avalanche. Equation 4.2 displays a proposed equation for predicting the horizontal distance travelled by a rock avalanche based on Galileo Scaling.

$$y = B + V^{0.33} \pm E \tag{4.2}$$

Where y is the horizontal distance travelled, B is an offset term to account for the offset between the synthetic Galileo Scaling values and the real data, V is the volume of the rock avalanche and E is an error term. Further research is required to build a database containing information past the height, length, and volume of the rock avalanches which in turn, would allow for the creation of a more accurate empirical statistical tool. By including the source geology, the degree of lateral confinement, and mode of failure, the understanding of the Galileo Scaling relationship between volume and the horizontal distance travelled could be improved. This could potentially devise an accurate prediction tool that could be utilised quickly in the field to determine the potential horizontal distance a rock avalanche could travel.

Available filed data shows that the area and deposit thickness do not share a strong relationship. Area and apparent coefficient of friction expressed as Heim's Ratio do correlate, as well as volume and thickness, and volume and length of deposit. These relationships could prove

useful in potentially predicting future rock avalanche deposit geometry once smaller data sets have been established.

Chapter 5 : Conclusions and Implications

5.1 Literature Review of Rock Avalanche Models

An extensive literature review of rock avalanche behaviour current was completed to determine the present knowledge gaps of these catastrophic phenomena. These have been identified as:

1. Fragmentation – while various models have been developed to characterise rock avalanche fragmentation, these models do not agree with respect to how much energy is lost to this process or how this process occurs.
2. Entrainment – there are active discussion as to whether the entrainment of mass during rock avalanche motion is an energy sink or source term. Furthermore, it is not well understood how entrainment affects the horizontal distance travelled by a rock avalanche.
3. Environment – environmental factors are not typically quantified in rock avalanche models even though the environment, degree of lateral confinement, source geology and initial failure mechanisms have all been shown to affect the horizontal distance travelled.
4. Coefficient of Friction – The coefficient of friction of a rock avalanche is typically assumed to be constant, which likely is not the case in the field. The coefficient of friction would change depending on the degree of fragmentation of the rock avalanche, how much mass is entrained, and if the mass entrained is saturated or unsaturated.
5. Databases – existing rock avalanche databases often only include the name, height, length, volume and general location of the event, other information such as source

geology is typically not included. Consideration of other parameters such as the environment could improve the analysis of the Galileo Scaling relationship observed between the volume and the horizontal distance travelled.

5.2 Simple Physics Energy Models

The sliding physics analysis shows that a change (entrainment or deposition) in the initial mass of the rock avalanche does not affect the horizontal distance travelled. Instead, the percentage of mass either entrained or deposited during rock avalanche motion either decreased (entrainment) or increased (deposition) the horizontal distance respectively. An explanation could be found in the impact energy model, which was the only simple physics model to display a direct dependency on the initial mass of a rock avalanche. As the initial rock avalanche mass increases, the energy lost to impact also increased, this energy loss is likely transferred into fragmentation and frictional energy. Further research is required however into the impact energy model to provide a better understanding of how this model is affected by varying slope angles and to fully incorporate the model into an equation that represents the entire rock avalanche process.

The path geometry of the rock avalanche was found to not affect the total horizontal distance travelled. Two different topographic profiles were examined: i) a slope that connects to a lower, horizontal surface, and, ii) a slope that connects to a lower horizontal surface which has a hill over which the rock avalanche travels and continues on a distal horizontal slope. When calculating the horizontal distance travelled between these two topographic profiles the distance calculated was the same between the two. The geometry of the runout path does not affect the horizontal distance travelled and the importance of determining the path geometry may not be as crucial as previously considered. It is important to note that the lateral confinement of a rock

avalanche has been shown to have a direct effect on the horizontal distance travelled. Nicoletti and Sorriso-Valvo (1991) found that unconfined rock avalanches generally did not travel as far as confined rock avalanches, and that unconfined rock avalanches displayed a larger deposit area which were thinner in thickness than that of a confined rock avalanche. There should be more importance placed on the lateral constraints of a rock avalanche rather than the path geometry as it has a greater effect on the rock avalanche travel distance.

The assumption that blasting theory is an accurate representation of rock avalanche fragmentation could potentially be incorrect. Blasting theory is derived from a controlled energy blast within a rock mass that radiates equally through the mass to obtain an almost uniform grain size (Locat et al., 2006). Rock avalanches are chaotic events that display a large range in grain size from boulders to silty particles (Bartali et al., 2020). Rock avalanche fragmentation likely originates from the impact face of the rock body onto a lower slope and radiates outwards. This process would likely be a large energy sink however further research is required to determine the implications of this model.

Heim's Ratio is typically used as the apparent coefficient of friction value in rock avalanche models which is an incorrect assumption in many cases. Heim's Ratio is derived from a simple physics model which exclusively considers potential energy and frictional energy, no other energy losses are considered. If a rock avalanche model only considered energy losses to friction, then the assumption that the apparent coefficient of friction is equal to Heim's Ratio is correct. When other energy losses are considered, such as fragmentation or entrainment, the apparent coefficient of friction value is found to be lower than the Heim's Ratio value by 3 to 33%. When the other simple models (e.g. entrainment) are rearranged to solve for the apparent coefficient of friction value, they do not simplify to Heim's Ratio. Once energy loss or gains besides potential energy and frictional

energy are considered, Heim's Ratio is no longer a reasonable assumption for the apparent coefficient of friction value. A direct implication of the improper use of Heim's Ratio as the apparent coefficient value can be observed in Davies et al. (2019) model of fragmentation. These authors determined that the fragmentation energy used more energy than what was available to the system; however, the apparent coefficient of friction value for the frictional energy loss was assumed to be Heim's Ratio. By assuming Heim's Ratio as the apparent coefficient of friction value, the energy loss to friction would be overestimated and could contribute the finding that lost to fragmentation exceeds the available energy (Davies et al., 2019). Heim's Ratio may still be used as a way to display the mobility of a rock avalanche as it is a quick analysis and allows for the mobility to be compared between various rock avalanche events.

5.3 Statistical Relations

It has been noted in the literature that there appears to be a square-cube law relationship, identified by Delaney and Evans (2014) as Galileo Scaling, between volume and the depositional area, horizontal distance travelled and Heim's Ratio. A preliminary analysis was completed through the use of a rock avalanche inventory to determine the validity of these relationships. The horizontal distance, Heim's Ratio and depositional area all scale with the rock avalanche volume, with horizontal distance travelled and volume displaying the strongest correlation. The major criticism of these correlations is the amount of scatter, for a given volume the horizontal distance travelled may range from 650m to 9000m. These figures are often created using rock avalanche inventories which represent rock avalanches from variable source geology, and environments, all of which affect the horizontal distance travelled by a rock avalanche. To limit scatter smaller datasets were considered. These datasets were constrained by location, environment and source

geology and generally displayed less scatter. The large database had an R^2 value of 0.73, whereas the Legros (2002) and Chinese database had R^2 values of 0.81 and 0.84 respectively, thus showing an increase of the confidence of the data about the trendline. When considering the volume and horizontal distance travelled the Chinese database exhibited strong Galileo Scaling,

An estimate of the horizontal distance travelled by a rock avalanche can be calculated using Galileo Scaling, this new value was compared with field characteristics in the database to explore potential rock avalanche behaviour. The field data plotted an order of magnitude above the calculated horizontal distance value and did not correlate well with any rock avalanche parameters such as deposit length, thickness, area or apparent coefficient of friciont.

A simple prediction equation was created based on Galileo Scaling that could potentially account for the offset observed between the synthetic and real values.

5.4 Further Research

The fragmentation and impact energy simple models require further research. The impact energy model is limited to the current analysis as the model increases in complexity when considering a block sliding down a slope. Additional insights may be gained from understanding how this model would behave when the rock mass falls onto slope rather than a horizontal surface. As well, further data about deformation rates of various rock types are required to explore how lithology can affect the horizontal distance travelled.

Further, the energy lost when a rock mass impacts a lower slope is likely related to the energy lost to fragmentation. The current rock fragmentation models for rock avalanches differ the amount of energy consumed by these processes. The fragmentation energy model used in this

thesis is based on blasting theory. This model assumes that energy lost to the breaking of the rock mass is distributed evenly across the rock and originates from the centre of the mass and that the final material has a uniform grain size (Locat et al., 2006). Rock avalanches do not display a uniform grain size, rather the grain size often ranges from dust to blocks the size of a house (Delaney and Evans, 2014). Further, the fragmentation of a rock avalanche would originate from the side of a rock mass which collided with the lower slope and radiate outwards from this surface. These key differences change how the rock would fragment, and changes the energy consumed by this process.

Mitchell et al. (2018) and Whitall et al. (2020) have theorised that the utilizing a scaling relationship could potentially be used as a prediction tool for determining the potential travel distance of rock avalanches. This would require databases that contained more information about rock avalanches than what is currently available in the literature. Databases with greater information about rock avalanches would allow for the creation of smaller datasets that are constrained based on location, environment, source geology, the rock avalanche trigger, and other external conditions. The completion of these smaller datasets would allow for further analyses to be completed to determine how Galileo Scaling is affected by these factors and to create a potential prediction tool.

References

Aaron, J., and Hungr, O. (2015). Dynamic analysis of extraordinarily mobile rock avalanche in the Northwest Territories, Canada. *Canadian Geotechnical Journal*, *53*(6), 899-908.

Aaron, J., and McDougall, S. (2019). Rock avalanche mobility: The role of path material. *Engineering Geology, 257*, 105126. doi:10.1016/j.enngeo.2019.05.03

Abele, G. (1974). Vom Eis geformte Bergsturzlandschaften: Frage der glazialen Umgestaltung der bergsturze von Sierre, Films, Elms und vom Fernpass. *Zeitshrift fur Geomorphologie, 18*, 120-147.

Allstadt, K. (2013). Extracting source characteristics and dynamics of the August 2010 Mount Meager landslide from broadband seismograms. *Journal of Geophysical Research: Earth Surface, 118*, 1472-1490.

Bagnold, R. (1954). Experiments on a gravity-free dispersion of large solid spheres in a Newtonian fluid under shear. *Proceedings of the Royal Society A, 225*(1160), 49-63.

Bai, X., Jian, J., He, S., and Liu, W. (2018). Dynamic process of the massive Xinmo landslide, Sichuan (China), from joint seismic signal and morphodynamic analysis. *Bulletin of Engineering Geology and the Environment*, *78*, 3269-3279.

Bartali, R., Rodriquez Linan, G., Torres-Cisneros, L., Perez-Angel, G., and Nahmad-Molinari, Y. (2020). Runout transition and clustering instability observed in binary-mixture avalanche deposits. *Granular Matter, 22*(30). doi:10.1007/s10035-019-0989-0

Bartelt, P., Salm, B., and Gruber, U. (1999). Calculating dense-snow avalanche runout using a Voellmy-fluid model with active/passive longitudinal straining. *Journal of Glaciology, 45*(150), 242-254.

Barth, N. C. (2014). The Cascade rock avalanche: implication of a very large Alpine Fault-triggered failure, New Zealand. *Landslides, 11*(3), 327-341.

Benko, B., and Stead, D. (1998). The Frank Slide: a reexamination of the failure mechanism. *Canadian Geotechnical Journal, 35*(2), 299-311.

Bessette-Kirton, E. K., Coe, J. A., and Zhou, W. (2018). Using Stereo Satellite Imagery to Account for Ablation, Entrainment, and Compaction in Volume Calculations for Rock Avalanches on Glaciers: Application to the 2016 Lamplugh Rock Avalanche in Glacier Bay National Park, Alaska. *Journal of Geophysical Research: Earth Surface, 123*(4), 622-641.

Blais-Stevens, A., Geertsema, M., Schwab, J., and van ASCH, T. W. (2015). Complex Landslide Triggered in an Eocene Volcanic-Volcaniclastic Succession along Sutherland River, British Columbia, Canada. *Environmental and Engineering Geoscience, 21*(1), 35-45.

Bowman, E. T., Take, W. A., Rait, K. L., and Hann, C. (2012). Physical models of rock avalanche spreading behaviour with dynamic fragmentation. *Canadian Geotechnical Journal, 49*(4), 460-476.

Brideau, M. A., McDougall, S., Stead, D., Evans, S. G., and Turner, K. (2012). Three-dimensional distinct element modelling and dynamic runout analysis of a landslide in gneissic rock,

British Columbia, Canada. *Bulletin of Engineering Geology and Environment, 71*, 467-486.

Brideau, M.-A., and Roberts, N. J. (2015). Mass Movement in Bedrock. In *Landslide Hazards, Risks and Disasters* (pp. 43-90). Elsevier Inc.

Brideau, M., Stead, D., Kinakin, D., and Fecova, K. (2005). Influence of tectonic structures on the Hope Slide, British Columbia, Canada. *Engineering Geology, 80*, 242-259.

Brideau, M. A., Stead, D., Lipovsky, P., Jaboyedoff, M., Hopkinson, C., Demuth, M., Barlow, J., Evans, S., and Delaney, K., (2010). Preliminary description and slope stability analyses of the 2008 Little Salmon Lake and 2007 Mt. Steele landslides, Yukon. In: Yukon Exploration and Geology 2009, K.E. MacFarlane, L.H. Weston and L.R, Blackburn (eds.). Yukon Geological Survay, 119-133.

Brodsky, E., Gordeev, E., and Kanamori, H. (2003). Landslide basal friction as measured by seismic waves. *Geophysical Research Letters, 30*(24), 2236.

Cagnoli, B., and Piersanti, A. (2015). Grain size and flow volume effects on granular flow mobility in numerical simulations: 3-D discrete element modeling of flows of angular rock fragments. *Journal of Geophysical Research: Solid Earth, 120*(4), 2350-2366.

Cagnoli, B., and Piersanti, A. (2017). Combined effects of grain size, flow volume and channel width on geophysical flow mobility: Three-dimensional discrete element modeling of dry and dense flows of angular rock fragments. *Solid Earth, 8*(1), 177-188.

Campbell, C. (1989). Self-Lubrication for Long Runout Landslides. *The Journal of Geology, 97*(6), 653-665.

Campbell, C. (1990). Rapid Granular Flows. *Annual Review of Fluid Mechanics, 22*, 57-92.

Campbell, C., Cleary, P., and Hopkins, M. (1995). Large-scale landslide simulations: Global deformation, velocities and basal friction. *Journal of Geophysical Research, 100*(5), 8267-8283.

Charriere, M., Humair, F., Froese, C., Jaboyedoff, M., Pedrazzini, A., and Longchamp, C. (2015). From the source area to the deposit: Collapse, fragmentation and propagation of the Frank Slide. *GSA Bulletin, 128*, 332-352.

Clague, J. J., and Souther, J. G. (1982). The Dusty Creek landslide on Mount Cayley, British Columbia. *Canadian Journal of Earth Sciences, 19*(3), 524-539.

Coe, J., Baum, R., Allstadt, K., Kochevar, B., Schmitt, R., Morgan, M., and Kean, J. (2016). Rock-avalanche dynamics revealed by large-scale field mapping and seismic signals at a highly mobile avalanche in the West Salt Creek valley, western Colorado. *Geosphere, 12*(2), 607-631.

Collins, G., and Melosh, H. (2003). Acoustic fluidization of the extraordinary mobility of sturzstroms. *Journal of Geophysical Research, 108*(B10), 1-14.

Collins, B., and Reid, M. (2019). Enhanced landslide mobility by basal liquefaction: The 2014 State Route 530 (Oso), Washington, Landslide. *Geological Society of America Bulletin, 132*(3/4), 451-476.

Corominas, J. (1996). The angle of reach as a mobility index for small and large landslides. *Canadian Geotechnical Journal, 33*(2), 260-271.

Crosta, G., Chen, H., and Lee, C. (2004). Replay of the 1987 Val Pola Landslide, Italian Alps. *Geomorphology, 33*(2), 127-146.

Crosta, G., De Blasio, F., De Caro, M., Volpi, G., Imposimato, S., and Rodderman, D. (2017). Modes of propagation and deposition of granular flows onto an erodible substrate: Experimental, analytical, and numerical study. *Landslides, 14*(1), 47-68.

Crosta, G., Frattini, P., and Fusi, N. (2007). Fragmentation in the Val Pola rock avalanche, Italian Alps. *Journal of Geophysical Research: Earth Surface, 112*. doi: 10.1029/2005JF000455

Crosta, G., Hermanns, R., Dehls, J., Lari, S., and Sepulveda, S. (2017). Rock avalanches clusters along the northern Chile coastal scarp. *Geomorphology, 289*, 27-43.

Crosta, G., Imposimato, S., and Roddeman, D. (2009). Numerical modelling of entrainment/deposition in rock and debris-avalanches. *Engineering Geology, 109*(1-2), 135-145.

Cruden, D., M. (1976). Major rock slides in the Rockies. *Canadian Geotechnical Journal, 13*(1), 8-20.

Cruden, D., M, (1980). A Large Landslide on Mars: Discussion and Reply. *Geological Society of America Bulletin, 91*, 63-64.

Cruden, D., M. (1982). The Brazeau Lake Slide, Jasper National Park. *Canadian Journal of Earth Science, 19*, 975-981.

Cruden, D., M., and Eaton, T. M. (1987). Reconnaissance of rockslide hazards in Kananaskis Country, Alberta. *Canadian Geotechnical Journal, 24*(3), 414-429.

Dade, W. B., and Huppert, H. E. (1998). Long-runout rockfalls. *Geology 26*(9)*, 26*, 803-806.

Dai, F., Tu, X., Xu, C., Gong, Q., and Yao, X. (2011). Rock avalanches triggered by oblique thrusting during the 12 May 2008 Ms 8.0 Wenchuan earthquake, China. *Geomorphology, 132*(3-4), 300-318.

Davies, T. (1981). Spreading of Rock Avalanche Debris by Mechanical Fluidization. *Rock Mechanics, 15*, 9-24.

Davies, T., and McSaveney, M. (1999). Runout of dry granular avalanches. *Canadian Geotechnical Journal, 36*(2), 313-320.

Davies, T., and McSaveney, M. (2002). Dynamic simulation of the motion of fragmenting rock avalanches. *Canadian Geotechnical Journal, 39*(40), 789-798.

Davies, T., and McSaveney, M. J. (2009). The role of rock fragmentation in the motion of large landslides. *Engineering Geology, 109*(1-2), 67-79.

Davies, T., McSaveney, M., and Boulton, C. (2012). Elastic strain energy release from fragmenting grains: Effects on fault rupture. *Journal of Structural Geology, 38*, 265-277.

Davies, T., MvSaveney, M., and Deganutti, A. (2007). Dynamic rock fragmentation causes low rock-on-rock friction. In *Proceedings of the 1st Canada-US Rock Mechanics Symposium - Rock Mechanics Meeting Society's Challenges and Demands.* CRC Press.

Davies, T., McSaveney, M., and Hodgson, K. (1999). A fragmentation-spreading model for long-runout rock avalanches. *Canadian Geotechnical Journal, 36*(6), 1096-1110.

Davies, T., Reznichenko, N., and McSaveney, M. (2019). Energy budget for a rock avalanche: fate of fracture-surface energy. *Landslides, 17*(4), 1-11

De Blasio, V. (2007). Production of frictional heat and hot vapour in a model of self-lubricating landslides. *Rock Mechanics and Rock Engineering, 41*(1), 219-226.

De Blasio, F. (2009). Rheology of a wet, fragmenting granular flow and the riddle of the anomalous friction of large rock avalanches. *Granular Matter, 11*(3), 179-184.

De Blasio, F. (2011). *Introduction to the physics of landslides.* Heidelberg: Springer.

De Blasio, F. (2014). Friction and dynamics of rock avalanches travelling on glaciers. *Geomorphology, 36*(6), 88-98.

De Blasio, F., and Crosta, G. (2014). Simple physical model for the fragmentation of rock avalanches. *Acta Mechanica, 225*, 243-252.

De Blasio, F., and Crosta, G. (2015). Fragmentation and boosting of rock falls and rock avalanches. *Geophysical Research Letters, 42*(20), 8463-8470.

De Blasio, F., Dattola, G., and Crosta, G. (2018). Extremely Energetic Rockfalls. *Journal of Geophysical Research: Earth Surface, 123*. doi: 10.1029/2017JF004327

DeGiuli, E., and Wyart, M. (2017). Friction law and hysteresis in granular materials. *Proceedings of the National Academy of Sciences of America, 114*(35), 9284-9289.

Delaney, K. B., and Evans, S. G. (2014). The 1997 Mount Munday landslide (British Columbia) and the behaviour of rock avalanches on glacier surfaces. *Landslides, 11*(6), 1019-1036.

Delannay, R., Valance, A., Mangeney, A., Roche, O., and Richard, P. (2017). Granular and particle-laden flows: from laboratory experiments to field observations. *Journal of Physics D: Applied Physics, 50*(5). doi: 10.1088/1361-6463/50/5/053001

Deline, P., Hewitt, K., Reznichenko, N., and Shugar, D. (2015). Rock Avalanches onto Glaciers. In J. Shroder (Ed.), *Using Stereo Satellite Imagery to Account for Ablation, Entrainment, and Compaction in Volume Calculations for Rock Avalanches on Glaciers: Landslide Hazards, Risks and Disasters* (pp. 263-319).

Deparis, J., Jongmans, D., Cotton, F., Baillet, L., Thouvenot, F., and Hantz, D. (2008). Analysis of rock-fall and rock-fall avalanche seismograms in the French Alps. *Bulletin of the Seismological Society of America, 98*(4), 1781-1796.

Dong, J. J., Yang, C. M., Yu, W. L., Lee, C. T., Miyamoto, Y., and Shimamoto, T. (2013). Velocity displacement dependent friction coefficient and the kinematics of giant landslides. In K. Ugai, H. Yagi, and A. Wakai (Eds.), *Earthquake-induced landslides* (395-401). Springer.

Dufresne, A., Bosmeier, A., and Prager, C. (2016)a. Sedimentology of rock avalanche deposits - Case study and review. *Earth-Science Reviews, 163*, 234-259.

Dufresne, A., and Dunning, S. (2017). Process dependence of grain size distributions in rock avalanche deposits. *Landslides, 14*, 1555-1563.

Dufresne, A., and Geertsema, M. (2020). Rock slide-debris avalanches: flow transformation and hummock formation, examples from British Columbia. *Landslides, 17*, 15-32.

Dufresne, A., Geertsema, M., Shugar, D., Koppes, M., Higman, B., Haeussler, P., Stark, C., Venditti, J. G., Bonno, D., Larsen, C., Gulick, S. P. S., McCall, N., Walton. M., Loso, M.G., and Willis, M. (2018). Sedimentology and geomorphology of a large tsunamigenic landslide. Taan Fiord, Alaska. *Sedimentary Geology, 364*, 302-318.

Dufresne, A., Prager, C., and Bosmeier, A. (2016)b. Insights into rock avalanche emplacement processes from detailed morpho-lithological studies of the Tschirgant deposit (Tyrol, Austria). *Earth Surface Processes and Landforms, 41*, 587-602

Dufresne, A., Wolken, G., Hibert, C., Bessette-Kirton, E., Coe, J., Geertsema, M., and Erkström, G. (2019). The 2016 Lamplugh rock avalanche, Alaska: deposit structures and emplacement dynamics. *Landslides 16* (3), 2301-2319.

Dunning, S. (2006). The grain-size distribution of rock-avalanche deposits in valley-confined settings. *Italian Journal of Engineering Geology and Environment, 1*, 117-121.

Edwards, L. (2003). *Physics*. Toronto, ON: McGraw-Hill Ryerson.

Eisbacher, G. (1977). Rockslides in the Mackenzie Mountains, District of Mackenzie. *Report of Activities, Part A, Geological Survey of Canada*, 235-242.

Eisbacher, G. H. (1979). Cliff collapse and rock avalanches (Sturzstroms) in the Mackenzie Mountains, north western Canada. *Canadian Geotechnical Journal , 17*, 309-334.

Erkström, G., and Stark, C. (2013). Simple scaling of catastrophic landslide dynamics. *Science, 339*(6126), 1416-1419.

Estep, J., and Dufek, J. (2013). Discrete element simulations of bed force anomalies due to force chains in dense granular flows. *Journal of Volcanology and Geothermal Research, 254*, 108-117.

Evans, S., and Clague, J. (1988). Catastrophic rock avalanches in glacial environments. *Landslides-Glissements de Terrains: Proceedings, 5th International Symposium of Landslides, Lausanne*, 2, 1153-1159.

Evans, S., and Delaney, K. (2015). Chapter 16 - Catastrophic Mass Flows in the Mountain Glacial Environment. *In J. Shroder, W. Haeberli, and C. Whiteman, Snow and Ice-Related Hazards, Risks, and Disasters* (pp. 563-606). Elsevier.

Evans, S. G., Hungr, O., and Clague, J. J. (2001). Dynamics of the 1984 rock avalanche and associated debris flow on Mount Cayley, British Columbia, Canada; implications for landslide hazard assessment on dissected volcanoes. *Engineering Geology*, *61*(1), 29-51.

Evans, S., Tutubalina, O., and Drobyshev, S. (2009). Catastrophic detachment and high-velocity long-runout flow of Kolka Glacier, Caucasus Mountains, Russia in 2002. *Geomorphology, 105*(3-4), 314-321.

Fan, X., Xu, Q., Scaringi, G., Dai, L., Li, W., Dong, X., Zhu, X., Pei, X., Dai, K., and Havenith, H. (2017). Failure mechanism and kinematics of the deadly June 24th 2017 Xinmo landslide, Maoxian, Sichuan, China. *Landslides, 14*(6), 2129-2146.

Fan, S., Xu, Q., Scaringi, G., Zheng, G., Huang, R., Dai, L., and Ju, Y. (2019). The "long" runout rock avalanche in Pusa, China, on August 28, 2017: a preliminary report. *Landslides, 16,* 139-154.

Farin, M., Mangeney, A., and Roche, O. (2014). Fundamental changes of granular flow dynamics, deposition, and erosion processes at high slope angles: insights from laboratory experiments. *Journal of Geophysical Research: Earth Surface, 119*(3), 504-532.

Favreau, P., Mangeney, A., Lucas, A., Crosta, G., and Bouchut, F. (2010). Numerical modeling of landquakes. *Geophysical Research Letters*, *37*(15). doi: 10.1029/2010GL043512

Francioni, M., Calamita, F., Coggan, J., De Nardis, A., Eyre, M., Miccadei, E., Piacentini, T., Stead, D., and Sciarra, N. (2019). A Multi-Disciplinary Approach to the Study of Large Rock Avalanches Combining Remote Sensing, GIS and Field Surveys: The Case of the Scanno Landslide, Italy. *Remote Sensing, 11*(13). doi: 10.3390/rs11131570

Fuchs, F., Lenhardt, W., and Bokelmann, G. (2018). Seismic detection of rockslides at regional scale: examples from the Eastern Alps and feasibility of kurtosis-based event location. *Earth Surface Dynamics 6*, 955-970.

Galileo, G. (1638). *Discourses and Mathematical Demonstrations Relating to Two New Sciences.* Elzevir, L.

Ge, Y., Tang, H., Eldin, M., Chen, H., Zhong, P., Zhang, L., and Fang, K. (2019). Deposit characteristics of the Jiweishan rapid long runout landslide based on field investigation and numerical modeling. *Bulletin of Engineering Geology and the Environment*, *74,* 4383-4396.

Geertsema, M., Clague, J., Schwab, J., and Evans, S. (2005). An overview of recent large catastrophic landslides in northern British Columbia, Canada. *Engineering Geology, 83*(1-3), 120-143.

Geertsema, M., Hungr, O., Schwab, J., and Evans, S. (2006). A large rockslide - Debris avalanche in cohesive soil at Pink Mountain, northeastern British Columbia, Canada. *Engineering Geology, 83*(1-3), 64-75.

Goguel, J. (1978). Chapter 20 - Scale-Dependent Rockslide Mechanisms, with Emphasis on the Role of Pore Fluid Vaporization. In B. Voight (Ed.), *Developments in Geotechnical Engineering* (Vol. 14, pp. 693-705). Elsevier.

Google earth V 7.3.3.7786. (n.d.)a. Bonnet Plume, Mackenzie Mountains, Yukon, Canada. 64°22'65" N, 132°00'50" W, Eye alt 6.52km. Image Landstat, Copernicus. google.com/earth [February 16, 2021].

Google earth V 7.3.3.7786. (n.d.)b. Damocles Slide, Mackenzie Mountains, Northwest Territories, Canada. 64°17'56" N, 130°59'47" W, Eye alt 6.78km. Image Landstat, Copernicus. google.com/earth [February 16, 2021].

Google earth V 7.3.3.7786. (n.d.)c. Rockslide Pass, Mackenzie Mountains, Northwest Territories, Canada. 63°20'44" N, 127°41'50" W, Eye alt 7.3km. Image Landstat, Copernicus. google.com/earth [February 16, 2021].

Google earth V 7.3.3.7786. (n.d.)d. Turtle Mountain, Alberta, Canada. 49°35'10" N, 114°23'52" W, Eye alt 5.56km. Image CNES, Airbus. google.com/earth [February 14, 2021].

Goren, L., and Aharonov, E. (2007). Long runout landslides: The role of frictional heating and hydraulic diffusivity. *Geophysical Research Letters, 34*(7). doi: 10.1029/2006GL028895

Gudmundsson, A. (2011). *Rock Fractures in Geological Processes.* Cambridge University Press.

Guthrie, R., Friele, P., Allstadt, K., Roberts, N., Evans, S., Delaney, K., Roche, D., Clague, J. J., and Jakob, M. (2012). The 6 August 2010 Mount Meager rock slide–debris flow, Coast Mountains, British Columbia: Characteristics, dynamics, and implications for hazard and risk assessment. *Natural Hazards and Earth System Sciences, 12*, 1277-1294.

Habib, P. (1975). Production of gaseous pore pressure during rock slides. *Rock Mechanics, 7*(4), 193-197.

Hanes, D. M., and Inman, D. L. (1985). Observations of rapidly flowing granular-fluid materials. *Journal of Fluid Mechanics, 150*, 357-380.

Haug, O., Rosenau, M., Leever, K., and Oncken, O. (2016). On the energy budgets of fragmenting rockfalls and rockslides: Insights from experiments. *Journal of Geophysical Research: Earth Surface, 121*, 1310-1327.

Haug, O., Rosenau, M., Rudolf, M., Leever, K., and Oncken, O. (2020). Variations in runout of rock avalanches controlled by fragmentation, not basal friction. *EarthArXiv*. doi: 10.31223/osf.io/2ntdc

Haung, C., Li, Y., Yi, S., Liu, K., and Wu, C. (2018). Characteristics and failure mechanism of an ancient earthquake induced landslide with an extremely wide distribution area. *Journal of Moutain Science, 15*, 380-393.

Heim, A. (1882). Ueber den Bergsturz von Elm. *Z. Dtsch. Geol. Ges*, 435-438.

Heim, A. (1932). Landslides and Human Lives (N. Skermer, Trans.) BiTech Publisher

Hencher, S. R., Lee, S. G., Carter, T. G., and Richards, L. R. (2011). Sheeting joints: characterisation, shear strength and engineering. *Rock Mechanics and Rock Engineering, 44*, 1-22.

Hermanns, R., and Longva, O. (2012). Rapid rock-slope failures. In J. J. Clague, and D. Stead (Eds.), *Landslides: Types, Mechanisms and Modeling* (pp. 59-70). Cambridge: Cambridge University Press.

Hermanns, R. L., Oppikofer, T., and Blikra, L. H. (2012). Recommended hazard and risk classification system for large unstable slopes in Norway. *Trondheim: Geological Survey of Norway, 49.*

Hermanns, R. L., and Strecker, M. R. (1999). Structural and lithological controls on large Quaternary rock avalanches (struzstroms) in arid northwestern Argentina. *Geological Society of America Bulletin, 111*(6), 934-948.

Hewitt, K., Clague, J., and Orwin, J. (2008). Legacies of catastrophic rock slope failures in mountain landscapes. *Earth Science Review, 87*, 1-38.

Hibert, C., Erkström, G., and Stark, C. (2017). The relationship between bulk-mass momentum and short-period seismic radiation in catastrophic landslides. *Journal of Geophysical Research: Earth Surface, 122*, 1201-1215.

Hoek, E. (1999). Putting numbers to geology - an engineer's viewpoint. *Quaternary Journal of Engineering Geology, 32*, 1-19.

Hoek, E., and Brown, E. T. (1997). Practical estimates of rock mass strength. *International Journal of Rock Mechanics and Mining Science, 34*, 1164-1186.

Howard, K. E. (1973). Avalanche mode of motion, implications from lunar examples. *Science, 180(*4090), 1052-1055.

Hsu, K. (1975). Catastrophic Debris Streams (Sturzstroms) Generated by Rockfalls. *Geological Society of America Bulletin, 86*, 129-140.

Hu, Y., Chen, M., and Zhou, J. (2019). Numerical simulation of the entrainment effect during mass movement in high-speed debris avalanches. *Arabian Journal of Geosciences, 12*(14). doi: 10.1007/s12517-018-4199-6

Huang, D., Li, Y., Song, Y., Xu, Q., and Pei, X. (2019). Insights into the catastrophic Xinmo rock avalanche in Maoxian county, China: Combined effects of historical earthquakes and landslide amplification. *Engineering Geology, 258*(3). doi: 10.1016/j.enggeo.2019.105158

Hungr, O. (1990). Mobility of rock avalanches. *National Research Institute for Earth Science and Disaster Resilience, 46*, 11-20.

Hungr, O. (1995). A model for the runout analysis of rapid flow slides, debris flows, and avalanches. *Canadian Geotechnical Journal, 32*, 610-623.

Hungr, O., Dawson, R., Kent, A., Campbell, D., and Morgenstern, N. (2002). Rapid flow slides of coal-mine waste in British Columbia, Canada. In S. Evans, and J. DeGraff (Eds.), *Catastrophic Landslides, Geological Society of America* (pp. 191-208). Boulder: The Geological Society of America, Inc.

Hungr, O., and Evans, S. (1989). Engineering evaluation of fragmental rockfall hazards. *Proceedings of the 5th International Symposium on Landslides in Lausanne.*

Hungr, O., and Evans, S. (1996). Rock avalanche runout prediction using a dynamic model. *Landslides: International Symposium on Landslides,* 233-238.

Hungr, O., and Evans, S. (2004). Entrainment of debris in rock avalanches: an analysis of a long run-out mechanism. *GSA Bulletin, 116*(9/10), 1240-1252.

Hungr, O., Evans, S. G., Bovis, M. J., and Hutchinson, J. N. (2001). A review of the classification of landslides of the flow type. *Environmental Engineering Geoscience, VII*, 221-238.

Hungr, O., Leroueil, S., and Picarelli, L. (2014). The Varnes classification of landslide types, an update. *Landslides, 11*(2), 167-194.

Hungr, O., and Morgenstern, N. (1984). Experiments on the flow behaviour of granular materials at high velocity in an open channel. *Geotechnique, 34*, 405-413.

Huscroft, C. A., Lipovsky, P. S., and Bond, J. D. (2004). A regional characterization of landslides in the Alaska Highway corridor Yukon. *Yukon Geological Survey*.

Hutter, K., Koch, T., Pluss, C., and Savage, S. (1995). The dynamics of avalanches of granular materials from initiation to runout. Part II. Experiments. *Acta Mechanica, 109*, 127-165.

Imre, B., Laue, J., and Springman, S. (2010). Fractal fragmentation of rocks within sturzstroms: insight derived from physical experiments within the ETH geotechnical drum centrifuge. *Granular Matter, 12*, 267-285.

ISRM. (1981). Basic geotechnical description of rock masses. *International Journal of Rock Mechanics and Mining Sciences, 18*, 87-110.

Iverson, R. (2015). Scaling and design of landslide and debris-flow experiments. *Geomorphology, 244*, 9-20.

Jackson, L. E., and Isobe, J. S. (1990). Rock avalanches in the Pelly Mountains, Yukon Territory. *Geological Survey of Canada Paper*, 263-269.

Jaeger, J. C., Cook, N. G., and Zimmerman, R. W. (2007). *Fundamentals of Rock Mechanics, Fourth ed.* Blackwell Publishing.

Je, L., Zhixian, C., Yifei, C., and Bothwick, A. (2020). Barrier lake formation due to landslide impacting a river: A numerical study using a double layer-averaged two-phase flow model. *Applied Mathematical Modelling, 80*, 574-601.

Jelinek, J., and Zacek, V. (2018). Assessment of a catastrophic rock avalanche in the West Mongolian Altai Mountains. *Engineering Geology, 223*, 38-47.

Jibson, R., and Keefer, D. (1994). Analysis of the seismic origin of landslides: examples from the New Madrid seismic zone. *Geological Society of America Bulletin, 105*, 521-536.

Johnson, B. (1978). Blackhawk Landslide, California, U. S. A. In B. Voight (Ed.), *Rockslides and Avalanches* (pp. 481-504). Amsterdam, Oxford, New York: Elsevier.

Johnson, B., and Campbell, C. (2017). Drop height and volume control the mobility of long-runout landslides on the Earth and Mars. *Geophysical Research Letters, 44*(24), 12091-12097.

Johnson, B., Campbell, C., and Melosh, H. (2016). The reduction of friction in long runout landslides as an emergent phenomenon. *Journal of Geophysical Research: Earth Science, 121*, 881-889.

Kang, C., Chan, D., Su, F., and Cui, P. (2017). Runout and entrainment analysis of an extremely large rock avalanche – a case study of Yigong, Tibet, China. *Landslides, 14*, 123-139.

Keefer, D. (1984). Landslides caused by earthquakes. *Geological Society of America Bulletin, 95*, 406-421.

Kelfoun, K., and Druitt, T. (2005). Numerical modeling of the emplacement of Socompa rock avalanche, Chile. *Journal of Geophysical Research, 110*(B12). doi: 10.1029/2005JB003758

Kent, P. (1966). The Transport Mechanism in Catastrophic Rock Falls. *The Journal of Geology, 74*(1), 79-83.

Kesseler, M., Heller, V., and Turnbull, B. (2020). Grain Reynolds Number Scale Effects in Dry Granular Slides. *Journal of Geophysical Research: Earth Surface, 125*(1). doi: 10.1029/2019JF005347

Lato, M., Anderson, S., and Porter, M. (2019). Reducing Landslide Risk Using Airborne Lidar Scanning Data. *Journal of Geotechnical and Geoenvironmental Engineering, 145*(9). doi: 10.1061/(ASCE)GT.1943-5606.0002073

Lee, J., Davies, T., and Bell, D. (2009). Successive Holocene rock avalanches at Lake Coleridge, Canterbury, New Zealand. *Landslides, 6*(287). doi: 10.1007/s10346-009-0163-6

Legros, F. (2002). The mobility of long-runout landslides. *Engineering Geology, 63*, 301-331.

Li, W., Li, H., Dai, F., and Lee, L. (2012). Discrete element modeling of a rainfall-induced flowslide. *Engineering Geology, 149-150*, 22-34.

Lin, Q., Cheng, Q., Li, K., Xie, Y., and Wang, Y. (2020). Contributions of Rock Mass Structure to the Emplacement of Fragmenting Rockfalls and Rockslides: Insights from Laboratory Experiments. *Journal of Geophysical Research: Solid Earth, 125*(4). doi: 10.1029/2019BJ019296

Linares-Guerrero, E., Goujon, C., and Zenit, R. (2007). Increased mobility of bidisperse granular avalanches. *Journal of Fluid Mechanics, 593*, 475-504.

Lie, W., He, S., Li, X., and Xu, Q. (2016). Two dimensional landslide dynamic simulation based on a velocity-weakening friction law. *Landslides, 13*(5), 957-965.

Liu, W., Wang, D., Zhou, J., and He, S. (2019). Simulation the Xinmo landslide runout considering entrainment effect. *Environmental Earth Sciences, 78*(585). doi: 10.1007/s12665-019-8596-2

Locat, P., Couture, R., Leroueil, S., Locat, J., and Jaboyedoff, M. (2006). Fragmentation energy in rock avalanches. *Canadian Geotechnical Journal, 43*(8), 830-851.

Lucas, A., Mangeney, A., and Ampuero, J. (2014). Frictional velocity-weakening in landslides on Earth and on other planetary bodies. *Nature Communications, 5*(3417). doi: 10.1038/ncomms4417

Luo, J., Xu, Z., Ren, Z., Wang, K., Yang, K., Tang, Y., Gao, H., and Tian, L. (2019). Rock avalanche-debris geometry and implications for rock-avalanche genesis. *Geomorphology, 334*(1), 60-75.

Masson, D. G., Le Bas, T. P., Grevemeyer, I., and Weinrebe, W. (2008). Flank collapse and large-scale landsliding in the Cape Verde Islands, off West Africa. *Geochemistry, Geophysics, Geosystems, 9*(7). doi: 10.1029/2008GC001983

Matheson, D. S., and Thomson, S. (1973). Geological implications of valley rebound. *Canadain Journal of Earth Sciences, 10*, 961-978.

McDougall, S. (2016). 2014 Canadian Geotechnical Colloquium: Landslide runout analysis — current practice and challenges. *Canadian Geotechnical Journal, 54*(5), 605-620.

McEwen, A. S. (1989). Mobility of large rock avalanches: evidence from Valles Marinerias, Mars. *Geology, 17*, 1111-1114.

McKinnon, M., Hungr, O., and McDougall, S. (2008). Dynamic analyses of Canadian Landslides. *Proceedings of the 4th Canadian Conference on Geohazards*.

McSaveney, M. J. (1978). Sherman Glacier rock avalanche, Alaska, U.S.A. In B. Voight (Ed.), *Rockslides and avalanches* (Vol. 1, pp. 197-258). Amsterdam: Elsevier.

McSaveney, M., and Davies, T. (2007). Rockslides and their motion. In K. Sassa, H. Fukuoka, F. Wang, and G. Wang (Eds.), *Progress in Landslide Science* (pp. 113-134). Germany: Springer.

Mead, S., and Cleary, P. (2015). Validation of DEM prediction for granular avalanches on irregular terrain. *Journal of Geophysical Research: Earth Surface, 120*(9), 1724-1742.

Melosh, H. (1979). Acoustic Fluidization: A New Geologic Process? *Journal of Geophysical Research, 84*(13), 7513-7520.

Melosh, H. (1982). A simple mechanical model of Valhalla Basin, Callisto. *Journal of Geophysical Research, Solid Earth, 87*, 1880-1890.

Mergili, M., Jaboyedoff, M., Pullarello, J., and Pudasaini, S. (2020). Back calculation of the 2017 Piz Cengalo-Bondo landslide cascade with r.avaflow: what we can do and what we can learn. *Natural Hazards and Earth System Sciences, 20*, 505-520.

Mitchell, A., McDougall, S., Nolde, N., Brideau, M. A., Whittall, J., and Aaron, J. B. (2019). Rock avalanche runout prediction using stochastic analysis of a regional dataset. *Landslides, 17*, 777-792.

Mitchell, A., McDougall, Whittall, J., Brideau, M., and McClarty, D. (2018). New empirical-statistical tools for the analysis of rock avalanche runout. *Geohazards 7*.

Mollon, G., Richefeu, V., Villard, P., and Daudon, D. (2012). Numerical simulation of rock avalanches: Influence of a local dissipative contact model on the collective behaviour of granular flows. *Journal of Geophysical Research: Earth Surface, 117*(F2). doi: 10.1029/2011JF002202

Moore, J., Pankow, K., Ford, S., Koper, K., Hale, J., Aaron, J., and Larsen, C. (2017). Dynamics of the Bingham Canyon rock avalanches (Utah, USA) resolved from topographic, seismic, and infrasound data. *Journal of Geophysical Research: Earth Surface, 122*(3), 615-640.

Moretti, L., Allstadt, K., Manageney, A., Capdeville, Y., Stutzmann, E., and Bouchut, F. (2015). Numerical modeling of the Mount Meager landslide constrained by its force history derived from seismic data. *Journal of Geophysical Research: Solid Earth, 120*(4), 2579-2599.

Moretti, L., Mangeney, A., Capdeville, Y., Stutzmann, E., Huggel, C., Schneider, D., and Bouchut, F. (2012). Numerical modeling of the Mount Stellar landslide flow history and of the generate long period seismic waves. *Geophysical Research Letters, 39*(16). doi: 10.1029/2012GL052511

Moretti, L., Mangeney, A., Walter, F., Capdeville, Y., Bodin, T., Stutzmann, E., and Le Friant, A. (2020). Constraining landslide characteristics with Bayesian inversion of filed and seismic data. *Geophysical Journal International, 221*(2), 1341-1348.

Nichols, T. C. (1980). Rebound, its nature and effect on engineering works. *Quarternary Journal of Engineering Geology and Hydrogeology, 13*, 133-152.

Nicoletti, P., and Sorriso-Valvo, M. (1991). Geomorphic controls of the shape and mobility of rock avalanches. *Geological Society of America Bulletin, 103*, 1365-1373.

Okura, Y., Kitahara, H., Sammori, T., and Kawanami, A. (2000). The effects of rockfall volume on runout distance. *Engineering Geology, 58*, 109-124.

Orwin, J. F., Clague, J. J., and Gerath, R. F. (2004). The Cheam rock avalanche, Fraser Valley, British Columbia, Canada. *Landslides 1*(4), 289-298.

Paguican, E., van Wyk de Vries, B., and Lagmay, A. (2012). Hummocks: how they form and how they evolve in rockslide-debris avalanches. *Landslides, 11*, 67-80.

Parez, S., and Aharonov, E. (2015). Long runout landslides: a solution from granular mechanics. *Frontiers in Physics, 3*(80), 1-10.

Penna, I., Albellan, A., Humair, F., Jaboyedoff, M., Daic, S., and Fauque, L. (2016). The role of tectonic deformation on rock avalanche occurrence in the. *Geomorphology, 289*, 18-26.

Perinotto, H., Schneider, J.-L., Bachelery, P., Le Bourdonnec, F.-X., Famin, V., and Michon, L. (2015). The extreme mobility of debris avalanches: A new model of transport mechanism. *Journal of Geophysical Research: Solid Earth, 120*, 8110-8119.

Phillips, J., Hogg, J., Kerswell, R., and Thomas, N. (2006). Enhanced mobility of granular mixtures of fine and coarse particles. *Earth and Planetary Science Letters, 246*(3/4), 466-480.

Pirulli, M., Preh, A., Roth, W., Scavia, C., and Poisel, R. (2003). Rock avalanche run out prediction: combined application of two numerical methods. *Technology Roadmap for Rock Mechanics. South African Institute of Mining and Metallurgy*.

Pollet, N., Cojean, R., Couture, R., and Schneider, J. (2011). A slab on slab model for the Flims rockslide (Swiss Alps). *Canadian Geotechnical Journal, 42*(2), 587-600.

Preh, A. (2020). Falls originating from rock slopes – runout evaluation using numerical models. *Geomechanics and Tunnelling, 13*(1), 59-73.

Preuth, T., Bartelt, P., Korup, O., and McArdell, B. (2010). A random kinetic energy model for rock avalanches: Eight case studies. *Journal of Geophysical Research: Earth Surface, 115*(F3). doi: 10.1029/2009JF001640

Pollard, D. D., and Aydin, A. (1988). Progress in understanding jointing over the past century. *Geological Society of America Bulletin, 100*, 1181-1204.

Pudasaini, S., and Krautblatter, M. (2014). A two-phase mechanical model for rock-ice avalanches. *Journal of Geophysical Research: Earth Surface, 119*, 2272-2290.

Rait, K., and Bowman, E. (2016). Influences of strain rate and shear rate on the propagation of large scale. Landslides and Engineered Slopes. Experience, Theory and Practice Proceedings of the 12th International Symposium on Landslides. *12th International Symposium on Landslides.* Napoli.

Ramsay, J. G. (1967). Folding and Fracturing of Rocks. McGraw-Hill.

Ren, Z., Wang, K., Yang, K., Zhou, Z., Yang, Y., Tian, L., and Xu, Z. (2018). The grain size distribution and composition of the Touzhai rock avalanche deposit in Yunnan, China. *Engineering Geology, 234*(21), 97-111.

Reznichenko, N., Andrews, G., Geater, R., and Strom, A. (2017). Multiple origins of large hummock deposits in Alai Valley, Northern Pamir: implications for palaeoclimate reconstructions. *Geomorphology, 285,* 347-361.

Richefu, V., Mollon, G., Daudon, D., and Villard, P. (2012). Dissipative contacts and realistic block shapes for modeling rock avalanches. *Engineering Geology, 149*, 78-92.

Roberti, G., Friele, P., van Wyk de Vries, B., Ward, B., Clague, J., Perotti, L., and Giardino, M. (2017). Rheological evolution of the Mount Meager 2010 debris avalanche, southwestern British Columbia. *Geosphere*, *13*(2), 369-390.

Ruiz-Carulla, R., Corominas, J., and Mavrouli, O. (2017). A fractal fragmentation model for rockfalls. *Landslides*, *14*(3), 857-889.

Ryder, J. M., Bovis, M. J., and Church, M. (1990). Rock avalanches at Texas Creek, British Columbia. *Canadian Journal of Earth Sciences, 27*, 1316-1329.

Saadati, M., Forquin, P., Weddfelt, K., Larsson, P., and Hild, F. (2018). On the mechanical behaviour of granite material with particular emphasis on the influence from pre-existing cracks and defects. *Journal of Testing and Evaluation, 46*(1). doi: 1520/JTE20160072

Sakals, M. E., Geertsema, M., Schwab, J. W., and Foord, V. N. (2012). The Todagin Creek landslide of October 3, 2006 Northwest British Columbia, Canada. *Landslides, 9*, 107-115.

Salm, B. (1966). Contribution to avalanche dynamics. *International Association of Scientific Hydrology Publication 69*, 199-214.

Salm, B. (1972). Grundlagen des Lawinenverbaus. Bündner Wald 9,, 67-81.

Sandøy, G., Oppikofer, T., and Nilsen, B. (2017). Why did the 1756 Tjellefonna rockslide occur? A back-analysis of the largest historic rockslide in Norway. *Geomorphology, 289*, 78-95.

Sassa, K. (1985). The mechanism of debris flows. *Proceedings of the 11th International Conference on Soil Mechanics and Foundation Engineering.* San Francisco, California, 3, 1173-1176.

Savage, S., and Hutter, K. (1989). The motion of a finite mass of granular material down a rough incline. *Journal of Fluid Mechanics, 199*, 177-215.

Scheidegger, A. (1973). On the Prediction of the Reach and Velocity of Catastrophic Landslides. *Rock Mechanics, 5*, 231-236.

Schiliro, L., Esposito, C., De Blasio, F., and Mugnozza, G. (2019). Sediment texture in rock avalanche deposits: insights from field and experimental observations. *Landslides, 6(*9), 1629-1643.

Schleier, M., Hermanns, R., and Rohn, J. (207). Rock Avalanches in a Changing Landscape Following the Melt Down of the Scandinavian Ice Sheet, Norway. Workshop on World *Landslide Forum*.

Schneider, D., Bartelt, P., Caplan-Auerbach, J., Christen, M., Huggel, C., and McArdell, B. (2010). Insights into rock-ice avalanche dynamics by combined analysis of seismic recordings and a numerical avalanche model. *Journal of Geophysical Research: Earth Surface, 155*(F4). doi: 10.1029/2010JF001734

Shaller, P. (n.d.). Analysis and implications of large Martian and terrestrial landslides, Ph.D. Thesis. California Institute of Technology.

Shen, W., Li, T., Li, P., Berti, M., Shen, Y., and Guo, J. (2019). A two-layer numerical model for simulating the frontal plowing phenomenon of flow-like landslides. *Engineering Geology, 259.* doi: 10.1016/j.enggeo.2019.105168

Shreve, R. (1968). Leakage and Fluidization in Air-Layer Lubricated Avalanches. *Geological Society of America Bulletin, 79*, 653-658.

Siebe, C., Komorowski, J.-C., and Sheridan, M. (1992). Morphology and emplacement of an unusual avalanche deposit at Jocotitlan Volcano. *Bulletin of Volcanology, 54*(7), 573-589.

Singeisen, C., Ivy-Ochs, S., Wolter, A., Steinemann, O., Akcar, N., Yesilyurt, S., and Vockenhuber, C. (2020). The Kandersteg rock avalanche (Switzerland): integrated analysis of a late Holocene catastrophic event. *Landslides, 17,* 1297-1317.

Sosio, R., Crosta, G., Chen, J., and Hungr, O. (2012). Modelling rock avalanche propagation onto glaciers. *Quaternary Science Reviews, 47*, 23-40.

Sosio, R., Crosta, G., and Hungr, O. (2008). Complete dynamic modelling calibration for the Thurwieser rock avalanche (Italian Central Alps). *Engineering Geology, 100*(1-2), 11-26.

Straub, S. (1996). Self-organisation in the rapid flow of granular material: evidence for a major flow mechanism. *Geologische Rundschau, 86*, 415-425.

Straub, S. (1997). Predictability of long runout landslide motion: implications from granular flow mechanics. *Geologische Rundschau, 86*(2), 415-425.

Strom, A. (2006). Morphology and Internal Structure of Rockslides and Rock Avalanches: Grounds and Constraints for their Modelling. *Landslides from Massive Rock Slope Failure*, 305-326.

Strom, A. (2015). Possible Causes of Accelerating Landslide Motion in Confined Environment. In *Engineering Geology for Society and Territory* (Vol. 2, pp. 883-885). Springer International.

Strom, A., Li, L., and Lan, H. (2019). Rock avalanche mobility: optimal characterization and the effects of confinement. *Landslide, 16*(8), 1437-1452.

Su, X., Wei, W., Ye, W., Meng, X., and Wu, W. (2019). Predicting landslide sliding distance based on energy dissipation and mass point kinematics. *Natural Hazards, 96*, 1367-1385.

Taboada, A., Chang, K., Radjai, F., and Bouchette, F. (2005). Rheology, force transmission, and shear instabilities in frictional granular media from biaxial numerical tests using the contact dynamics method. *Journal of Geophysical Research, 110*(B9). doi: 10.1029/2003JB002955

Taboada, A., Estrada, N., and Radjai, F. (2006). Additive decomposition of shear strength in cohesive granular media form grain-scale interactions. *Physical review letters, 97*(9). Doi: 10.1103/PHysRevLett.97.098302

Tang, C., Hu, J., Lin, M., Angelier, J., Lu, C., Chan, Y., and Chu, H. (2009b). The Tsaoling landslide triggered by the Chi-Chi earthquake, Taiwan: insights from a discrete element simulation. *Engineering Geology, 106*(1-2), 1-19.

Tang, C., Zhu, J., Li, W. L., and Liang, J. T. (2009a). Rainfall-triggered debris flows following the Wenchuan earthquake. *Bulletin of Engineering Geology and the Environment, 68*(2), 187-194.

Terzaghi, K. (1962). Stability of steep slopes on hard unweathered rock. *Geotechnique, 12*, 251-270.

Turcotte, D. (1986). Fractals and fragmentation. *Journal of Geophysical Research: Solid Earth, 91*(B2), 1921-1926.

Van Gassen, W., and Cruden, D. (1989). Momentum transfer and friction in the debris of rock avalanches. *Canadian Geotechnical Journal, 26*(4), 623-628.

Viero, A., Furlanis, S., Squarzoni, C., Teza, G., Galgaro, A., and Piero, G. (2012). Dynamics and mass balance of the 2007 Cima Una rockfall (Eastern Alps, Italy). *Landslides, 10*(4), 393-408.

Voellmy. (1955). Uber die Zerstrungskraft von Lawinen. Schweiz. *Schweizerische Bauzeitung, 75*, 159-162.

Voight, B., Janda, R., Glicken, H., and Douglass, P. (1983). Nature and mechanics of the Mount St Helens rockslide-avalanche of 18 May 1980. *Geotechnique, 33*(3), 243-273.

Voight, B., and Sousa, J. (1994). Lessons from Ontake-san: a comparative analysis of debris avalanche dynamics. *Engineering Geology, 38*(3-4), 261-297.

Walter, F., Amann, F., Kos, A., Kenner, R., Phillips, M., de Preux, A., Huss, M., Tagnacca, C., Clinton, J., Diehl, T., and Bonanomi, Y. (2020). Direct observations of a three million cubic meter rock-slope collapse with almost immediate initiation of ensuing debris flows. *Geomorphology, 351*(1). doi: 10.1016/j.geomorph.2019.106933

Wang, Y., Cheng, Q., Lin, Q., Li, K., and Yang, H. (2018a). Insights into the kinematics and dynamics of the Luanshibao rock avalanche (Tibetan Plateau, China) based on its complex surface landforms. *Geomorphology, 317*, 170-183.

Wang, Y.-F., Cheng, Q.-G., Shi, A.-W., Yuan, Y.-Q., Yin, B.-M., and Qui, Y.-H. (2019). Sedimentary deformation structures in the Nyixoi Chongco rock avalanche: implications on rock avalanche transport mechanisms. *Landslides, 16*(3), 523-532.

Wang, Y., Cheng, Q., Yuan, Y., Wang, J., Qui, Y., Yin, B., Shi, A., and Guo, Z. (2020). Emplacement mechanisms of the Tagarma rock avalanche on the Pamir-western Himalayan syntaxis of the Tibetan Plateau, China. *Landslides, 17*, 527-542.

Wang, Y., Cheng, Q., and Zhu, A. (2015). Surface microscopic examination of quartz grains from rock avalanche basal facies. *Canadian Geotechnical Journal, 52*(2), 167-181.

Wang, Y., Dong, J., and Cheng, Q. (2017). Velocity-dependent frictional weakening of large rock avalanche basal facies: Implications for rock avalanche hypermobility? *Journal of Geophysical Research: Solid Earth, 122*(3), 1648-1676.

Wang, Y., Dong, J., and Cheng, Q. (2018b). Normal Stress-Dependent Frictional Weakening of Large Rock Avalanche Basal Facies: Implications for the Rock Avalanche Volume Effect. *Journal of Geophysical Research: Solid Earth, 123*, 3270-3282.

Whitehouse, I. E., and Griffiths, G. A. (1983). Frequency and hazard of large rock avalanches in the central Southern Alps, New Zealand. *Geology, 11*(6)*,* 331-334.

Whittall, J. (2019). Runout estimates and risk-informed decision making for bench scale open pit slope failure. *Canadian Geotechnical Journal, 57*(7), 1044-1057.

Wilson, C. (1984). The role of fluidisation in the emplacement of pyroclastic flows: 2. Experimental results and their interpretations. *Journal of Volcanology and Geothermal Research, 20*, 55-84.

Wyllie, D., and Mah, C. (2004). *Rock Slope Engineering* (Vol. 4). London, New York: Spon Press.

Wyllie, D. C., and Norrish, N. I. (1996). Rock Strength Properties and Their Measurement. *Investigation and Mitigation,* 372-390.

Xu, Q., Shang, Y., van Asch, T., Wang, S., Zhang, Z., and Dong, X. (2012). Observations from the large, rapid Yigong rockslide-debris avalanche, southeast Tibet. *Canadian Geotechnical Journal, 49*, 589-606.

Yamada, M., Mageney, A., Matsushi, Y., and Matsuzawa, T. (2018). Estimation of dynamic friction and movement history of large landslides. *Landslides, 15*, 1963-1974.

Yang, Q., Cai, F., Su, Z., Ugai, K., Xu, L., Huang, R., and Xu, Q. (2014). Numerical Simulation of Granular Flows in a Large Flume Using Discontinuous Deformation Analysis. *Rock Mechanics and Rock Engineering, 47*, 2299-2306.

Yang, Q., Cai, F., Ugai, K., Yamada, M., Su, Z., Ahmed, A., Huang, R., and Xu, Q. (2011). Some factors affecting mass-front velocity of rapid dry granular flows in a large flume. *Engineering Geology, 122*(3-4), 249-260.

Yang, Q., Su, Z., Cheng, Q., Ren, Y., and Cai, F. (2019). High mobility of rock-ice avalanches: Insights from small flume tests of gravel-ice mixtures. *Engineering Geology, 260*. doi: 10.1016/j.enggeo.2019.105260

Zhan, W., Fan, X., Huang, R., Pei, X., and Li, W. (2017). Empirical prediction for travel distance of channelized rock avalanches in the Wenchuan earthquake area. *Natural Hazards Earth System Sciences, 17*, 833-844.

Zhang, M., and McSaveney, M. (2017). Rock avalanche deposits store quantitative evidence on internal shear during runout. *Geophysical Research Letters, 44*(17), 8814-8821.

Zhang, M., Wu, L., Zhang, J., and Li, L. (2019). The 2009 Jiweishan rock avalanche, Wulong, China: Deposit characteristics and implications for its fragmentation. *Landslides, 16,* 893-906.

Zhang, M., Yin, Y., and McSaveney, M. (2016). Dynamics of the 2008 earthquake-triggered Wenjiagou Creek rock avalanche, Quinping, Sichuan, China. *Engineering Geology, 200*, 75-87.

Zhao, T., Crosta, G., Dattola, G., and Utili, S. (2018). Dynamic Fragmentation of Jointed Rock Blocks During Rockslide-Avalanches: Insights From Discrete Element Analyses. *Journal of Geophysical Research: Solid Earth, 123*(4), 3250-3269

Zhao, T., Crosta, G., Utili, S., and De Blasio, F. (2017). Investigation of rock fragmentation during rockfalls and rock avalanches via 3-D discrete element analyses. *Journal of Geophysical Research: Earth Surface, 122*, 1-18.

Zhao, T., and Liu, Y. (2020). A novel random discrete element analysis of rock fragmentation. *International Journal for Numerical and Analytical Methods in Geomechanics, 44*(10), 1386-1395.

Zhou, J., Su, Z., and Yang, X. (2013). Kinetic Friction Coefficient and Mass Movement Process of Large Rock Avalanches Triggered by the Wenchuan Earthquakes. In K. Ugai, H. Yagi, and A. Wakai (Eds.), *Earthquake Induced Landslides: Proceedings of the International Symposium on Earthquake-Induced Landslides, Kiryu, Japan, 2012* (pp. 521-528). Springer.

Zhu, Y., Dai, F., and Yao, X. (2020). Preliminary understanding of the emplacement mechanism for the Tahman rock avalanche based on deposit landforms. *Quarterly Journal of Engineering Geology and Hydrogeology 5*(3), 460-465.

Zygouri, V., and Koukouvelas, I. (2017). Techniques of Rockfall Inventory in Earthquake Prone Rock Slopes. *Bulletin of the Geological Society of Greece, 50*, 1756-1765.

Appendix A: Rock Avalanche Database

Name	Location	Height (km)	Length (km)	H/L	Volume (km^3)	Area (km^2)	Thickness (m)	Deposition Length	Rock Type	Reference
Blackhawk		1.2	9.6	0.13	0.28					Legros, 2002
Corno di desde		1.2	3.7	0.32	0.02					Legros, 2002
Deyen, Glarus		0.74	6.6	0.11	0.6					Legros, 2002
Diablerets		1.9	5.5	0.35	0.05					Legros, 2002
Disentis		0.74	2.1	0.35	0.015					Legros, 2002
Elm		0.71	2.3	0.31	0.01					Legros, 2002
Engelberg		1.6	7.4	0.22	2.75					Legros, 2002
Fernpass		1.4	15.6	0.09	1					Legros, 2002
Flims		2	15.6	0.13	12					Legros, 2002
Frank		0.87	3.5	0.25	0.03					Legros, 2002
Garnish		1.9	7.5	0.25	0.8					Legros, 2002
Goldau		1.2	6	0.20	0.035					Legros, 2002
Gros Ventre		0.56	3.4	0.16	0.038					Legros, 2002
Kandertal		1.9	9.9	0.19	0.14					Legros, 2002
Maligne Lake		0.92	5.47	0.17	0.5					Legros, 2002
Medicine Lake		0.32	1.22	0.26	0.086					Legros, 2002
Madison		0.43	1.6	0.27	0.029					Legros, 2002
Mombiel		0.37	0.8	0.46	0.0008					Legros, 2002
Obersee GL		1.8	5	0.36	0.12					Legros, 2002
Pamir		1.5	6.2	0.24	2					Legros, 2002
Poshivo		1.5	4.1	0.37	0.15					Legros, 2002
Saidmarreh		1.5	18.9	0.08	20					Legros, 2002
Schachental		1.8	3.1	0.58	0.0005					Legros, 2002
Scimada Saoseo		1.5	5.5	0.27	0.08					Legros, 2002
Sherman		1.3	6.2	0.21	0.03					Legros, 2002
Siders		2.4	17.4	0.14	1.5					Legros, 2002
Tamins		1.3	13.5	0.10	1.3					Legros, 2002

Vaiont		0.5	1.5	0.33	0.25					Legros, 2002
Val Lagone		1.05	2.4	0.44	0.0007					Legros, 2002
Voralpsee		1.1	3.4	0.32	0.03					Legros, 2002
Wengen 1		0.5	1.1	0.45	0.0025					Legros, 2002
Wengen 2		0.59	1.4	0.42	0.0055					Legros, 2002
Akagi		2.4	19	0.13	4					Legros, 2002
Asakusa		1	6.5	0.15	0.04					Legros, 2002
Asama		1.8	20	0.09	2	90				Legros, 2002
Bandai-san 1888		1.2	11	0.11	1.5	34				Legros, 2002
Bezymianni 1956		2.4	18	0.13	0.8	30				Legros, 2002
Callaqui		3.1	15	0.21	0.15					Legros, 2002
Chaos Crags		0.65	5	0.13	0.15	8				Legros, 2002
Chimborazo		3.6	35	0.10	8.1					Legros, 2002
Chokai		2.2	25	0.09	3.5					Legros, 2002
Colima		4	40	0.10	12.5	900				Legros, 2002
Egmont (Pungarehu)		2.6	31	0.08	7.5	250				Legros, 2002
Egmont (Opua)		2.5	27	0.09	0.35	120				Legros, 2002
Fuji		2.5	24	0.10	1.8					Legros, 2002
Galunggung		1.9	25	0.08	2.9	175				Legros, 2002
Iriga		1.05	11	0.10	1.5	65				Legros, 2002
Iwaki		1.6	14	0.11	1.5					Legros, 2002
Komagatake		1	11.5	0.09	0.25					Legros, 2002
Kurohime		0.8	6	0.13	0.12					Legros, 2002
Mageik	0.8	0.8	9	0.09	0.09					Legros, 2002
Mawenzi		4.5	60	0.08	7.1	1150				Legros, 2002
Meru		3.9	50	0.08	15	1400				Legros, 2002
Monbacho		1.3	12	0.11	1	45				Legros, 2002
Mt. St. Helns 1980		2.55	24	0.11	2.5	60				Legros, 2002
Myoko (Sekikawa		2	19	0.11	0.8					Legros, 2002
Myoko (Taguchi)		1.4	8	0.18	0.23	10				Legros, 2002
Ovalnaya Zimina		2.4	17	0.14	0.4					Legros, 2002

Papandayan		1.5	11	0.14	0.14					Legros, 2002
Peteroa	3.9	3.9	85	0.05	16					Legros, 2002
Popa		1.2	11	0.11	0.8					Legros, 2002
Popocatepetl		4	33	0.12	28					Legros, 2002
Shasta		3.55	50	0.07	26	450				Legros, 2002
Shiveluch	2	2	12	0.17	1.5	98				Legros, 2002
Sierra Velluda		3.4	25	0.14	0.5					Legros, 2002
Socompa		3.25	35	0.09	17	480				Legros, 2002
Tashiro		0.7	8.8	0.08	0.55					Legros, 2002
Tateshina		1.4	12.5	0.11	0.35					Legros, 2002
Unzen		0.85	6.5	0.13	0.34	12				Legros, 2002
Usu		0.5	6.5	0.08	0.3					Legros, 2002
Yatsugatake (Nirasaki)		2.4	32	0.08	9					Legros, 2002
Yatsugatake (Otsukigawa)		1.4	12.5	0.11	0.27					Legros, 2002
Soufriere Guadeloupe		1.35	9.5	0.14	0.5	25				Legros, 2002
St Helens 20000 BP		1.75	16	0.11	1					Legros, 2002
Vesuvius 1944		0.575	0.64	0.90	0.0002	0.898				Legros, 2002
Vesuvius 1944		0.505	0.94	0.54	0.0009	0.537				Legros, 2002
Vesuvius 1944		0.285	0.5	0.57	0.0006	0.099				Legros, 2002
Vesuvius 1944		0.47	0.96	0.49	0.0008	0.126				Legros, 2002
Vesuvius 1944		0.636	1.24	0.51	0.001	0.136				Legros, 2002
Vesuvius 1944		0.36	0.68	0.53	0.0011	0.145				Legros, 2002
Vesuvius 1944		0.41	0.82	0.50	0.0012	0.161				Legros, 2002
Jocotitlan		1.15	12	0.10	2.8	80				Legros, 2002, Siebe et al. 1992
Frank Slide		0.76	3.5	0.22		2.44	15	2300		Locat et al. 2006
Slide Mountain		0.42	1.65	0.25		1.28	25	1130		Locat et al. 2006
Queen Elizabeth		0.95	2.65	0.36		0.93	60	1800		Locat et al. 2006
Jonas Creek north		0.86	2.8	0.31		1.08	3	1880		Locat et al. 2006
Jonas Creek south		0.9	1.83	0.49		0.5	12	700		Locat et al. 2006
Claps de Luc		0.37	0.8	0.46		0.4	15	425		Locat et al. 2006

La Madeleine		1.25	4.5	0.28		2.06	60	500		Locat et al. 2006
Charmonetier		0.52	0.6	0.87		0.04	15	400		Locat et al. 2006
Arvel		0.25	0.35	0.71		0.03	10	310		Locat et al. 2006
Sao Nicolau N		2.869		0.11						Masson et al. 2008
Sao Nicolau NE		3.127		0.12						Masson et al. 2008
Sao Nicolau NW		2.682		0.10						Masson et al. 2008
Sao Nicolau S		4.306		0.07						Masson et al. 2008
Sao Vicente		2.703		0.06						Masson et al. 2008
Thurwieser		0.583	2.9	0.20						Sosio et al. 2008
Lorna d Aspereza		1	7	0.14					Granite/schist	Hermanns and Strecker, 1999
Aval d Zarzo I		0.9	6.5	0.14					Granite	Hermanns and Strecker, 1999
Aval d Zarzo II		0.65	4	0.16					Granite	Hermanns and Strecker, 1999
Lorna d Redonda		1	7	0.14					Granite/Schist	Hermanns and Strecker, 1999
Villa Vil I		0.3	2.5	0.12					Volcanic breccia	Hermanns and Strecker, 1999
Villa Vil II		0.35	2.25	0.16					Volcanic breccia	Hermanns and Strecker, 1999
Villa Vil III		0.4	2.5	0.16					Volcanic breccia	Hermanns and Strecker, 1999
Villa Vil IV		0.4	2.75	0.15					Volcanic breccia	Hermanns and Strecker, 1999
Villa Vil V		0.4	1.5	0.27					Volcanic breccia	Hermanns and Strecker, 1999
Villa Vil VI		0.25	1	0.25					Volcanic breccia	Hermanns and Strecker, 1999
Rincon Ruins I		0.8	5.5	0.15					Granite	Hermanns and Strecker, 1999
NN		0.5	2.2	0.23					Granite	Hermanns and Strecker, 1999

nn		0.7	3.5	0.20					Phyllite	Hermanns and Strecker, 1999
NN		0.7	3.75	0.19					Conglomerate	Hermanns and Strecker, 1999
NN		0.7	3.1	0.23					Conglomerate	Hermanns and Strecker, 1999
El Paso I		1.1	4.75	0.23					Conglomerate	Hermanns and Strecker, 1999
El Paso II		0.7	2.85	0.25					Conglomerate	Hermanns and Strecker, 1999
Casa de los Loros II		1.1	3.5	0.31					Conglomerate	Hermanns and Strecker, 1999
I		0.65	2.3	0.28					Conglomerate	Hermanns and Strecker, 1999
Brealito		0.7	2.25	0.31					Conglomerate	Hermanns and Strecker, 1999
Pandemonium Cr. 1959		2	8.6	0.23					Gneiss	Nicoletti and Sorriso-Valvo, 1991
Twin Slides		0.9	4.67	0.19					Caron r.	Nicoletti and Sorriso-Valvo, 1991
Twin Slides €		0.82	4.4	0.19					Carbon r.	Nicoletti and Sorriso-Valvo, 1991
Antronapiana, 1642		1.65	4.19	0.39					Gneiss	Nicoletti and Sorriso-Valvo, 1991
Huascaran, 1962		3.6	15.5	0.23					Granodiorite	Nicoletti and Sorriso-Valvo, 1991
Triolet Glac, 1717		1.86	6.9	0.27					Granite	Nicoletti and Sorriso-Valvo, 1991
Steller 1, 1964		1.2	6.7	0.18					Granite	Nicoletti and Sorriso-Valvo, 1991
Allen 4, 1964 or 1965		1.3	7.7	0.17					Granite	Nicoletti and Sorriso-Valvo, 1991
Fairweather 1964 or 1965		3.3	10	0.33					Granite	Nicoletti and Sorriso-Valvo, 1991
Schwan, 1964		1.55	6.1	0.25					Granite	Nicoletti and Sorriso-Valvo, 1991

Devastation GL. 1975	1.19	6.1	0.20					Soft volc r.	Nicoletti and Sorriso-Valvo, 1991
Diablerets, 1749	1.2	5.5	0.22					Limestone	Nicoletti and Sorriso-Valvo, 1991
Rubble Cr. 1855 or 1856	1.04	6.9	0.15					Dacite	Nicoletti and Sorriso-Valvo, 1991
Nozzle, unk	1.05	6.42	0.16					Carbon r.	Nicoletti and Sorriso-Valvo, 1991
Huscaran, 1970	3.85	15.6	0.25					Granodiorite	Nicoletti and Sorriso-Valvo, 1991
Dust Cr. 1963	0.97	2.49	0.39					Dacite	Nicoletti and Sorriso-Valvo, 1991
Sasso Englar	0.6	2.3	0.26					Resissant volc. R	Nicoletti and Sorriso-Valvo, 1991
Dfinov	0.37	1.68	0.22					Gneiss	Nicoletti and Sorriso-Valvo, 1991
Damocles	0.55	3.4	0.16					Carbon r,	Nicoletti and Sorriso-Valvo, 1991
Mystery Cr.	1.25	4	0.31					Diorite	Nicoletti and Sorriso-Valvo, 1991
Goldau 1806	1.12	6.1	0.18					Conglomerate	Nicoletti and Sorriso-Valvo, 1991
Low Gros Venture, 1925	0.66	4.35	0.15					Sandstone, limestone soft red r.	Nicoletti and Sorriso-Valvo, 1991
Stalk Lakes	0.7	3	0.23					Clastic r.	Nicoletti and Sorriso-Valvo, 1991
Lavini di Marco 1883	1.17	5.65	0.21					Carbon r.	Nicoletti and Sorriso-Valvo, 1991
Mont Granier, 1248	1.52	7.69	0.20					Limestone marl	Nicoletti and Sorriso-Valvo, 1991
Silver Reef	0.76	6.67	0.11					Marble	Nicoletti and Sorriso-Valvo, 1991
Martinez Mt	1.85	8.56	0.22					Gneiss	Nicoletti and Sorriso-Valvo, 1991

Rockslide Pass		1	6.33	0.16					Dolostone, Limestone	Nicoletti and Sorriso-Valvo, 1991
Maligne Lake		0.98	5.47	0.18					Carbon r. Chert, Shale	Nicoletti and Sorriso-Valvo, 1991
Mayunmarca, 1974		1.8	8	0.23					Sandstone, Siltstone	Nicoletti and Sorriso-Valvo, 1991
Costantino, 1973		0.94	2.24	0.42					Gneiss	Nicoletti and Sorriso-Valvo, 1991
Madison Canyon, 1959		0.43	1.68	0.26					Gneiss, Schist, Dolostone	Nicoletti and Sorriso-Valvo, 1991
Monte Zandilla, 1987		1.39	3.95	0.35					Diorite gabbro, orthoquartz	Nicoletti and Sorriso-Valvo, 1991
Hope, 1965		1.22	4.24	0.29					Basic metavolc r.	Nicoletti and Sorriso-Valvo, 1991
Triple Slide		0.55	3.97	0.14					Carbon r.	Nicoletti and Sorriso-Valvo, 1991
Parpan		1.34	6.55	0.20					Dolostone, crystal r.	Nicoletti and Sorriso-Valvo, 1991
LC1n				0.18						Crosta et al. 2017b
LC1s				0.18						Crosta et al. 2017b
LC2				0.21						Crosta et al. 2017b
LC3s				0.24						Crosta et al. 2017b
LC3s				0.30						Crosta et al. 2017b
LC3n				0.26						Crosta et al. 2017b
LC3n				0.33						Crosta et al. 2017b
LC4				0.34						Crosta et al. 2017b
LC3n				0.36						Crosta et al. 2017b
LN1				0.18						Crosta et al. 2017b
LN1				0.27						Crosta et al. 2017b
LN2				0.26						Crosta et al. 2017b
LN3s				0.25						Crosta et al. 2017b
LN3n				0.26						Crosta et al. 2017b
LN3c				0.25						Crosta et al. 2017b

LS1				0.38						Crosta et al. 2017b
Poulter River							10			Whitehouse and Griffiths, 1983
Poutler River							35			Whitehouse and Griffiths, 1983
Poulter River							10			Whitehouse and Griffiths, 1983
Poulter River							10			Whitehouse and Griffiths, 1983
Taramakau River							30			Whitehouse and Griffiths, 1983
Waimakariri River							40			Whitehouse and Griffiths, 1983
Waimakariri River							50			Whitehouse and Griffiths, 1983
Otira River							100			Whitehouse and Griffiths, 1983
Taipo River							50			Whitehouse and Griffiths, 1983
Taipo River							20			Whitehouse and Griffiths, 1983
Wainamkariri River							100			Whitehouse and Griffiths, 1983
Craigieburn Range							10			Whitehouse and Griffiths, 1983
Taipo River							15			Whitehouse and Griffiths, 1983
Cragieburn Range							5			Whitehouse and Griffiths, 1983
Wilberforce River							50			Whitehouse and Griffiths, 1983
Wilberforce River							20			Whitehouse and Griffiths, 1983
Avoca River							50			Whitehouse and Griffiths, 1983

Craigieburn Range							130			Whitehouse and Griffiths, 1983
Acheron River							10			Whitehouse and Griffiths, 1983
Wilberforce River							10			Whitehouse and Griffiths, 1983
Wilberforce River							25			Whitehouse and Griffiths, 1983
Lake Coleridge							20			Whitehouse and Griffiths, 1983
Mathias River							100			Whitehouse and Griffiths, 1983
Mathias River							20			Whitehouse and Griffiths, 1983
Mathias River							20			Whitehouse and Griffiths, 1983
Mathias River							10			Whitehouse and Griffiths, 1983
North Ashburton River							15			Whitehouse and Griffiths, 1983
South Ashburton River							10			Whitehouse and Griffiths, 1983
Lawrence River							10			Whitehouse and Griffiths, 1983
Lawrence River							15			Whitehouse and Griffiths, 1983
Clyde River							50			Whitehouse and Griffiths, 1983
Clyde River							20			Whitehouse and Griffiths, 1983
Martin River 2		1.12	4	0.28		5	2			Sosio et al. 2012
Martin River 3		1.4	5	0.28		3.9	2			Sosio et al. 2012
Martin River 4		2.36	5.9	0.40		5.2	1			Sosio et al. 2012
Martin River 5		1.184	3.7	0.32		1.5	2			Sosio et al. 2012
Martin River		1.72	4.3	0.40		2.1	1			Sosio et al. 2012

Martin River unnamed 2		1.116	3.6	0.31		1.8	1			Sosio et al. 2012
Illiamna-Red Glacier		1.978	8.6	0.23		4	2			Sosio et al. 2012
Mt Munday		1.035	4.5	0.23		2.5	1.5			Sosio et al. 2012
Punta Thurwieser		1.392	2.9	0.48		0.8	5			Sosio et al. 2012
Eperon de la Brenva		2.145	5.5	0.39		0.35	6			Sosio et al. 2012
Mt. Cook		0.759	6.9	0.11		7.5	1.5			Sosio et al. 2012
Jiweishan		0.7	2.15	0.33						
Tsaoling, Taiwan		1.208	3.8	0.32						Tang et al. 2009a
Glarnisch				0.25						Scheidegger, 1973
Vajont				0.34						Scheidegger, 1973
Diablerets				0.34						Scheidegger, 1973
Little Tahoma Pk.				0.29						Scheidegger, 1973
Wengen				0.42						Scheidegger, 1973
Wengen S				0.45						Scheidegger, 1973
Airolo				0.64						Scheidegger, 1973
Lecco				0.88						Scheidegger, 1973
Berrfottene		1	4	0.25						Hermanns et al. 2012
Bjorkum		0.4	0.55	0.73						Hermanns et al. 2012
Erdalen		0.46	1.01	0.46						Hermanns et al. 2012
Frykkjelen		0.95	2.2	0.43						Hermanns et al. 2012
Furuneset		0.9	1.5	0.60						Hermanns et al. 2012
Grande		1.35	1.45	0.93						Hermanns et al. 2012
Gravem		0.9	1.5	0.60						Hermanns et al. 2012
Grotlandsura		0.5	1.2	0.42						Hermanns et al. 2012
Gumpedalen		0.72	2.2	0.33						Hermanns et al. 2012
Hellaren		0.9	4	0.23						Hermanns et al. 2012
Hysket		0.55	1.13	0.49						Hermanns et al. 2012
Kubergan 1		0.375	0.7	0.54						Hermanns et al. 2012
Kubergan 2		0.35	0.64	0.55						Hermanns et al. 2012
Langhammaren		0.85	1.5	0.57						Hermanns et al. 2012
Melkevoll		0.48	0.75	0.64						Hermanns et al. 2012

Nakkevatnet		0.9	2.35	0.38						Hermanns et al. 2012
Rorsetura		0.65	1.1	0.59						Hermanns et al. 2012
Skjaersura		1	1.75	0.57						Hermanns et al. 2012
Store Urdi		0.4	1.4	0.29						Hermanns et al. 2012
Stolaholmen		0.42	0.96	0.44						Hermanns et al. 2012
Sordalen		0.675	1.5	0.45						Hermanns et al. 2012
Tjellefonna		0.75	2	0.38						Hermanns et al. 2012
Urbadouri		0.47	1.35	0.35						Hermanns et al. 2012
Venge		0.76	1.7	0.45						Hermanns et al. 2012
Verkildsdalen		0.675	1.6	0.42						Hermanns et al. 2012
LCRA1		0.495	1.78	0.28			23			Lee et al. 2009
Cascadw		0.62	4.8	0.13		9.1				Barth, 2014
Round Top		0.57	4.8	0.12		5.6				Barth, 2014
Wenjia Gully		0.44	4	0.11		3				Zhan et al. 2017
Shuimo Gully		0.49	2	0.25		0.915				Zhan et al. 2017
Dawuji		0.54	1.9	0.28		0.792				Zhan et al. 2017
Donghekou		0.24	2.4	0.10		1.283				Zhan et al. 2017
Hongshi Gully		0.29	2.7	0.11		0.687				Zhan et al. 2017
Woqian		0.33	1.6	0.21		0.695				Zhan et al. 2017
Xiaojiashan		0.48	1.35	0.36		0.465				Zhan et al. 2017
Niumian Gully		0.32	2.64	0.12		0.527				Zhan et al. 2017
Liqi Gully		0.36	1.5	0.24		0.355				Zhan et al. 2017
Caocaoping		0.345	1.34	0.26		0.354				Zhan et al. 2017
Huoshi Gully		0.27	1.32	0.20		0.322				Zhan et al. 2017
Shibangou		0.45	1.8	0.25		0.496				Zhan et al. 2017
Xiejiadianzi		0.4	1.6	0.25		0.294				Zhan et al. 2017
Dashui Gully		0.32	1.4	0.23		0.241				Zhan et al. 2017
Changping		0.29	1.2	0.24		0.224				Zhan et al. 2017
Xiaomuling		0.175	1.03	0.17		0.218				Zhan et al. 2017
Baishuling		0.335	1.2	0.28		0.208				Zhan et al. 2017

Dawan		0.22	1	0.22		0.203				Zhan et al. 2017
Xiajiashan		0.34	1.14	0.30		0.198				Zhan et al. 2017
Shicouzi		0.26	1.2	0.22		0.169				Zhan et al. 2017
Changtan		0.4	1.65	0.24		0.151				Zhan et al. 2017
Hongmagong		0.195	0.8	0.24		0.144				Zhan et al. 2017
Baiguocun		0.165	0.8	0.21		0.139				Zhan et al. 2017
Qinglongcun		0.09	0.6	0.15		0.134				Zhan et al. 2017
Pengjiashan		0.2	1	0.20		0.127				Zhan et al. 2017
Longwancun		0.205	0.86	0.24		0.099				Zhan et al. 2017
Zhangzhengbo		0.125	0.8	0.16		0.099				Zhan et al. 2017
Dujiayan		0.1	0.88	0.11		0.094				Zhan et al. 2017
Madiping		0.14	0.74	0.19		0.094				Zhan et al. 2017
Yandiaowo		0.145	0.8	0.18		0.092				Zhan et al. 2017
Chuangzi Gully		0.185	0.67	0.28		0.091				Zhan et al. 2017
Zhaojiashan		0.115	0.7	0.16		0.082				Zhan et al. 2017
Weiziping		0.135	0.6	0.23		0.074				Zhan et al. 2017
Maochongshan 2		0.16	0.74	0.22		0.07				Zhan et al. 2017
Waqianshan		0.135	0.62	0.22		0.07				Zhan et al. 2017
Muhongping		0.175	0.97	0.18		0.068				Zhan et al. 2017
Dapingshang		0.16	0.64	0.25		0.065				Zhan et al. 2017
Liushuping 2		0.15	0.58	0.26		0.054				Zhan et al. 2017
North Creek		0.728	2.8	0.26						Geertsema et al. 2006
Kshwan Glacier		0.713	2.3	0.31						Geertsema et al. 2006
Kendall Glacier		0.204	1.2	0.17						Geertsema et al. 2006
Howson II		1.296	2.7	0.48						Geertsema et al. 2006
Chisca		0.36	1.5	0.24						Geertsema et al. 2006
Turnoff Creek		0.56	2	0.28						Geertsema et al. 2006
Mosque Mountain		0.504	1.2	0.42						Geertsema et al. 2006
Zymoetz		1.247	4.3	0.29						Geertsema et al. 2006

Harold Price		0.72	4	0.18						Geertsema et al. 2006
Pink Mountain		0.42	2	0.21						Geertsema et al. 2006
Wenjiagou		0.535	2.28	0.23						Zhou et al. 2012
Niumiangou		0.658	2.61	0.25						Zhou et al. 2012
Tschirgant		1.48	6.3	0.23		9.8				Dufresne et al. 2015
Innerdalen		1.24	5.28	0.23						~~Schleier et al. 2017~~
Innfjorddalen		1.34	4.19	0.32						~~Schleier et al. 2017~~
Aishihik River		0.56	2.16	0.26						Huscroft et al. 2004
Avalanche Lake North		1.09	4	0.27						Eisbacher 1977, 1979
Avalanche Lake South		1.12	6.25	0.18						Eisbacher 1977, 1979
Beaver Flats North		0.32	1.07	0.30						Cruden 1976
Beaver Flats South		0.22	1.2	0.18						Cruden 1976
Brazeau Lake Slide		0.62	2.4	0.26						Cruden 1982
Cheam		1.05	6.42	0.16						Orwin et al. 2004
CHisca		0.33	1.39	0.24						Geertsema et al. 2006
Eagle Pass (Clanwilliam)		0.57	0.95	0.60						Hungr and Evans 2004
Jonas Creek North		0.88	3.25	0.27						Cruden 1976
Jonas Creek South		0.92	2.49	0.37						Cruden 1976
Little Salmon Lake		0.49	1.62	0.30						Brideau et al. 2010
McAuley Creek		0.5	1.6	0.31						Brideau et al. 2012
Mount Kitchener		0.95	2.42	0.39						Cruden 1976
Mount Meager		1.72	8.95	0.19						Guthrie et al. 2012
Mount Sparrowhawk		0.56	1.59	0.35						Cruden and Eaton 1988
Mt Cayley 1963		1	2.46	0.41						Clague and Souther 1982
Mt Cayley 1984		1.18	3.46	0.34						Evans et al. 2001
Nahanni But		0.4	1.55	0.26						Evans et al. 1987
Nomash River		0.46	1.93	0.24						Hungr and Evans 2004
Pelly Mountains 1		0.74	3.7	0.20						Jackson and Isobe 1990
Pelly Mountains 2		0.61	2.18	0.28						Jackson and Isobe 1990
Pelly Mountains 3		0.35	1.8	0.19						Jackson and Isobe 1990
Pelly Mountains 4		0.78	2.92	0.27						Jackson and Isobe 1990

Pelly Mountains 5		0.471	1.61	0.29						Jackson and Isobe 1990
Ruby Volcano		0.69	3.34	0.21						Levson et al. 2003
Sutherland		0.27	1.45	0.19						Blais-Stevens et al. 2015
Texas Creek		0.71	2.3	0.31						Ryder et al. 1990
Todagin Creek		0.84	2.19	0.38						Sakals et al. 2012
Vulcan Creek		0.355	1.2	0.30						Brideau et al. 2016
Tim Williams Glacier		0.935	3.7	0.25						Evans and Clague, 1991
Mount Meager		1.34	3.68	0.36						Evans and Clague, 1991
Kshwan Glacier		0.675	2.21	0.31						Evans and Clague, 1991
Yigong		3	10	0.30		6.2	80	4600		Wang et al. 2017